UNIVERSITY OF OKLAHOMA

GRADUATE COLLEGE

INTEGRATED GEOMECHANICS AND GEOLOGICAL CHARACTERIZATION OF THE DEVONIAN-MISSISSIPPIAN WOODFORD SHALE

A THESIS

SUBMITTED TO THE GRADUATE FACULTY

In partial fulfillment of the requirements for the

Degree of

MASTER OF SCIENECE

By

RAFAEL SIERRA PEREZ

Norman, Oklahoma

2011

[redacted]

INTEGRATED GEOMECHANICS AND GEOLOGICAL CHARACTERIZATION OF THE DEVONIAN-MISSISSIPPIAN WOODFORD SHALE

A THESIS APPROVED FOR THE
CONOCOPHILLIPS SCHOOL OF GEOLOGY AND GEOPHYSICS

BY

[redacted]

Dr. Younane N. Abousleiman, Chair

[redacted]

Dr. Roger M. Slatt, Co-Chair

[redacted]

Dr. Katie Keranen

[redacted]

Dr. Yucel Akkutlu

ACKNOWLEDGEMENTS

I would like to express my deepest gratitude to Dr. Younane N. Abousleiman and Dr. Roger M. Slatt who very generously accepted to be my advisors, for their guidance and support throughout my Masters, and for providing funding for my assistantship.

I also want to thank Dr. Katie Keranen and Dr. Yucel Akkutlu for serving on my committee, for their kindness, great interest, and taking the time and dedication in reviewing this manuscript.

I wish to extend my gratitude to The PoroMechanics Institute and The Institute for Reservoir Characterization for providing the funding to carry out this research. Thanks to all the member of such institutes for valuable discussions for the completion and improvement of this work.

I want to acknowledge all the member of the geomechanics impact group of ICP-Ecopetrol for the drive into geomechanics and for highlighting the importance and the future of this science in the industry.

My deepest appreciation to the staff from the PoroMechanics Institute and The School of Geology and Geophysics, in particular to Mr. John Brumley for his helpful technical support; to Ms. Carla Cates and Ms. Donna Mullins for their kindness and valuable administrative assistance. I also would like to show my appreciation to Mrs. Jody Foote, for her significant help in the Youngblood Energy Library.

I want to express my gratitude to my beloved family, for all their unconditional support throughout this experience; for giving me the strength to face all the new experiences I lived in these years. To my father, friend and mentor, whose words always find the right answer to my concerns. To my mother, who always finds the way

to put a smile on my face. To Lalu, my partner, whose presence encourages me to be a better man.

TABLE OF CONTENTS

LIST OF TABLES

LIST OF FIGURES

ABSTRACT

In this thesis, preserved Woodford Shale samples of different mineralogy compositions were obtained from a shallow research well in Oklahoma and prepared for various laboratory mechanical characterizations including the Ultrasonic Pulse Velocity (UPV) measurements, the unconfined compressive test, and the Inclined Direct Shear Testing Device (IDSTD^{TM}). In addition, the Woodford Shale fracture properties, including anisotropic tensile strength and fracture toughness, were investigated through a suite of Brazilian Tensile and Chevron Notched Semicircular Bend (CNSCB) tests with acoustic emission (AE) recorded during testing. The geomechanics characteristics of the Woodford Shale were modeled with correlation to mineralogy and micro-fabric on its effects on the mechanical properties were also studied with results from thin sections and XRD analysis performed on tested samples. The UPV and Brazilian test results show a clear anisotropic nature of Woodford Shale poroelastic properties and tensile strength. Investigations on the effects of shale mineralogy and morphology on its anisotropic mechanical properties show correlation between the degrees of anisotropy with clay packing density variation. Despite the limited number of tests reported, an increasing trend of Woodford Shale tensile strength with carbonate content could be observed. This proportional increase of tensile strength with carbonate content may suggest the strength-increasing nature of carbonate minerals in the Woodford Shale. CNSCB test results showed that the fracture toughness of the quartz-rich Upper Woodford samples is significantly higher (up to 57%) than the fracture toughness of samples from the more clay-rich Middle and Lower Woodford. This will lead to a lot of variability in hydraulic fracture

planning and design. Also, the acoustic emissions prior to the fracture propagation in CNSCB tests could only be observed for the lower clay samples belonging to the Upper Woodford. Furthermore, the integration of these results with the previously defined sequence stratigraphic framework resulted in the definitions of brittle and ductile couplets at the parasequence scale, which might be valuable for well placement and completion designs.

1. INTRODUCTION

In recent years, the oil industry has been demonstrating more interest in non-conventional hydrocarbon sources given the increase in energy prices and potential technology available. In the U.S midcontinent (e.g. Oklahoma and Texas) several companies are now giving special attention to formations previously interpreted as source rocks that are now being recognized as hydrocarbon potential pays, such as the Barnett Shale and the Woodford Shale (Comer, 2005). The Woodford Shale is one of many Devonian black shales that are now characterized as potential hydrocarbon sources and reservoir rocks. The Woodford is currently being produced in different basins by different companies such as: Newfield, Devon, Chesapeake, and Petroquest in the Arkoma basin, Range, Antero, Oracle Resources in the Ardmore basin, Devon and Cimarex in the Anadarko basin, among others (Wickstrom, 2008). Continuous advances in technology and a better understanding of the characteristics of these shale reservoirs make them more important from an economical point of view, hence the drilling and production activity continually increase in these non-conventional gas reservoirs.

The relatively low permeability of the shale formation makes its economically viable only through completion and fracturing of the target. The most common case is multi-staged hydraulic fracturing in horizontal wells which creates a fracture network that provides the permeability necessary for production (Comer, 1991; Mattews et al., 2007). The knowledge of the mechanical properties of the shale, taking into account the anisotropy present in these formations, is one of the key parameters for planning and execution of such processes.

Given their variable composition (their clay content tends to make them fissile) and fabric (layered nature), shale formations are treated as transversely isotropic materials from a mechanical point of view, behaving as homogeneous isotropic materials in the direction parallel to the bedding planes, and anisotropic in the direction perpendicular to the bedding planes. Although these are common characteristics of this rock type, all shale formations do not behave in the same way (Mattews et al., 2007; Slatt et al., 2008, Britt and Schoeffler, 2009). Having an understanding of the geological characteristics such as lithology variations, geochemistry, rock properties, and the relation between these parameters becomes essential when designing completion and development for these shale reservoirs (Rickman et al., 2008). Hence, there is a recent increase in proposed integrated methodologies or workflows that can improve well location and completion designs (Mattews et al., 2007; Slatt et al., 2008, Mitra et at., 2010).

The mechanical characteristics of shale formations can be investigated through laboratory analyses; however the required cored samples are often expensive, the tests are time consuming, and furthermore, difficult to perform given the challenges associated with this rock type. The fissile nature and the chemical reactivity of shale require an extra effort in processes such as core preservation and sample preparation. A model developed by the Geomechanics of Gas Shale Consortium (GGSC), which can quantify the anisotropic properties of these shale formations based only on its porosity and mineralogy, is an innovative approach that is worth further exploration. An analysis of the mechanical properties at different scales, using different tests that

provide a better understanding of the mechanical behavior of the rock, can then be helpful for the validation and calibration of such a model.

The natural fracture distribution is also critical for completion treatments such as hydraulic fracturing. Natural fractures may benefit stimulation treatments by reopening during fluid injection, acting as planes of weakness, hence allowing a bigger propagation of the induced fracture. They might also be detrimental if interconnected with underlying formations which are water saturated, acting as a "leak" for the injected fluid. According to the nature of the natural fractures (e.g. healed, opened, drill induced) these might either enhance or decay fluid flow and storage capacities of the free gas in the formation (Gale et al., 2007).

1.1 Significance

An understanding of the mechanical properties of shale formations is essential for several applications widely used in the petroleum industry. These include the seismic and/or the acoustic signature of rocks which are dictated by rock elastic properties; these properties control the propagation of acoustic waves through the medium. A better understanding of these properties provides meaningful input for seismic operations, improving methodologies used in seismic acquisition, processing and time/depth conversions, which in turn results in a more accurate interpretation and a better control on horizontal well placement (Banik, 1984; Winterstein, 1986; Tsvankin, 2005; Behera and Tsvankin, 2009; Slatt and Abousleiman, 2011). Furthermore, analyses such as amplitude variation with offset (AVO), seismic inversion and cross-borehole tomography are enhanced by understanding the anisotropic nature of shale formations and incorporating the effect of anisotropy into

such analyses (Carriot et al., 1992; Kim et al., 1993; Gallant et al., 2007; Tsvankin et al., 2009; Behura and Tsvankin, 2009;). Common analyses such as wellbore stability, where the knowledge of the mechanical properties is essential, as well as completion and hydraulic fracturing designs are enhanced by understanding and introducing the anisotropic character of these shale formations (Okland et al., 1993; Ekbote and Abousleiman, 2006; Al-Tahini and Abousleiman, 2008; Higgins et al., 2008).

An integration of geological characteristics and rock properties has become more popular in order to define the optimal completion intervals/locations or so called "sweet spots" (Warpinski et al., 2009; Baihly et al., 2010). Several methodologies have been proposed for such purpose (Britt and Schoeffler, 2009). This thesis follows the workflow proposed by Slatt et al. (2008).

1.2 Objectives

The main objective of this thesis is to analyze the geomechanics response of the Woodford Shale, taking into account geological characteristics such as the lithofacies description and the mineralogy data available as points for analysis. A mechanical characterization is available after completing a laboratory analysis of the Woodford consisting of different tests and coupling these results with those of previous studies performed for the same formation (Tran, 2009). This will provide meaningful insights into the geomechanics response of the Woodford Shale. More specific objectives include:

- To extend the previous laboratory analysis by using new tests such as the Brazilian test and the Three Point Bending test, both under tensile regime, as well as to extend the previous tests to the upper and lower member of the Woodford Shale. The

objective is to characterize the anisotropic elastic properties of the Woodford and the relation between these results and geological characteristics such as fabric and mineralogy of some of the lithofacies composing the Woodford.

- To investigate the stress dependency of the poroelastic properties by utilizing an innovative procedure developed by the PoroMechanics Institute called the Inclined Direct Shear Testing Device (IDSTD^{TM}) which uses a smaller sized sample with different size specifications than the one proposed by the classical laboratory standards (Abousleiman et al, 2010). Finally for the laboratory analysis, it is necessary to compare the results obtained by the classical approach and the one proposed in this thesis for validation of the results and further analyses.

- To complete the lithofacies description of the preserved samples that were tested by using thin sections and following the previous interpretation (Buckner, 2011) developed for the area of study.

- All the resulting analyses will be integrated into an interdisciplinary workflow that can serve as reference for future analyses yet to be performed.

1.3 Area of Study

The Woodford Shale is Late Devonian (~385 MA) to early Mississippian (~360 MA) in age. It has been identified in the past as an important source rock of hydrocarbons (Chong and Smith, 1984). It is present in the south central part of Oklahoma throughout almost the entire Arkoma Basin where it currently produces oil and gas (Slatt et al., 2010). Figure 1.1 presents the location of the completed wells in the Woodford by 2007 in Oklahoma as well as Pontotoc County which is the location for this study.

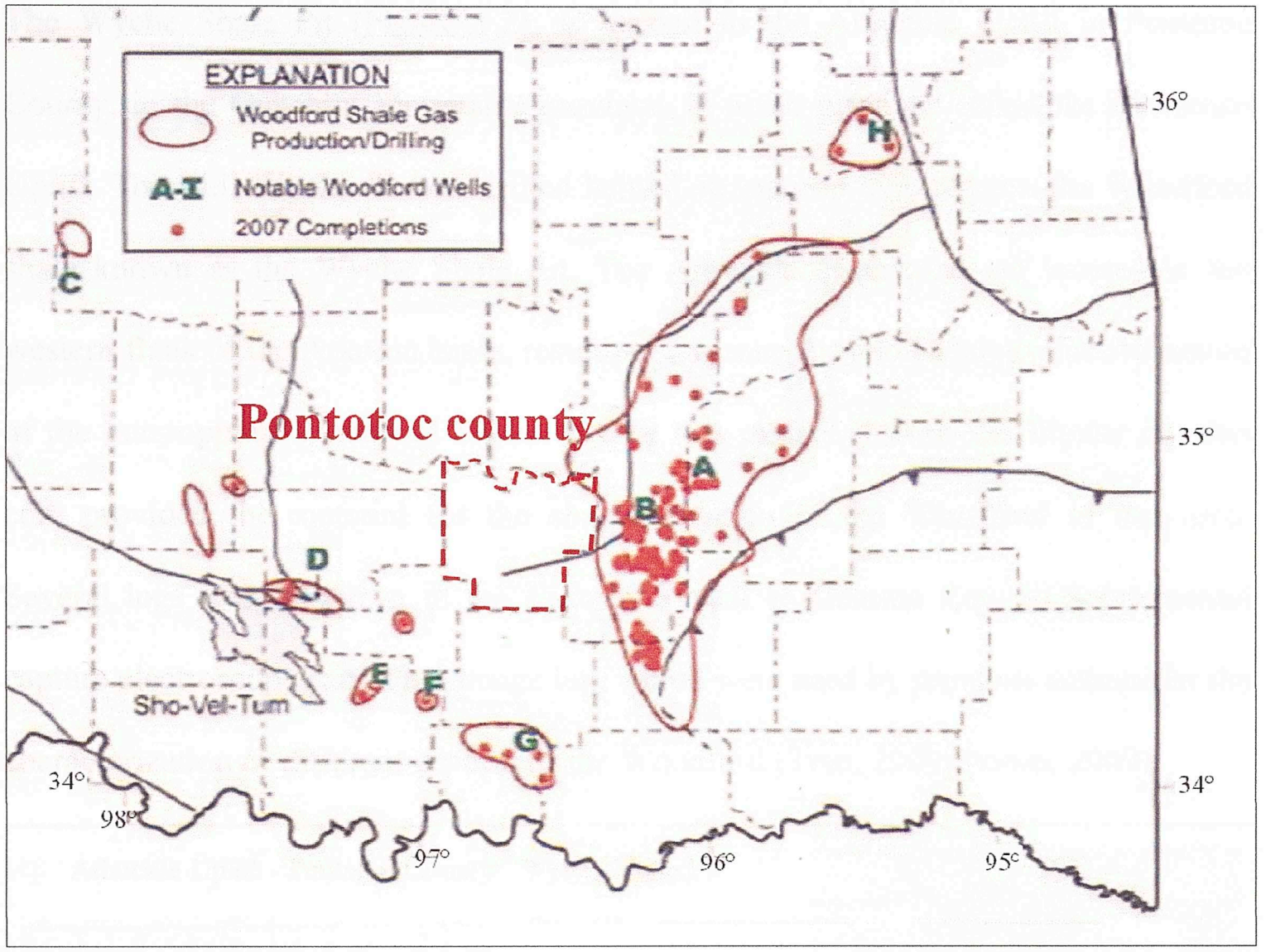

Figure 1.1. Woodford completed wells by 2007, dotted circle shows the location of Pontotoc County (Modified from Wickstrom, 2008).

It is subdivided into Upper, Middle and Lower Woodford members, all these first described by Ellison (1950) in the Permian basin where the Woodford Shale is also present. It contains kerogen type I and more abundant, marine type II (Cardott, 2001). Its minimum total organic content is 0.8, positioning it as potential source rock (defines as more than 0.5) (Hester et al., 1990). This value might vary regionally within its three different members. According to Miceli (2010) in central and southeastern Oklahoma the Woodford Shale is organic-rich, with TOC values ranging from 3.63% to 11.42%, having the Middle Woodford the highest organic richness of all three members.

The Wyche Shale Pit (Figure 1.2), is located in the Arbuckle Uplift in Pontotoc County, in the Ouachita Mountains province, in a sub province called the Lawrence Uplift. The well Wyche #1 was drilled behind an outcrop that exposes the Woodford shale known as the Wyche Shale Pit. The Arbuckle Mountains are located in the western flank of the Arkoma basin, resulting in a zone for good analogy for evaluation of the outcropping Woodford Shale. A core was extracted from the Wyche #1; this core provided the material for the characterization of the Woodford in this area. Several logs were also run in the open hole such as Gamma Ray, ECS (elemental capture electroscopy) and FMI image log, which were used by previous authors for the characterization of different aspects of the Woodford (Tran, 2009, Portas, 2009)

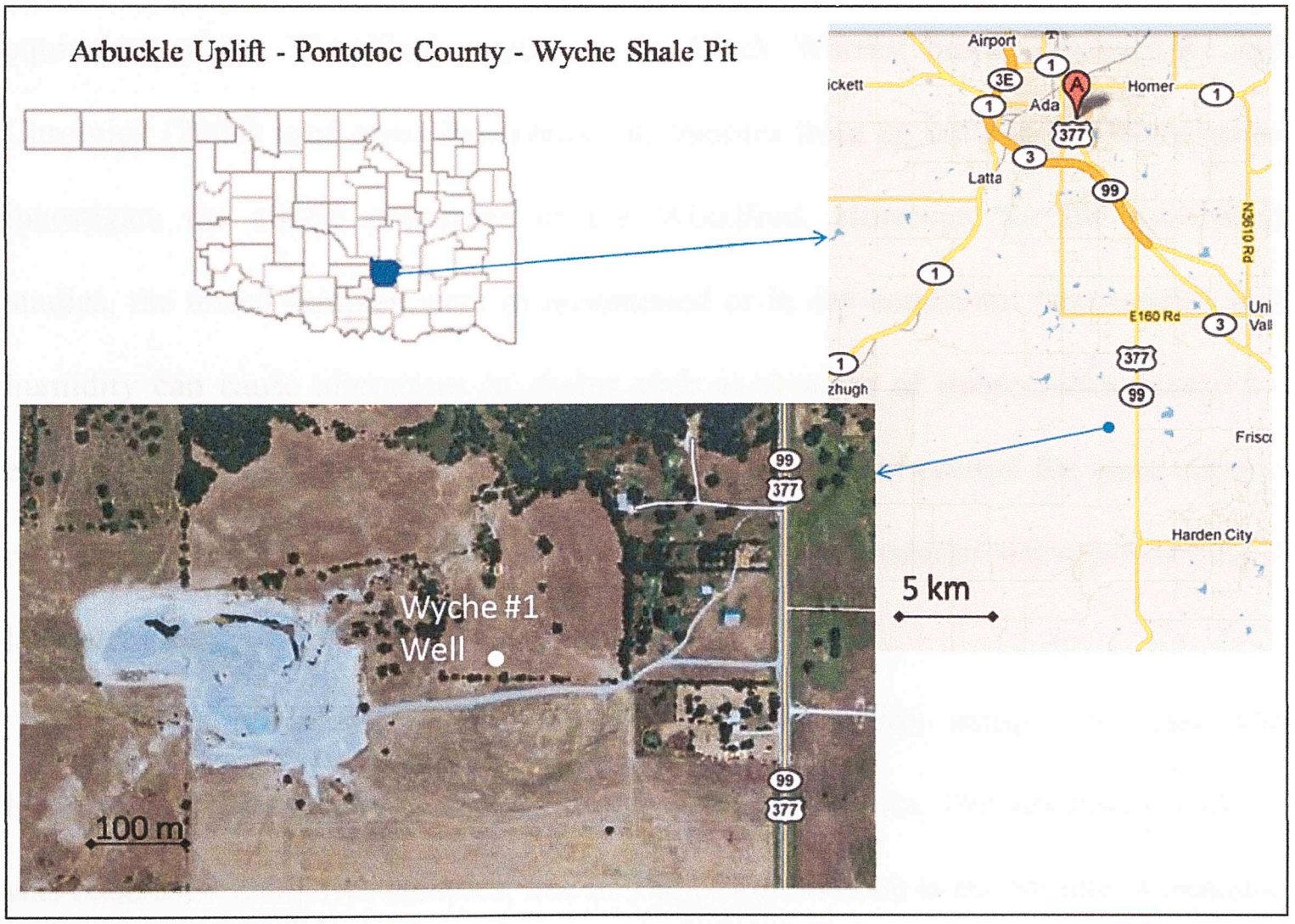

Figure 1.2. Location the area of study, the Wyche shale pit and the behind quarry well drilled (Wyche #1). Source: Google Maps, Accessed June, 2010.

1.4 Previous Laboratory Studies

In the past, extensive work was done in studying the mechanical properties of the so called oil-shale, mainly in the Green River formation of Western U.S (Chong and Smith, 1984). Several other authors have investigated the elastic properties of several gas-shale formations around the world. These results serve as the bases for future analyses to be done (Vernik and Nur, 1992; Amadei et al., 1983; Hornby, 1994; Jhonston and Christensen, 1995; Claesson and Bohloli, 2002; Scott and Abousleiman, 2005; Abousleiman et al., 2007; Abousleiman et al., 2010).

Johnston and Christensen (1995) conducted acoustic measurements in order to explore the seismic anisotropy of samples from a member of the Chattanooga Shale, an equivalent of the Woodford present in the Black Warrior basin. Zeszostarski and Chromick (2004) used nano indentation on samples from an outcrop in Oklahoma to investigate the elastic properties of the Woodford. However, for the mentioned studies, the tested samples were in unsaturated or in dry condition. Temperature and humidity can cause alterations in shales such as creation of microcracks caused by expansion (Horsrud, 2001). Therefore these studies may not present the most reliable results. The proper preservation of the shale samples is essential when performing a laboratory analysis

Tran (2008) completed a geomechanics characterization using well logs and laboratory tests in preserved samples from the Woodford core. The laboratory analysis was conducted using two samples, one in The Upper and one in the Middle Woodford. Some of the tests and results provided the basis for some of the analyses performed in this work.

2 GEOLOGICAL SETTING

2.1 Stratigraphy Summary

The Woodford Shale was deposited on top of a major regional unconformity separating it from the Hunton group, interpreted as a shallow marine carbonate ramp deposit, and overlain by late Mississippian limestone (Springer group) and the Caney shale (Figure 2.1, Arbenz, 2008).

The Woodford Shale is considered a "hot shale" given its high radioactivity (high gamma ray response), which is due to high concentrations of Uranium preserved on clays and organic matter during low sedimentation rates in deep waters (Hester et al., 1990).

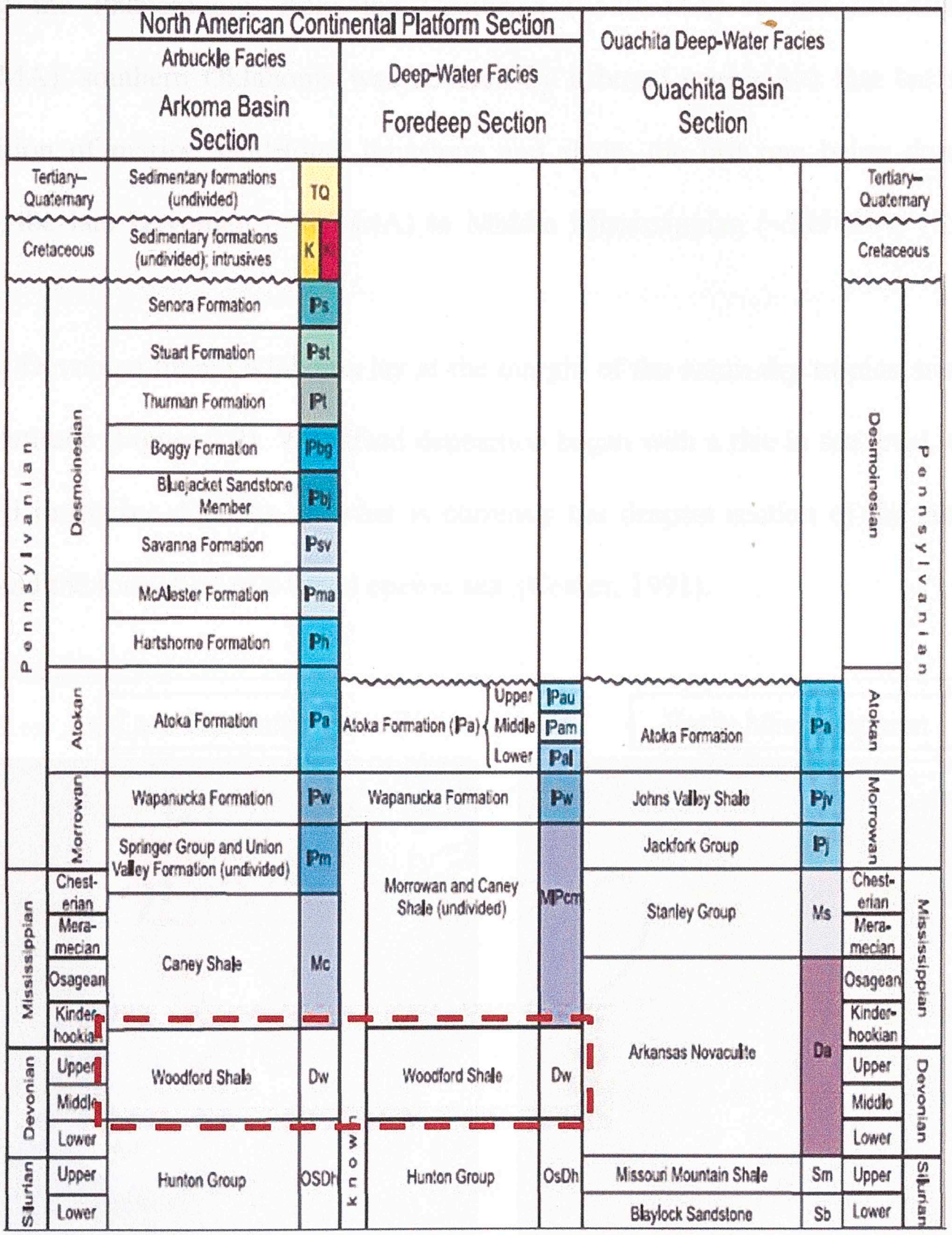

Figure 2.1.Stratigraphic column of Arkoma and Ouachita basins (Modified from Arbenz 2008).

The Woodford Shale is composed mainly of black shale. Some other common lithologic types include chert, siltstone, dolostone and lighter colored shale. The Woodford is interpreted as a deep marine deposit (Comer, 2005), having three informal members: the Lower, Middle and Upper Woodford (Hester et al., 1990).

During the Phanerozoic, from the Cambrian (~540 MA) to the Mississippian (~360MA), southern Oklahoma was covered by a broad epeiric sea that led to the deposition of marine sandstone, limestone and shale, the last one being dominant during the late Devonian (~385 MA) to Middle Mississippian (~345 MA) (Comer, 1991).

During Devonian time, Oklahoma lay at the margin of the warm dry tropics, near 15° south latitude (Figure 2.2). Woodford deposition began with a rise in sea level, which resulted in marine deposits on what is currently the deepest section of the Arkoma basin and the formation of a broad epeiric sea. (Comer, 1991).

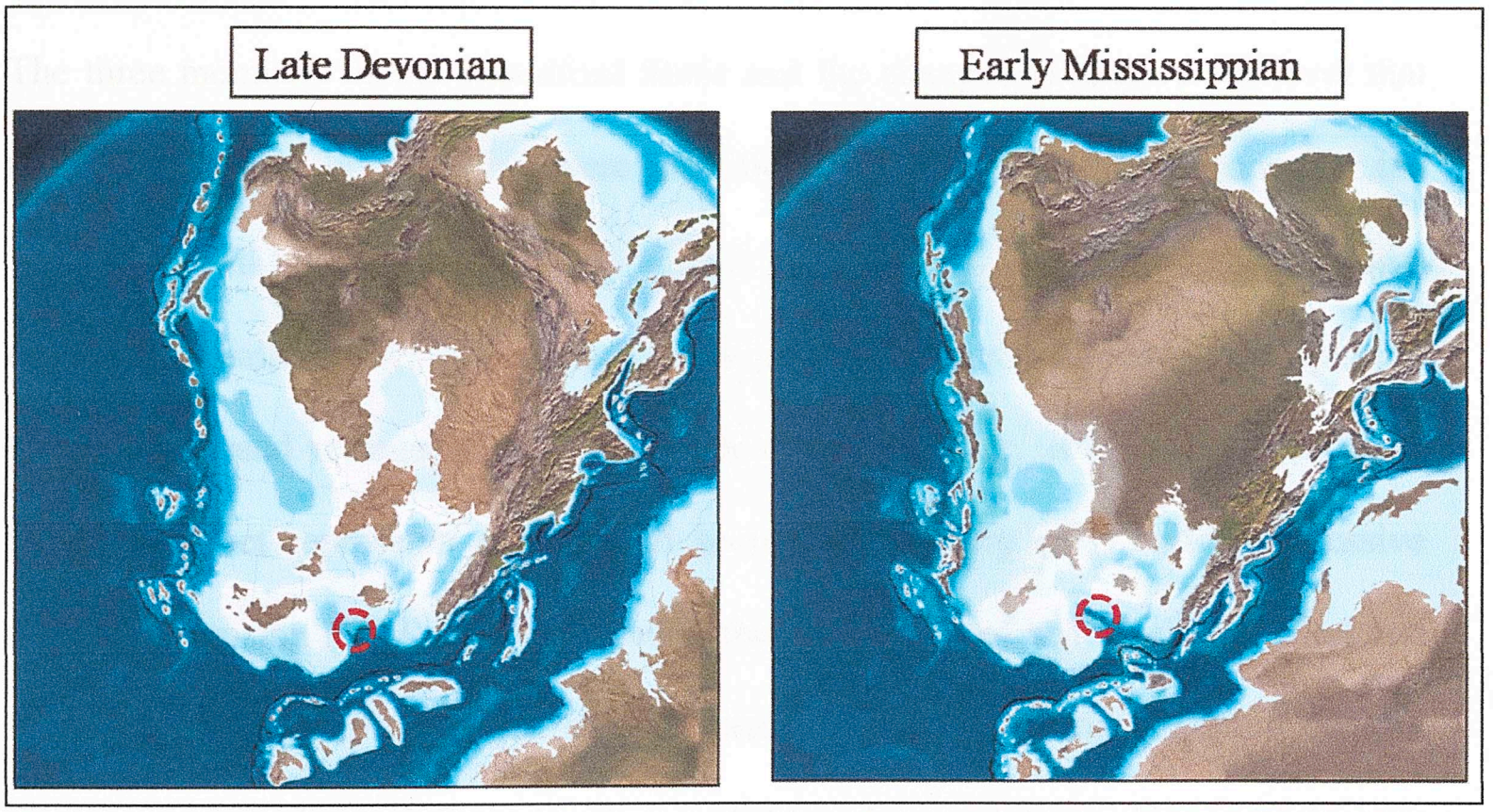

Figure 2.2.North American paleographic maps during times of deposition of the Woodford shale, the dotted circle represents the area of study. Modified from Blakey (2011). Source: http://jan.ucc.nau.edu/~rcb7/nam.html accessed November, 2010.

The lower Woodford was deposited in a proximal setting during a period of sea level transgression. The Middle Woodford was deposited in a more distal setting during continued transgression, hence its finer grained, and more organic rich nature. It has

the highest total organic content (TOC) of the three members. The Upper Woodford was deposited during continued progradation; it has the lowest TOC content of the three members (Slatt et al., 2010).

The high organic content of the Woodford shale resulted from the following factors: First, upwelling water "flooded" the epeiric seas resulting in high biological activity with high nutrient content. Second, high evaporation rates which are typical of shallow equatorial environments resulted in highly saturated brines, which became density stratified, restricting the oxygen content of the bottom water (Comer, 2005). The Woodford was then deposited during a major transgressive – regressive cycle with secondary cycles of higher order superimposed (Slatt et al., 2010).

The three members of the Woodford Shale and the changes in relative sea level that took place during its deposition were identified by Gamma Ray log response for the Wyche #1 well by Buckner (2011) (Figure 2.3). One major transgressive – regressive cycle with smaller cycles of superimposed higher order were associated with episodic progradation and retrogadation during deposition (Buckner, 2011). The Woodford-Hunton contact represents a combined sequence boundary (SB) and transgressive surface of erosion (TSE), associated with the early stage of sea level rise (Slatt and Rodriguez, 2010). Figure 2.3 shows interpreted brittle-ductile couplets at the parasequence scale as defined by Slatt and Abousleiman (2011). The brittle/ductile classification will be discussed in the results and discussion chapter of this thesis.

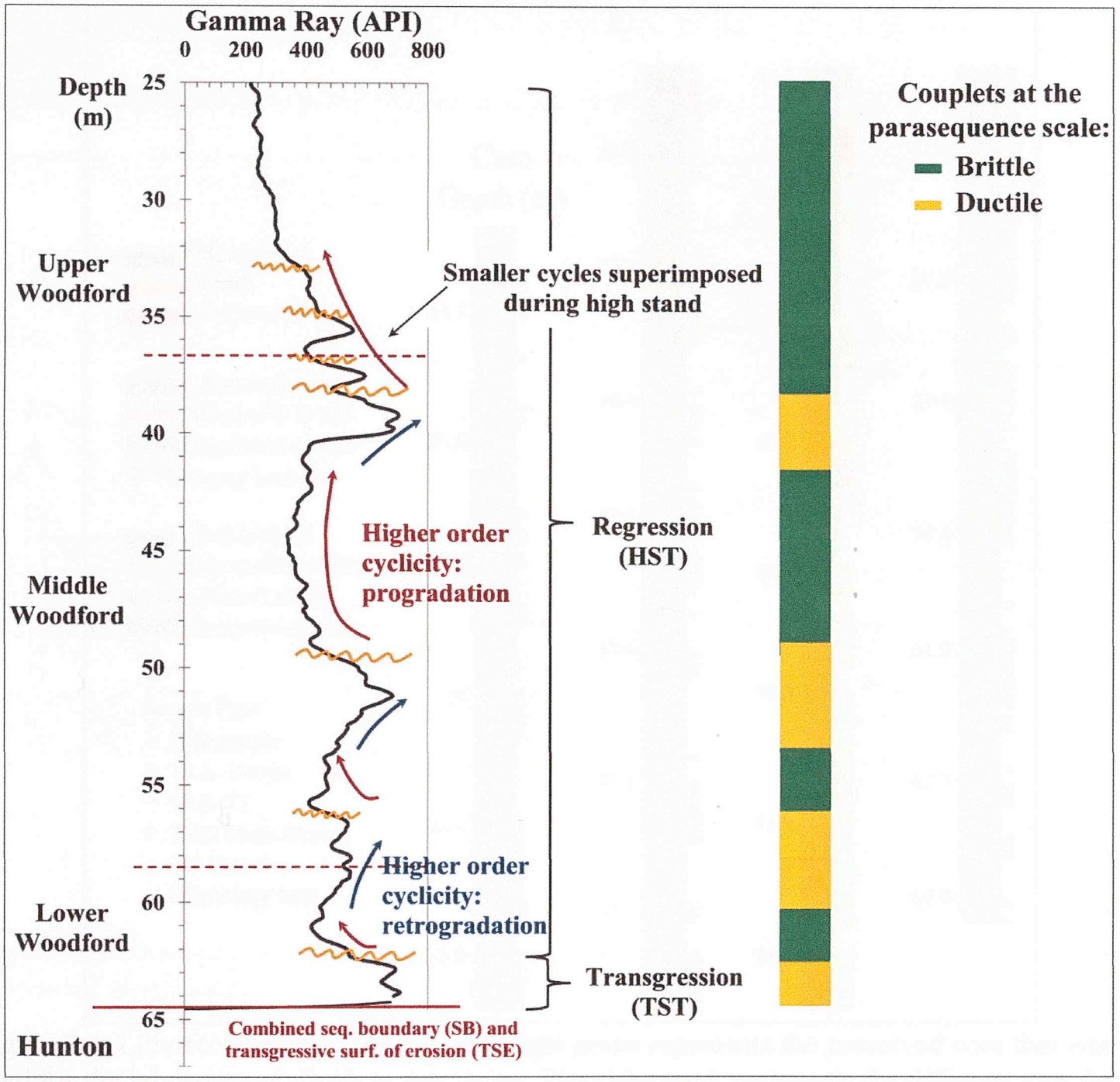

Figure 2.3.Sequence Stratigraphic framework for the Woodford Shale based on Gamma Ray (Interpretation from Buckner, 2011; Slatt and Rodriguez, 2010).

A lithofacies description using the recovered core was completed by Buckner (2011). Eight primary and 2 secondary lithofacies (very small percentage of the core) were identified: 1) siliceous laminated shale, 2) siliceous laminated shale that fines upward or coarsens upward, 3) calcareous laminated shale, 4) gray-black laminated shale, 5) light gray laminated shale, 6) black laminated shale, 7) nodular laminated shale, 8) blue-gray laminated shale, 9) coal and 10) unconsolidated mud (Figure 2.4).

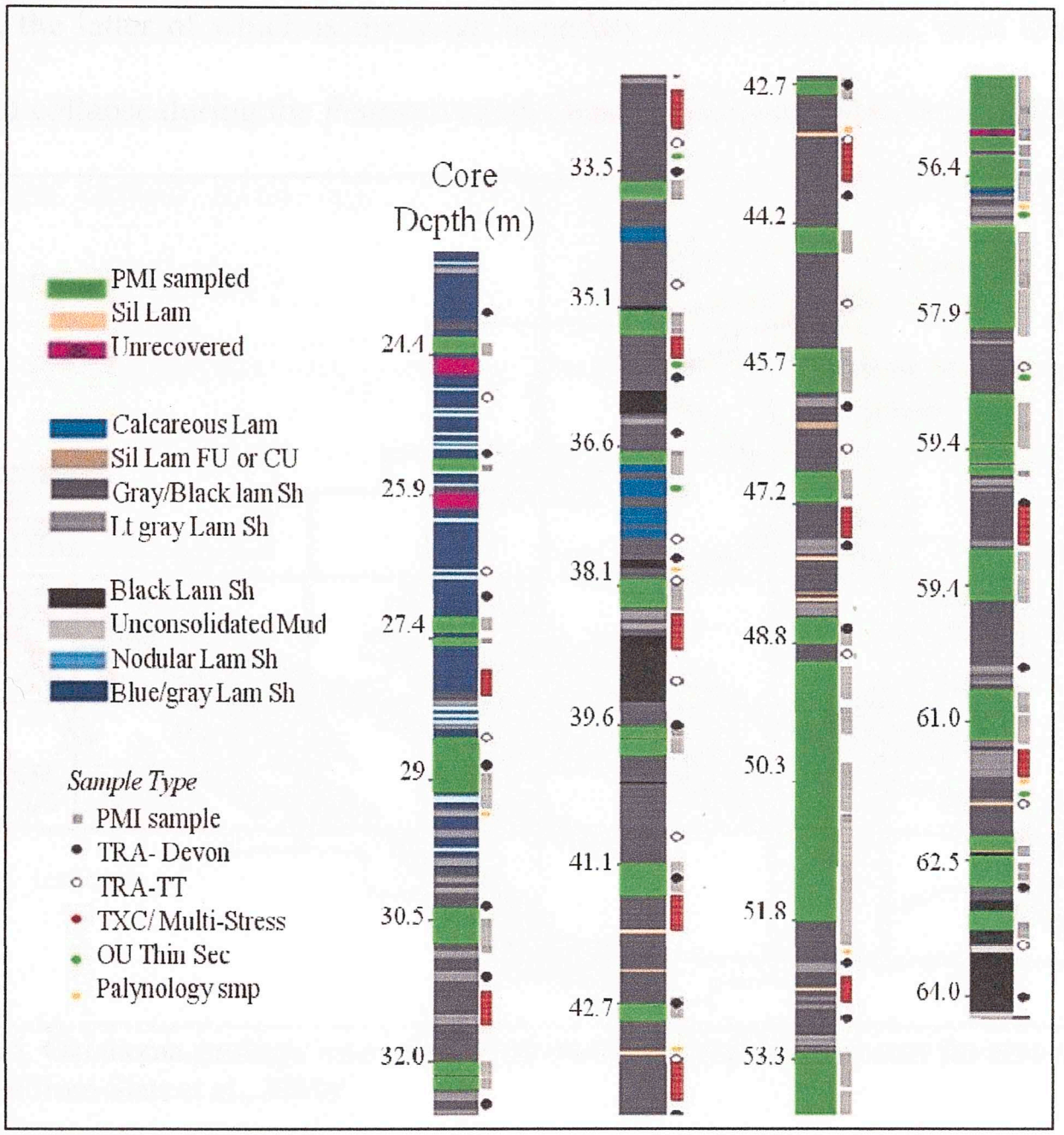

Figure 2.4. Lithofacies interpretation, the bright green represents the preserved core that was used for the laboratory analysis in this thesis. The right track represents the different uses for the core (Modified from Buckner, 2011).

2.3 Structure Summary

The Arbuckle Mountains are located in south central Oklahoma. The area of study is located east of the Arbuckle Mountains in the Lawrence Uplift sub province. The main structural features of the area include the Ahloso fault, which is a normal fault oriented at 90° Azimuth and dipping north. The Stonewall fault is a normal fault oriented at approximately 45° Azimuth and dipping southwest (Suneson, 1997). The Arkoma basin is located east of the Lawrence Uplift. The Woodford is currently under development and produces oil and gas in this area. The Lawrence Uplift and the Frank

Graben, the latter of which is the south boundary of the study area, were formed by tensional collapse during the Pennsylvanian Ouachita orogeny (Slatt, et al., 2010).

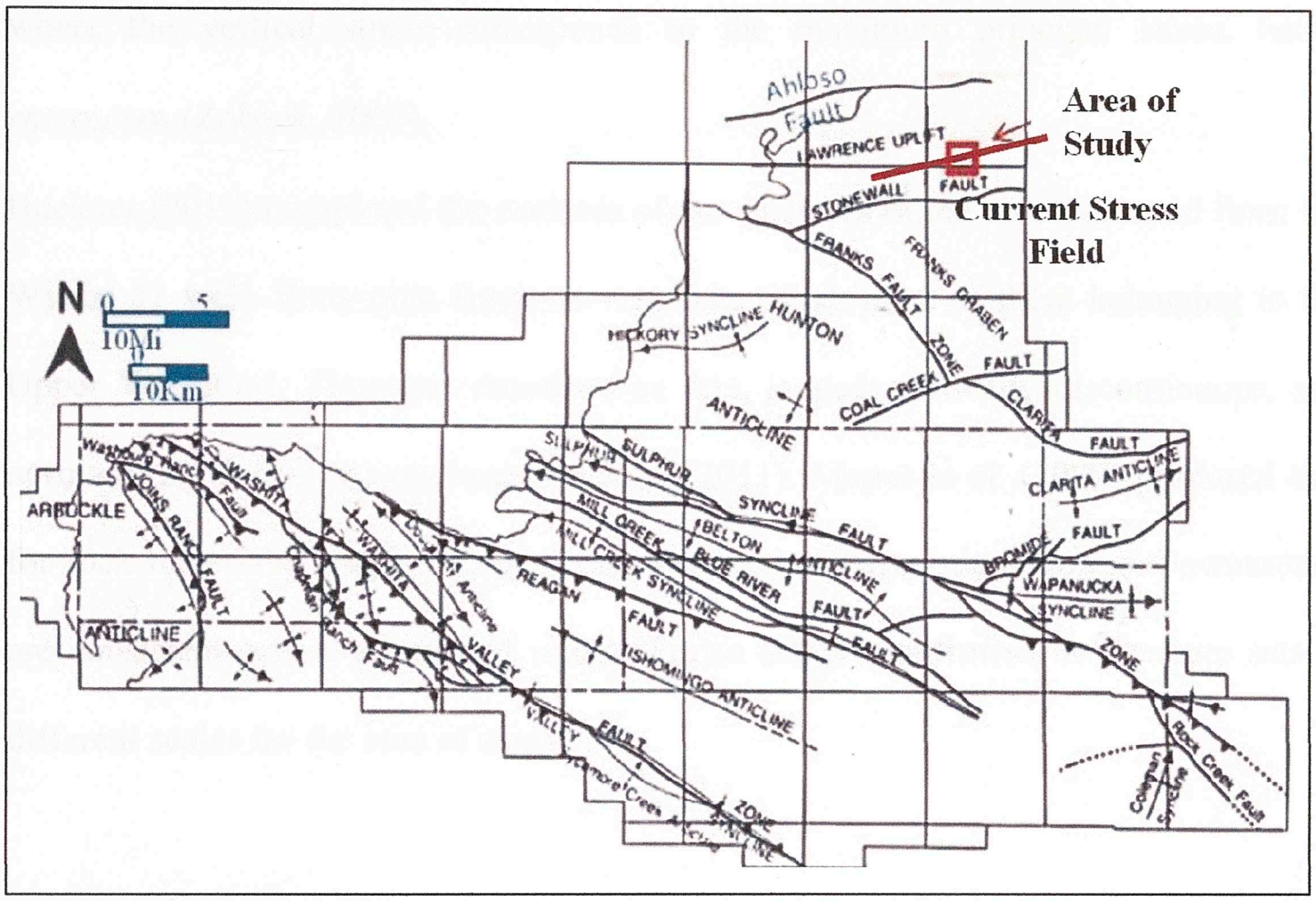

Figure 2.5. Oklahoma geologic map, presenting main structural features near the area of study (Modified from Slatt et al., 2010).

The progressive uplift of the strata induced compression stresses in the lower section of the anticline that was being developed, as well as tensional stresses in the upper section of the anticline, hence creating a series of tensional fractures in the upper section of the Woodford (Portas, 2009; Slatt et al., 2010).

The fracture patterns were characterized by Portas (2009). There are two extensional fracture sets. The first set is "systematic" due to similar orientation (median value of 90° Azimuth), morphology and the generally even spacing between them. The second set is "nonsystematic" due to their irregular geometry and irregular morphology. The fractures of the second set normally intersect those of the first set. The second set of

fractures has a median orientation of 45° Azimuth which is the direction of today's maximum horizontal stress. The area is under a normal fault regime (Portas, 2009), where the vertical stress corresponds to the maximum principal stress, hence $\sigma_v > \sigma_H > \sigma_h$ (Zoback, 2007).

Buckner (2011) completed the analysis of the fractures in the core extracted from the Wyche #1 well. Sixty-nine fractures were identified, most of them belonging to the Upper Woodford. These are described as thin, jagged, vertically discontinuous, and normally 2.5-5 (1-2 in) cm long (Buckner, 2011). Marret et al. (1999) proposed that for rock materials, within an equal set, fracture intensity, orientation and occurrence are consistent across a range of scales. Portas (2009) confirmed the fracture sets at different scales for the area of study.

3. GEOMECHANICS CHARACTERIZATION

3.1 Background

3.1.1 Theoretical considerations

Given its nature, the Woodford Shale, like other inherently layered materials, can be mechanically characterized as a transverse isotropic (TI) material. The material presents a rotational elastic symmetry along the vertical axis and the elastic properties are isotropic along the plane of isotropy (Figure 3.1), for this case, the x,y plane (Chong et al., 1979). Although anisotropy can be caused by different characteristics of the media such as oriented fractures, this work is only focused on the intrinsic anisotropy developed by the layered characteristic of shale.

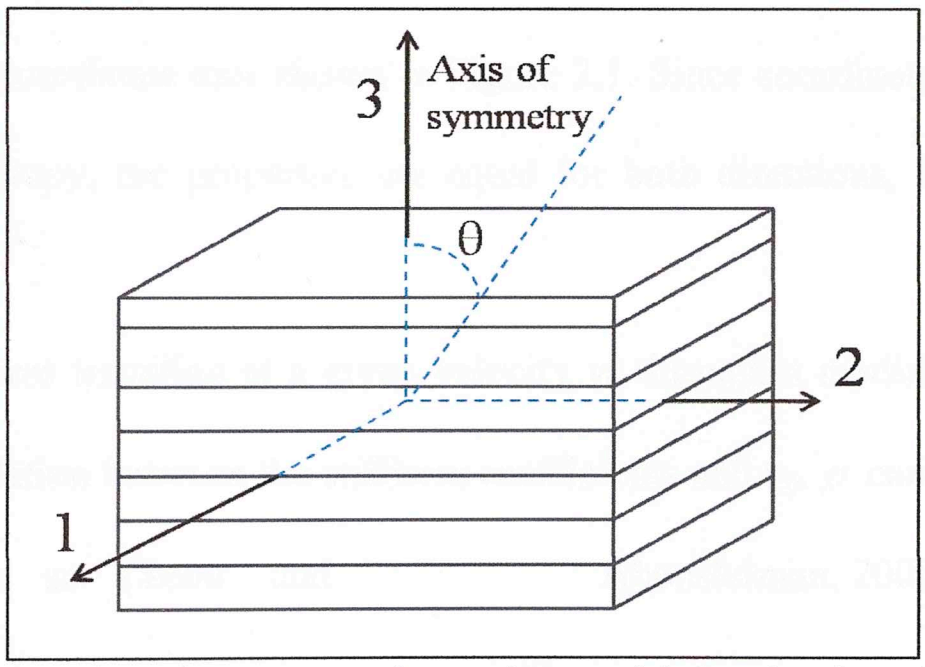

Figure 3.1. Representation of a transverse isotropic material showing the axis of symmetry.

The equations governing the strain (σ_{ij}) – stress (ε_{ij}) relation for transverse isotropic medium considering the poroelastic case are completely defined by 7 poroelastic parameters, as follows (Abousleiman and Cui, 1998):

$$\begin{bmatrix}\sigma_{11}\\ \sigma_{22}\\ \sigma_{33}\\ \sigma_{12}\\ \sigma_{13}\\ \sigma_{23}\end{bmatrix}=\begin{bmatrix}C_{11} & C_{12} & C_{13} & 0 & 0 & 0\\ C_{12} & C_{11} & C_{13} & 0 & 0 & 0\\ C_{13} & C_{13} & C_{33} & 0 & 0 & 0\\ 0 & 0 & 0 & C_{44} & 0 & 0\\ 0 & 0 & 0 & 0 & C_{66} & 0\\ 0 & 0 & 0 & 0 & 0 & C_{66}\end{bmatrix}\begin{bmatrix}\varepsilon_{11}\\ \varepsilon_{22}\\ \varepsilon_{33}\\ 2\varepsilon_{12}\\ 2\varepsilon_{13}\\ 2\varepsilon_{23}\end{bmatrix}+\begin{bmatrix}\alpha_{11}\\ \alpha_{11}\\ \alpha_{33}\\ 0\\ 0\\ 0\end{bmatrix}P \tag{3.1}$$

Where α_{ij} represents the Biot's coefficient, a measure of the effectiveness by which the fluid in the pore space repels the applied stress on the bulk. P represents the pore pressure of the fluid in the pore space.

In this notation, the stiffness coefficients (C_{ij}) are used to describe the elastic properties of the rock, an approach widely used in geophysics for borehole and seismic acoustic analyses (Johnston and Christensen, 1995). The subscripts make reference to the coordinate axis shown in Figure 2.1. Since coordinates 1 and 2 define the plane of isotropy, the properties are equal for both directions, for instance C_{11}= C_{22}.

For an elastic wave traveling at a given velocity v_{ij} through a medium having a bulk density ρ, the relation between the stiffness coefficients and v_{ij}, ρ can be described for a TI medium as (Scott and Abousleiman, 2005):

$$C_{33}=\rho V_{P0}^2 \tag{3.2}$$

$$C_{11}=\rho V_{P90}^2 \tag{3.3}$$

$$C_{66}=\rho V_{S90}^2 \tag{3.4}$$

$$C_{44}=\rho V_{S0}^2 \tag{3.5}$$

$$C_{12}=C_{11}-2C_{66} \tag{3.6}$$

$$C_{13}=-C_{44}+\frac{\sqrt{(\cos^2\theta C_{33}+\sin^2\theta C_{44}-\rho V_{P\theta}^2)(\sin^2\theta C_{11}+\cos^2\theta C_{44}-\rho V_{P\theta}^2)}}{\sin\theta\cos\theta} \tag{3.7}$$

Where the subscripts P and S denote compressive and shear waves, respectively and the second subscript represents the angle θ, which is the angle taken with respect to the axis of symmetry as represented in Figure 3.1. Hence, V_{S0} represents the velocity of a shear wave traveling in the direction of the axis of symmetry, direction 3 in Figure 3.1, and V_{P90} represents the velocity of a compression wave traveling in the direction of isotropy, direction 1 and/or 2 in Figure 3.1.

A different notation utilizing more widely recognized elastic moduli such as Young's modulus (E), Poisson's ratio (υ), and Shear Modulus (G) can also be used. For a transverse isotropic material the elastic moduli will be defined in two directions, one parallel to the axis of symmetry and the other along the plane of isotropy. The equations relating the stiffness coefficients with the dynamic poroelastic moduli for a TI material are (Abousleiman and Cui, 1998):

$$E_1 = \frac{C_{11}^2 C_{33} - C_{12}^2 C_{33} - 2C_{11}C_{13}^2 + 2C_{12}C_{13}^2}{C_{11}C_{33} - C_{13}^2} \tag{3.8}$$

$$E_3 = \frac{C_{11}C_{33} + C_{12}C_{33} - 2C_{13}^2}{C_{11} + C_{12}} \tag{3.9}$$

$$v_3 = \frac{C_{13}}{C_{11} + C_{12}} \tag{3.10}$$

$$G_1 = C_{66} \tag{3.11}$$

$$G_3 = C_{44} \tag{3.12}$$

$$\alpha_{11} = \alpha_{22} = 1 - \frac{C_{11} + C_{12} + C_{13}}{3K_s} \tag{3.13}$$

$$\alpha_{33} = 1 - \frac{C_{33} + 2C_{13}}{3K_s} \tag{3.14}$$

Where the subscripts correspond to the coordinate axis presented in Figure 3.1, and *Ks* is the bulk modulus of the matrix, having a value of 36 GPa (Scott and Abousleiman, 2005).

3.1.2 The Geomechanics of Gas Shale Consortium Simulator (GGSCS)

The GGSCS is an approach that scales up the anisotropic elastic and poroelastic properties of natural composites; for this case, shale. Breaking down the component of shale rocks to a nano-scale where no variation is observed between samples, then scaling this behavior to the macro-scale by describing the interaction between these fundamental composites makes it possible to model a macroscopic behavior relevant for engineering applications.

According to Abousleiman et al. (2007), shale is a clay supported material composed of a continuous clay phase that presents a transverse isotropic behavior at different scales. The model, supported by laboratory analyses, confirms the assumptions inherent to the model (Ulm and Abousleiman, 2006; Ortega et al., 2007): "*shales are nanogranular composite materials whose mechanical properties are dictated by particle to particle contact and by packing density characteristics, the much stiffer mineral properties play a secondary role*".

The model is based on the main constituents of the rock (evaluated by its mineral composition) and its morphology, which is quantified by porosity. These are collapsed into a property defined as clay packing density, which describes how tightly the clay particles are packed together. The model then upscales the poroelastic

properties based on the clay packing density, the inclusion volume fraction (f_{inc}) and the organic volume fraction (f_{org}). These can be calculated as follows (Abousleiman Y. N. et al., 2010):

$$\eta = 1 - \frac{\phi}{(1 - f_{inc})} \tag{3.15}$$

$$f_{inc} = (1-\phi)\frac{\sum_{k=1}^{total\_non\_clay}(m_k / \rho_k)}{\sum_{k=1}^{total\_non\_clay}(m_k / \rho_k) + \sum_{l=1}^{total\_clay}(m_l / \rho_l) + \sum_{n=1}^{total\_organic}(m_n / \rho_n)} \tag{3.16}$$

$$f_{org} = \frac{\sum_{n=1}^{total\_organic}(m_n / \rho_n)}{\sum_{l=1}^{total\_clay}(m_k / \rho_k) + \sum_{n=1}^{total\_organic}(m_n / \rho_n)} \tag{3.17}$$

Where m is the mass percentage, available from mineralogy data, and ρ is the density. The subscripts "k", "l" and "n" represent the inclusion (non-clay), clay and organic material composing the rock respectively.

3.2 Cores Preservation and Samples Selection

The retrieved cores from the well were divided with one set of cores immediately submerged at the well site in non-reactive Mulitherm PG-1 mineral oil to avoid alterations to the rock properties. The second set was stored in boxes and slabbed for core analysis and description (Figure 3.2). To avoid the effect of possible weathering of the Woodford formation due to seasonal fluctuations of the water table in the area (Abousleiman et al., 2009) or a possible change in lithology at the Woodford-Mayes

boundary (Slatt et al., 2010), only the interval below 26.5 m (86.9 ft) was employed for the laboratory analysis to guarantee the reliability of the results.

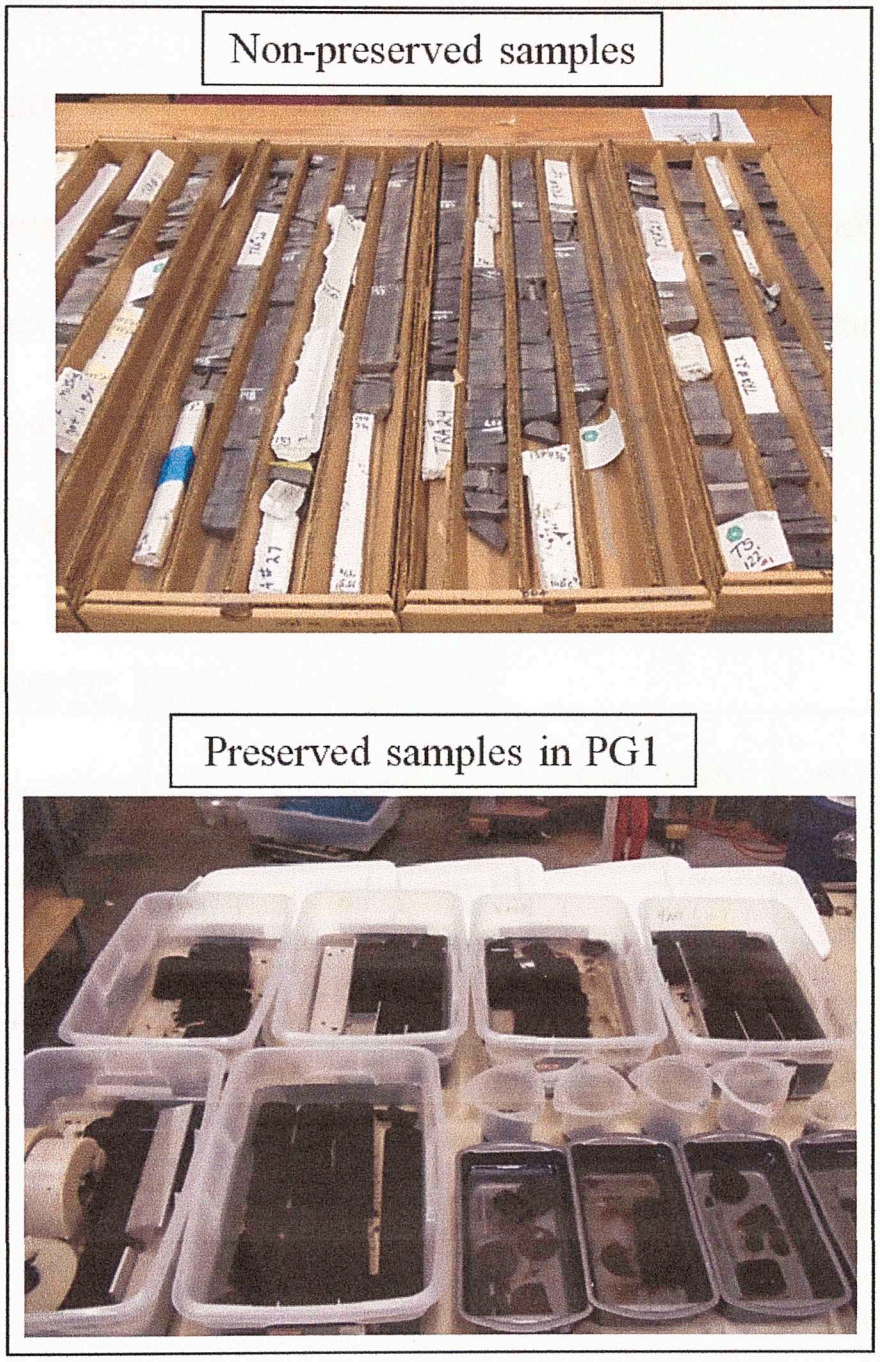

Figure 3.2. Retrieved core from Wyche #1 well. Samples are stored in boxes (non-preserved) and submerged in PG1 (preserved).

In addition, only core samples that met the following criteria were selected for testing: (1) the core is intact without any visible weak bedding planes or fractures, (2) the core does not exhibit any calcite or pyrite concretions (Abousleiman et al., 2007).

The selection of the samples was also based on available mineralogy data and lithofacies description. Since the samples were in a preserved condition, a general

lithofacies description was not possible before the laboratory analysis. For this reason only samples where mineralogy data was available at a nearby depth were chosen. The mineralogy was later confirmed by XRD measurements on the tested samples and a lithofacies description was completed using thin sections.

Figure 3.3 presents the ECS mineralogy log for the Woodford interval; the interpretation of the three members is shown. Table 3.1 presents the XRD mineralogy data from Chevron-HETC Mineral Analysis Laboratory. The samples were randomly selected for the entire interval (Tran, 2008).

Table 3.1. Chevron-HETC, XRD mineralogy

Depth (m)	Qtz	Kspar	Plag	Total Carb	Pyr	SUM NON-CLAY	SUM CLAY	Amorphous
33.67	53	2	1	3	3	62	20	18
36.68	63	1	1	12	5	82	5	13
36.87	36	0	0	38	20	94	2	4
39.93	37	2	3	2	9	54	30	17
41.33	35	2	2	20	2	62	25	14
44.35	34	2	2	7	9	54	30	16
47.03	36	2	3	8	4	54	32	15
47.24	31	0.5	3	7	13	55	28	18
50.60	33	2	3	3	10	51	31	18
53.35	34	2	3	7	6	52	36	12
54.69	44	1	2	13	7	67	18	15
56.64	27	2	3	14	3	49	37	14
57.90	36	1	4	4	1	46	43	11
61.21	39	2	3	8	7	59	26	15
64.25	28	2	2	4	6	42	43	15

XRD mineralogy presenting mass percentages of the main components. The amorphous percentage corresponds to the remaining percentage to achieve 100%.

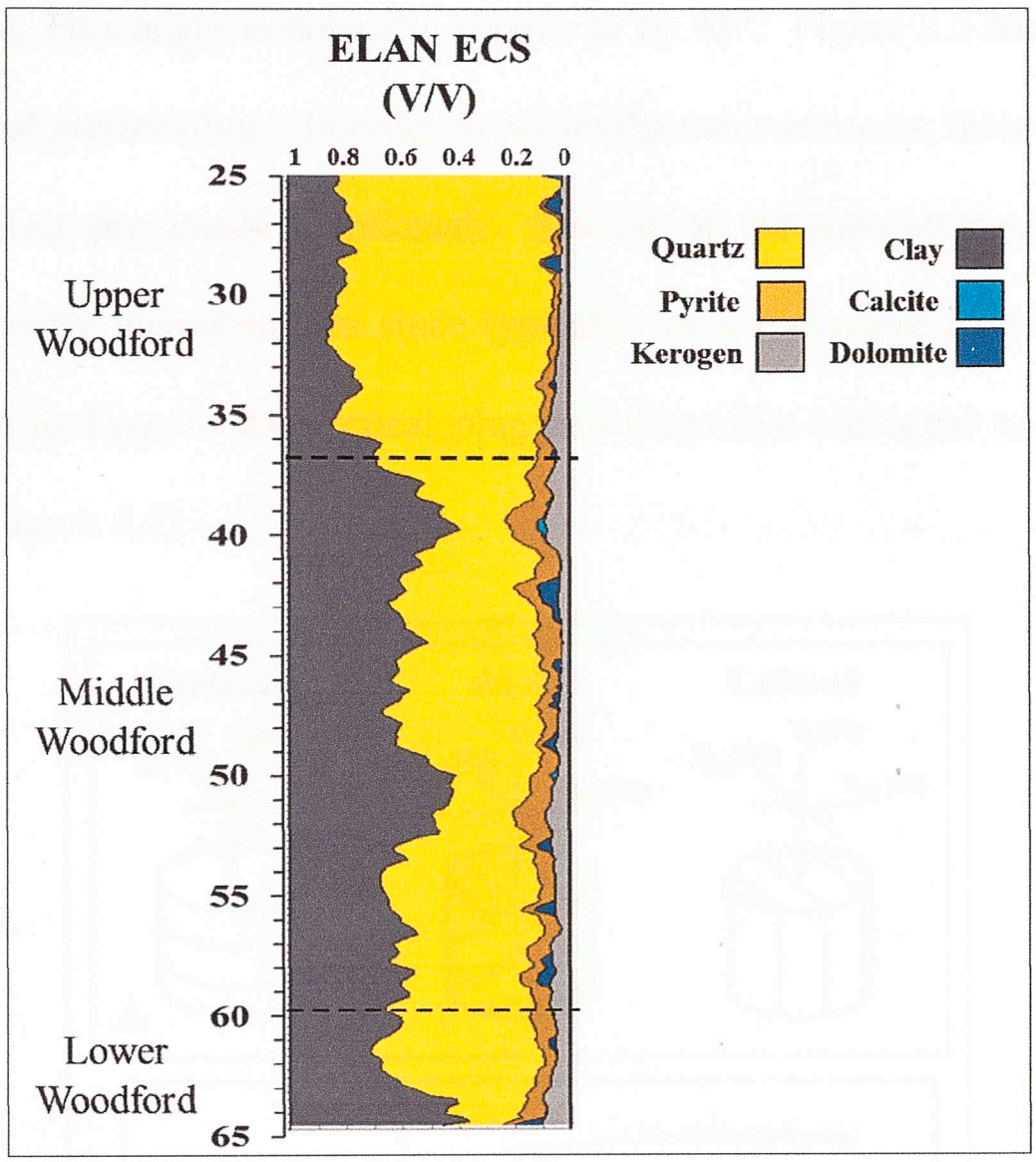

Figure 3.3. ECS mineralogy for the Woodford interval in the Wyche #1 well. Provided by Schlumberger.

3.3 Mechanical Characterization

3.3.1 Ultrasonic Pulse Velocity (UPV) measurements

Non-destructive UPV measurements are useful in order to investigate the wave propagation and anisotropy of shale samples (Vernik and Nur, 1992; Johnston and Christensen, 1994; Hornby, 1994; Johnston and Christensen, 1995). For transversely isotropic materials, five independent elastic moduli are necessary for a complete characterization of the transverse isotropic elastic behavior (Eq.2.1). Therefore, five different acoustic velocities in three directions are required, two coinciding with the symmetry axis and plane of isotropy (Figure 3.1; 3.5) and one taken at an angle

between those. This angle is normally chosen to be 45°. Figure 3.5 shows the setup for the classical methodology. In order to obtain the measurements, three plugs are cut in the directions previously mentioned. Several of the measurements shown are redundant velocity measurements since typically for a transverse isotropic material, $V_{SH(0)}$ is equal to $V_{SV(0)}$ in the vertical plug and these two are equal to $V_{SV(90)}$ in the lateral plug (Figure 3.5).

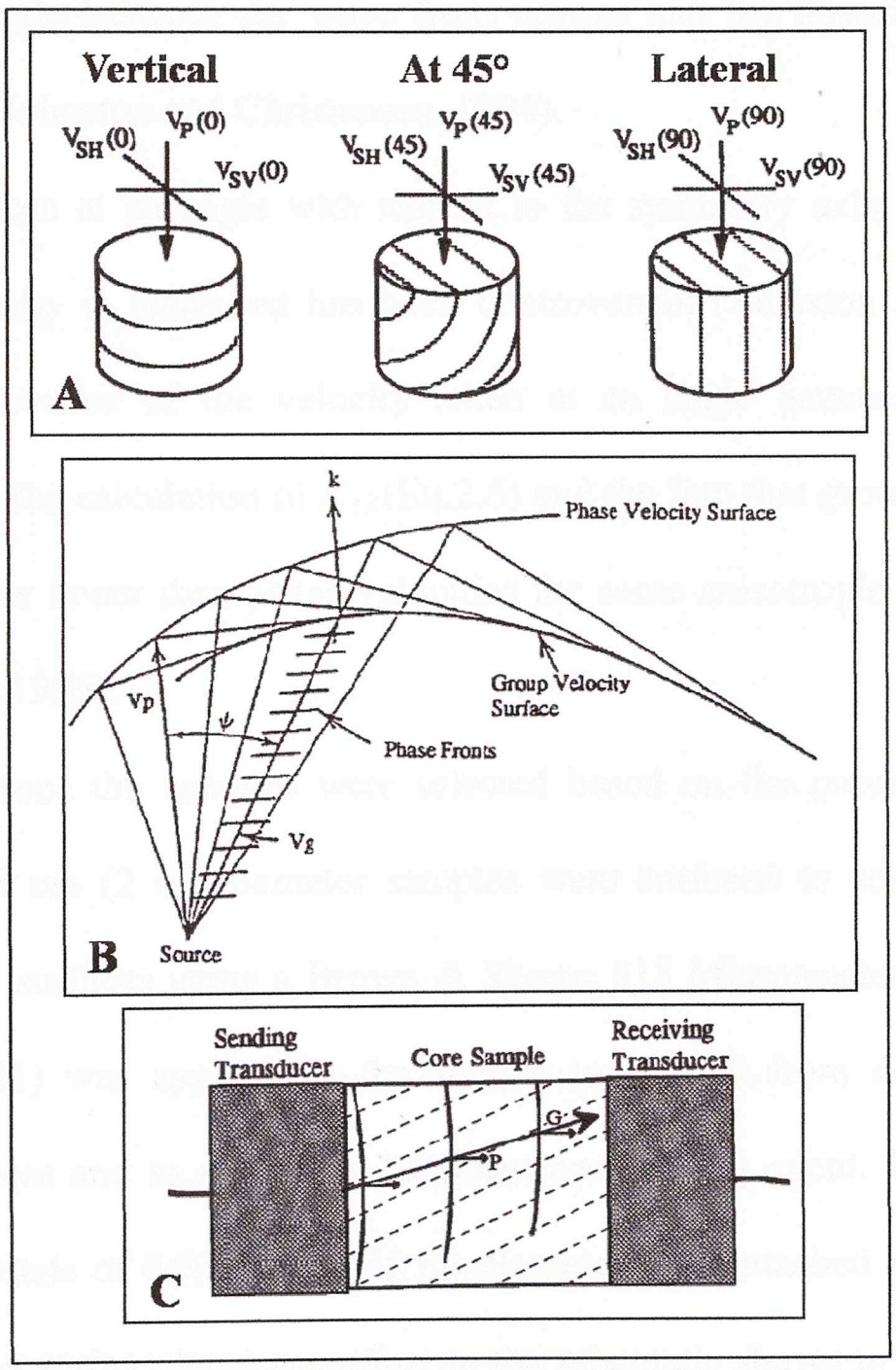

Figure 3.4. A. Schematic of the classical methodology for ultrasonic velocity measurements, showing the three plugs required (Modified from Vernik and Nur, 1992). B. Relationship between group and phase velocities (Johnston and Christensen, 1994). C. Schematic showing the classical setup with two transducers and the assumed wave propagation (Johnston and Christensen, 1995).

For the cores taken along the symmetry axis and plane of isotropy, the group velocity is equal to the phase velocity. At the laboratory scale, group velocity (Figure 3.4) implies point sources and receivers, where the velocity of an envelope of plane waves is measured. Phase velocity implies planar waves, where the velocity of a wave front is measured (Thomsen, 1986). Figure 3.4 presents the relationship between group and phase velocities, k represents the normal vector to the group velocity surface, and ψ represents the angle between the wave front normal and the direction of the group velocity vector (Johnston and Christensen, 1994).

For velocities taken at an angle with respect to the symmetry axis, the predicament over which velocity is measured has been controversial (Johnston and Christensen, 1994). The relevance of the velocity taken at an angle between the symmetry directions lies in the calculation of C_{13} (Eq.2.6) and the fact that group velocities have been proven to be lower than phase velocities for some anisotropic shales (Johnston and Christensen, 1995).

For this study, once the samples were selected based on the previously mentioned criteria, the 5.08 cm (2 in) diameter samples were surfaced to achieve parallelism between the end surfaces using a Brown & Sharpe 818 Micromaster surface grinder. Mineral oil (PG1) was applied on the sample to keep it from drying during the preparation process and to serve as a lubricant and cooling agent. Pairs of 600 kHz piezoelectric crystals of 0.635 cm (0.25 in) diameter were attached to the surfaces of the sample with a spring clamp according to the schematic shown in Figure. 3.5. Two thin lead foils were used for acoustic coupling between the crystals and the rock. Pulses of direct current of 300V from a Panametrics 5077PR Square Wave

Pulser/Receiver were used to excite the crystals; the vibration of the crystals induces an elastic wave that travels through the medium. The velocities were chosen to be V_{P0}, V_{P90}, $V_{P\theta}$ and V_{S90}, V_{S0} $V_{S0\text{-}1}$, $V_{S0\text{-}2}$ as illustrated in Figure. 3.5. As previously mentioned, $V_{S0\text{-}2}$ is a redundant measurement taken to confirm the transversely isotropic characteristic of Woodford Shale (Scott and Abousleiman, 2005). For the angular velocity, the edges of the sample were surfaced to generate an area big enough to clamp the piezoelectric crystals.

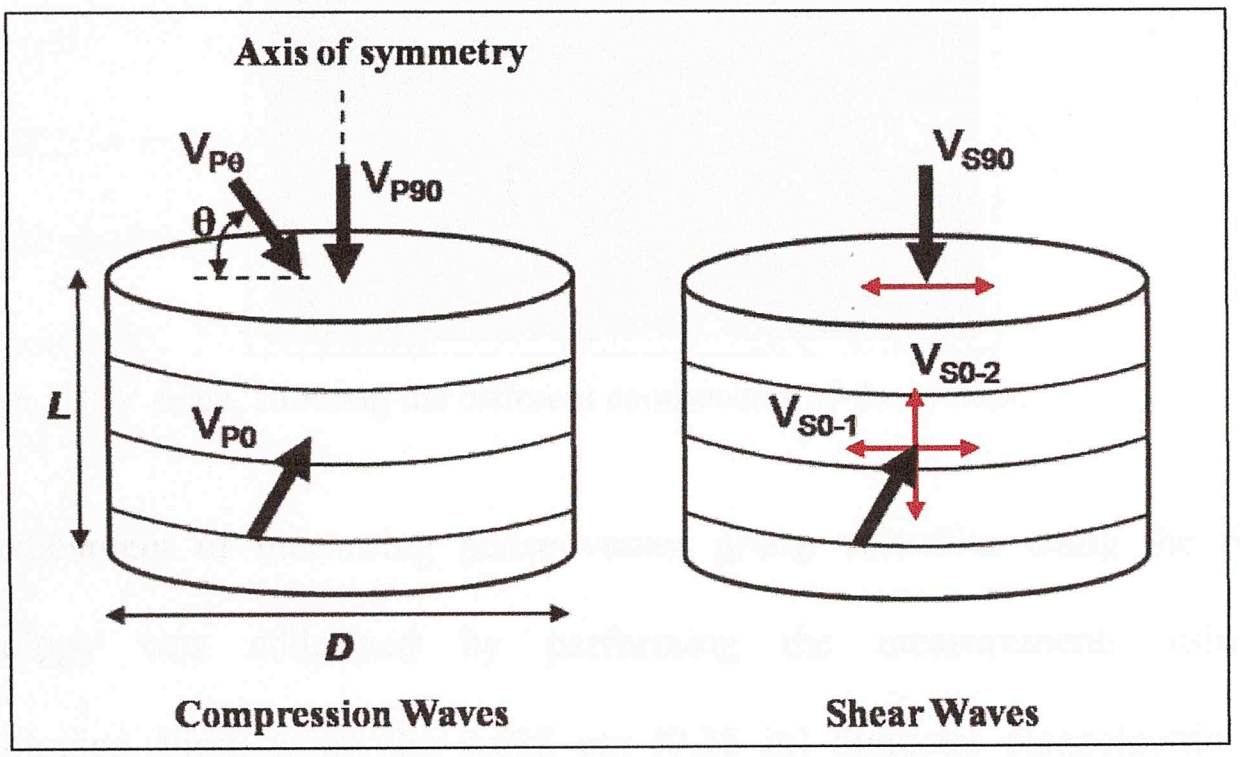

Figure 3.5. Schematic of UPV wave velocity measurements, showing direction and polarization of the velocities to be measured.

The associated wave forms were recorded using a Tektronix TDS 3024B Digital Phosphor Oscilloscope, which allows further analysis of the wave form and selection of the arrival times. Figure 3.6 presents the setup for the ultrasonic velocity measurements.

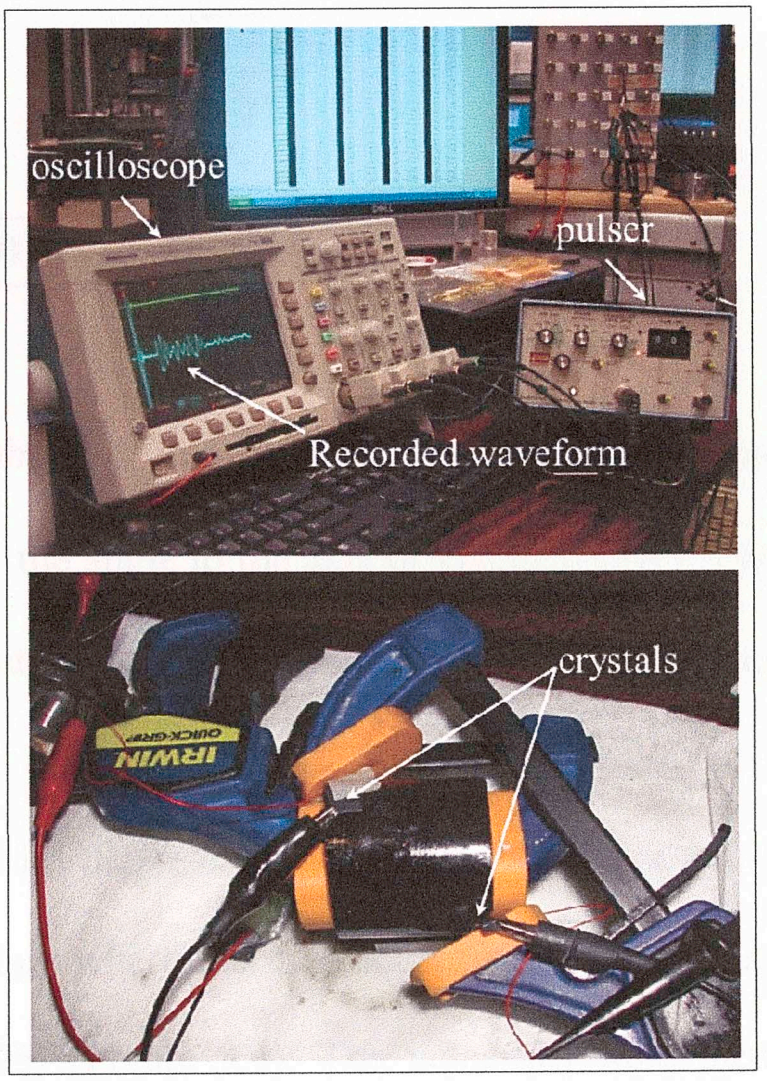

Figure 3.6. UPV setup, showing the different components of the system.

The predicament of measuring phase versus group velocities using the proposed methodology was addressed by performing the measurements using both methodologies. First, using the 0.635 cm (0.25 in) diameter piezoelectric crystals clamped on the sample, the full set of elastic stiffness coefficients and the phase velocity surfaces were calculated using the follow equations (Johnston and Christensen, 1994):

$$A = C_{11} \sin^2 \theta - C_{33} \cos^2 \theta + C_{44} \tag{3.18}$$

$$B = \sqrt{\left[(C_{11} - C_{44}) \sin^2 \theta + (C_{44} - C_{33}) \cos^2 \theta\right]^2 + (C_{13} + C_{44})^2 \sin^2 2\theta} \tag{3.19}$$

$$V_P = \sqrt{\frac{A + B}{2\rho}} \tag{3.20}$$

$$V_{SV} = \sqrt{\frac{A-B}{2\rho}} \tag{3.21}$$

$$V_{SH} = \sqrt{\frac{0.5(C_{11}-C_{12})\sin^2\theta + C_{44}\cos^2\theta}{\rho}} \tag{3.22}$$

Where ρ represents the bulk density. The phase velocities present the velocity of a wave as a function of the angle to the axis of symmetry (θ). Two plugs of 1cm (0.78 in) diameter were cut in different orientations from the same sample; the angles selected were 30° and 60° (Figure 3.7). The velocities were measured using the same setup and 2.54 cm (1 in) diameter piezoelectric crystals of 600 kHz, which followed the classic methodology where the transducer approaches the sample size (Johnston and Christensen, 1995) (Figure 3.4). The velocities were then compared with the theoretical phase velocities for those particular angles using the phase velocity surfaces.

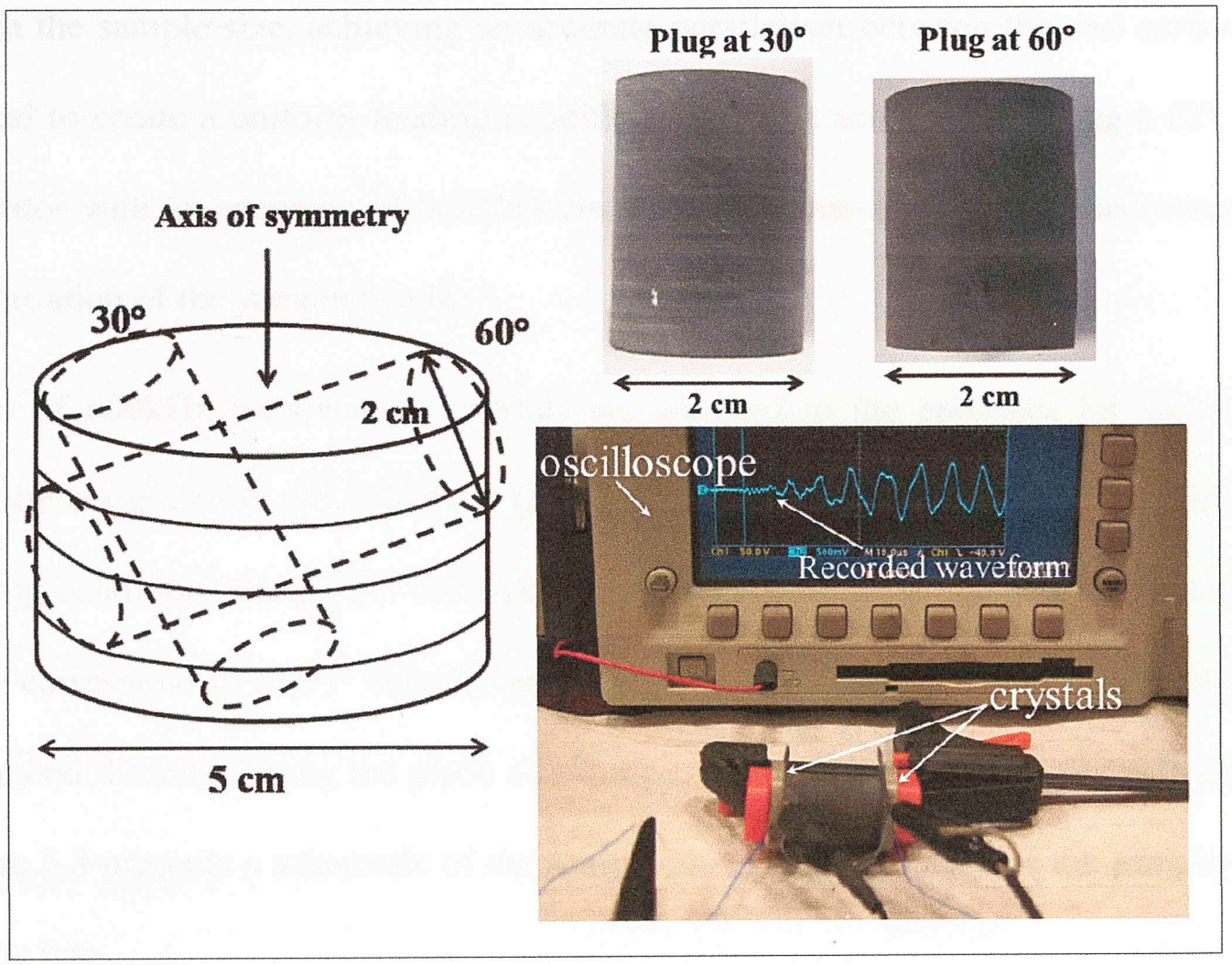

Figure 3.7. Schematic of plug cutting, samples, and setup for the UPV classical approach.

3.3.2 Standard Methodology, Uniaxial Compressive Test

The uniaxial compressive test is based on the unidirectional compression of a specimen with a specific geometry at a given loading rate (Fjaer, et al., 1992). This test allows the calculation of the elastic moduli and the investigation of the compressive strength of the rock (Hudson and Harrison, 1997).

A 5 cm (2 in) diameter sample was selected for this test at a depth of 50.18 m (164.63 ft). Furthermore, given the lack of a geological description beforehand, two samples for XRD were taken at the top and the bottom of the selected interval in order to evaluate the relative homogeneity of the core. The core was prepared to a length of 10.2 cm (4 in) following the same procedure described for the UPV core preparation.

Given the sample size, achieving an accurate parallelism between the end surfaces is critical to create a uniform loading condition. This was achieved by using a SPI Dial indicator with an accuracy of 0.00254 cm (0.001 in) that allows the measurement of the variation of the sample length.

A set of 600kHz piezoelectric crystals are attached to the end-caps for measuring acoustic compression (*P*) and shear (*S*) velocities in the vertical direction at different loading conditions during the test. Also, a set of crystals were attached to the sample; these correspond to one *P* velocity and two perpendicularly polarized *S* velocities in the lateral direction along the plane of isotropy, and one *P* velocity at an angle of 45°. Figure 3.8 presents a schematic of the sample along with an image of the sample used for the test.

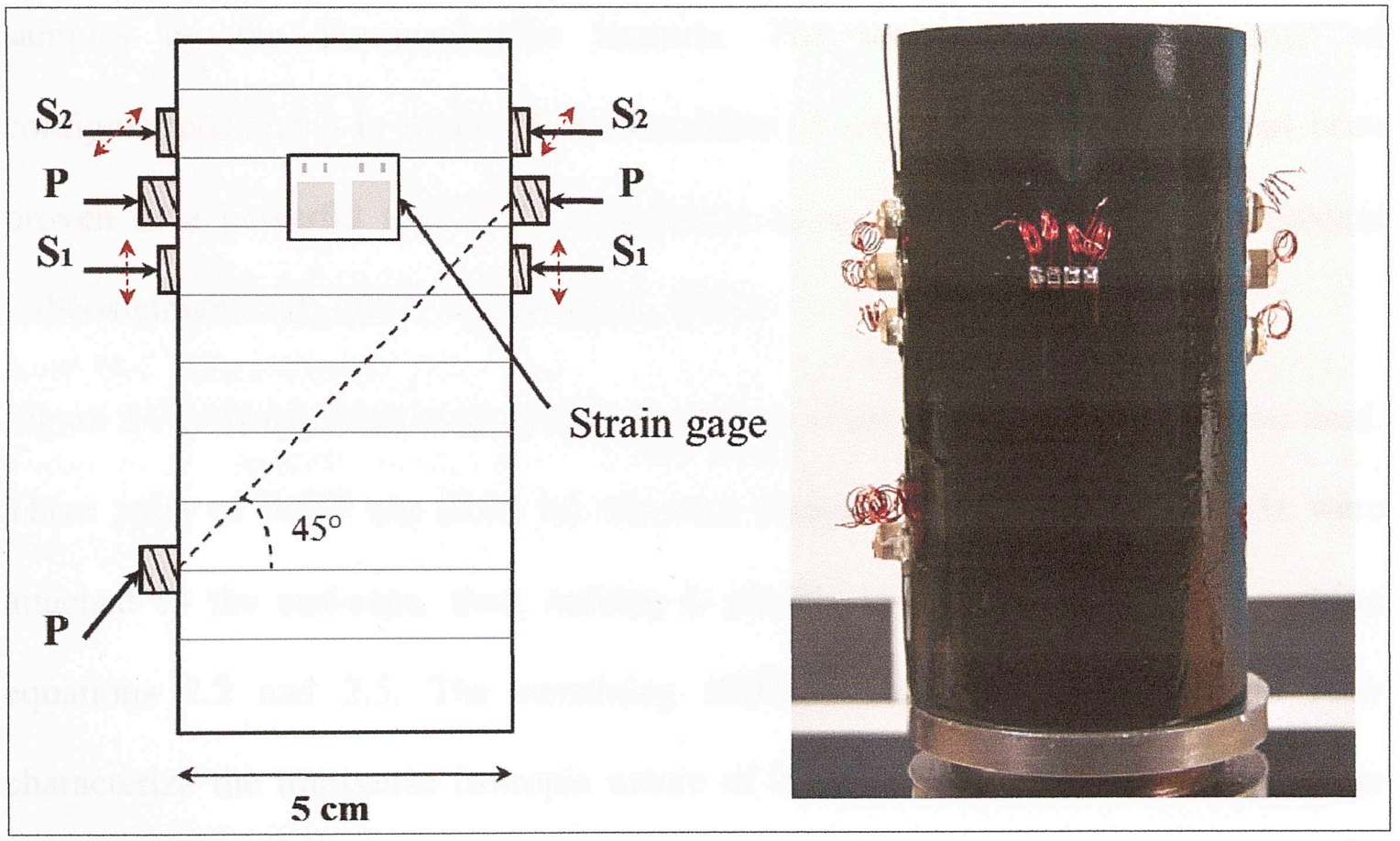

Figure 3.8. Schematics of the unconfined compressive test sample, image of the prepared sample for the test.

An MTS 810 loading frame was used to apply a compressive load to the stack. The test was carried out at a constant displacement rate of 0.000254 cm/min (0.0001 in/min). The displacement rate was chosen so it can be compared with tests performed for the same interval in the past (Abousleiman et al., 2007). A load cell was located between the stack and the loading frame in order to record the loading directly on the stack. One dual strain gage and two single strain gages perpendicularly oriented were located 180° apart on the periphery of the sample in order to measure both axial and lateral strain. Acoustic velocities were measured every 5337.9 N (1200 pounds) during the test, which represents increments of about 2.69 MPa (390 psi).

3.3.3 New approach. Inclined Direct Shear Testing Device (IDSTD^{TM}).

The IDSTD^{TM} was designed for the mechanical characterization of small-sized samples by the Poromechanics Institute. The tool allows a wide-range of configurations and it is applicable to a number of analyses. The procedure has been proven as a powerful tool in the assessment of shale's laboratory characterization (Abousleiman et al., 2007; Nguyen et al., 2008).

Figure 3.9 (Abousleiman et al., 2008), presents a schematic of the configuration used. Three pairs of 0.635 cm (0.25 in) diameter piezoelectric crystals of 2 MHz were attached to the end-caps, thus, making it posible to calculate C_{44} and C_{33} using equations 2.2 and 2.5. The remaining stiffness coefficients necessary to fully characterize the transverse isotropic nature of shale are modeled using an inversion technique developed by Tran (2009), which uses randomized maximum liklihood RML (Abousleiman et at., 2010).

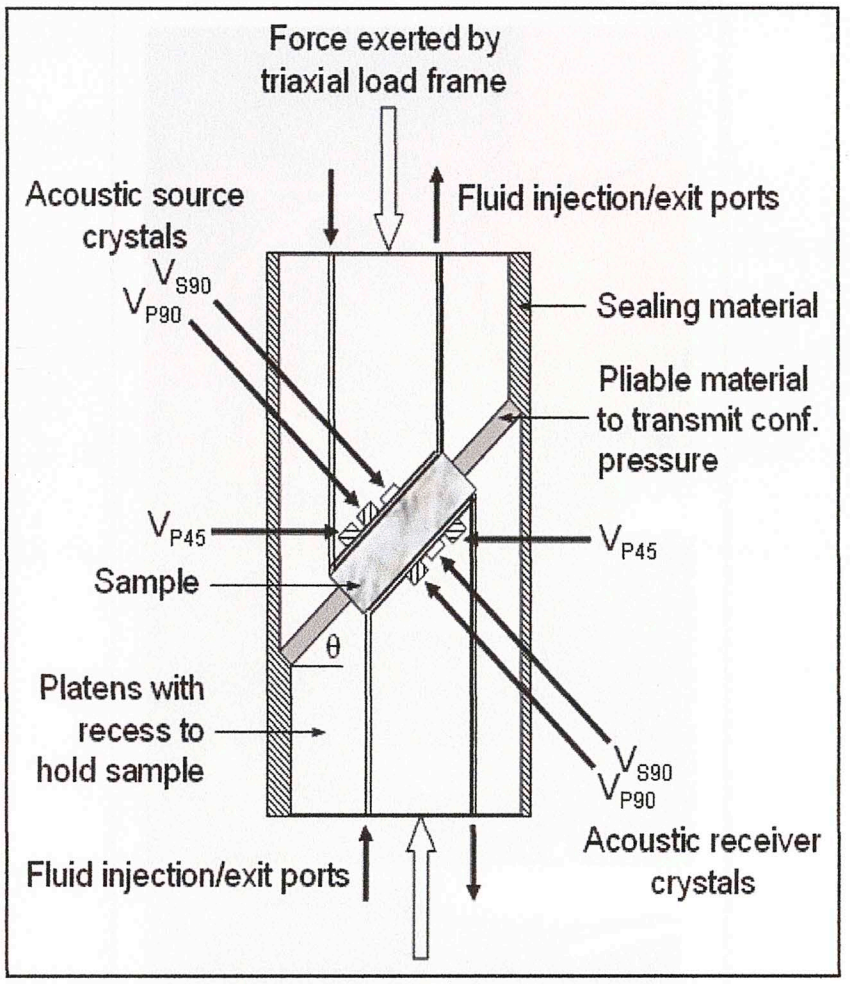

Figure 3.9. Schematic of IDSTD™ setup, θ is the inclination angle between the end platens, for this setup is equal to 45° (Abousleiman et al., 2008).

After measuring UPV in the samples, a plug of 2 cm (0.79 in) diameter was cut perpendicular to the bedding planes, the rest of the sample was used for further testing described in the following sections. Depending on sample thickness, from this plug at least two penny-shaped disks with a thickness of 0.71 cm (0.28 in) were prepared. Figure 3.10 presents an example of the standard sample and the setup for the IDSTD™.

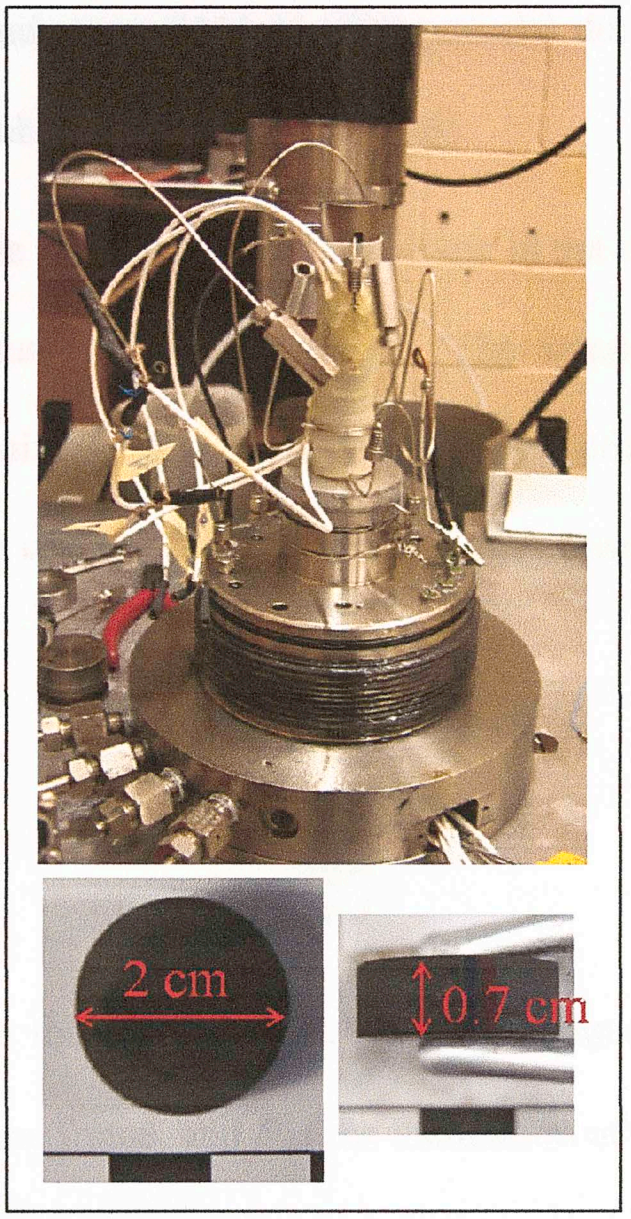

Figure 3.10. IDSTD™ setup, presenting the stack outside the confining cell and the standard disk geometry used for the test.

An MTS 819 loading frame was used to apply load on the stack. The tests were carried out at a constant displacement rate of 0.000254 cm/min (0.0001 in/min). The displacement rate was chosen so the pore pressure build up could be efficiently dissipated and therefore, not have a negative influence on the effective stress acting on the sample (Tran, 2009). The tests were performed in drained conditions by keeping the fluid ports open to atmospheric conditions. Saturation of the samples was guaranteed by flowing PG1 mineral oil through the fluid ports before testing. For applying confining pressure, digitally controlled ISCO syringe pumps were used. Acoustic velocities were measured every 0.7 MPa (100 psi) during the increment of

the confining pressure and every 3115 N (700 pounds) during axial loading, which represents increments of about 13.8 MPa (2000 psi).

The fracture of the sample is then expected to initiate in the critical region, away from the loading edges (Abousleiman et al., 2010). The stress-strain behavior can be evaluated assuming a uniform deviatoric stress in the critical region and using a composite strain from the vertical displacement (Abousleiman et al., 2010):

$$\sigma_{deviatoric} = \frac{4F}{\pi d^2 \cos\theta} \tag{3.23}$$

$$\varepsilon = \frac{u_{vertical}}{d \sin\theta} \tag{3.24}$$

Where F corresponds to the applied load, d is the sample diameter, $u_{vertical}$ is the vertical displacement of the frame, and θ is the inclination of the en-platens (45°).

The Mohr-Coulomb failure criteria assumes a linear dependency of the shear stress (τ) and the normal stress (σ_n) as follows (Fjaer et al., 1992):

$$\tau = C_o + \sigma_n \tan\phi \tag{3.25}$$

Where C_o represents the cohesion defined as the inherent shear strength of the rock and ϕ represents the angle of internal friction, a measure of the ability of a material to resist a shear stress (Fjaer et al., 1992). Two tests were carried out at different confining pressures in order to obtain two points that would describe the Mohr-Coulomb failure criteria. The confining pressures were selected to be 0.69 MPa (1000psi) and 13.8 MPa (2000 psi).

3.4 Fracture Properties

3.4.1 Indirect Brazilian Tensile Strength

The so-called Brazilian test is widely used as a method for the determination of the tensile strength of a rock sample. The test employs a circular disc of material that is compressed by two opposite loads; these are assumed to act over a small arc on the sample periphery, hence, acting as a point load across the sample's diameter (Fairhust, 1964). According to Aydin and Basu (2006), the compression produces a uniform tensile stress (T) distribution perpendicular to the applied load (P) (Figure 3.11).

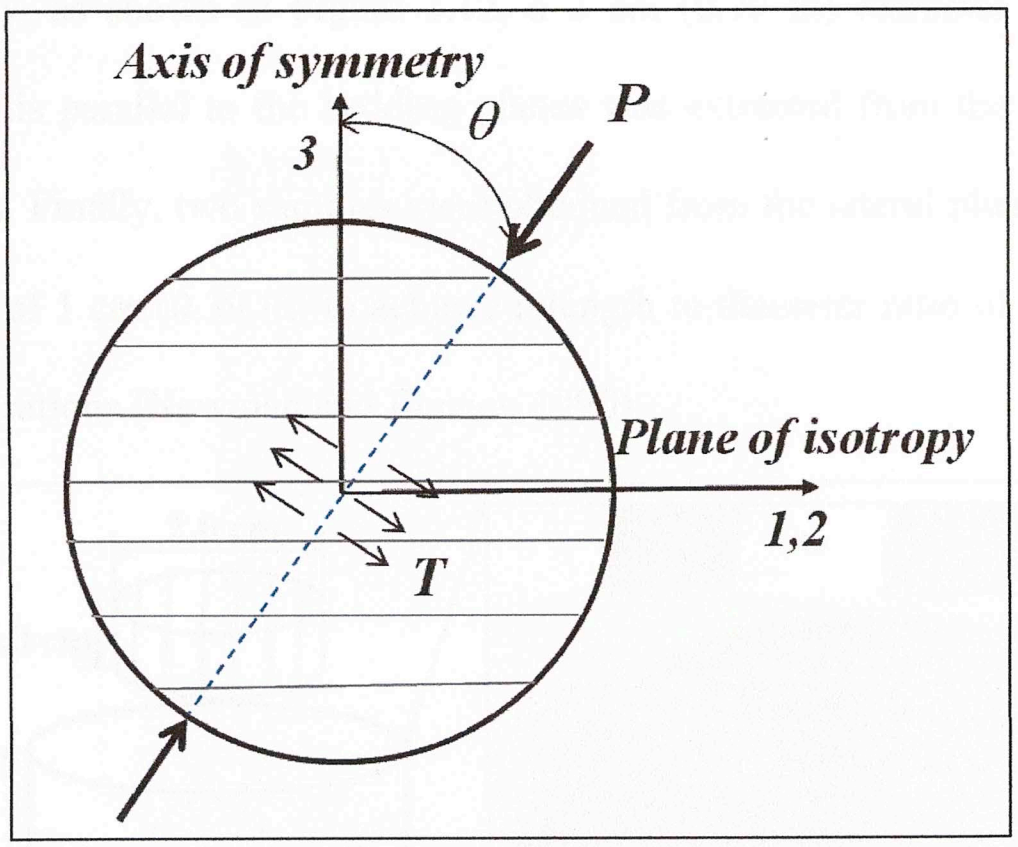

Figure 3.11. Schematic of Brazilian Test for transverse isotropic material, θ represents the angle taken with respect to the axis of symmetry.

An analytical solution by Amadei et al., (1983) for an anisotropic disc under the assumption of plane stress was used to calculate the stress at the disc's center. The equation relating the tensile strength (σ_t), the principal elastic constants, and the applied load at the moment of failure (P) is (Claesson and Bohloli, 2002):

$$\sigma_t = \frac{\sqrt[4]{E_1 / E_3}^{\cos(2\theta)} P}{\pi RL} - \frac{P\cos(4\theta)}{4\pi RL}\left(\frac{\sqrt{E_1 E_3}}{2}\left(\frac{1}{G_3} - \frac{2\nu_3}{E_3}\right) - 1\right) \tag{3.26}$$

Where θ represents the angle of the applied load with respect to the axis of symmetry of the transverse isotropic material and R and L represent the sample radius and thickness respectively.

The samples selected were first tested for UPV and then were sectioned into halves for the Brazilian and CNSCB tests; the latter one will be discussed in the following section. Ideally, as shown in Figure 3.12, a 2 cm (0.79 in) diameter plug with its longitudinal axis parallel to the bedding planes was extracted from the 5.0 cm (2 in) diameter cores. Finally, two samples were obtained from the lateral plug and polished to a thickness of 1 cm (0.39 in) to achieve a length to diameter ratio of 0.5 following ASTM specifications (Newman and Bennet, 1990).

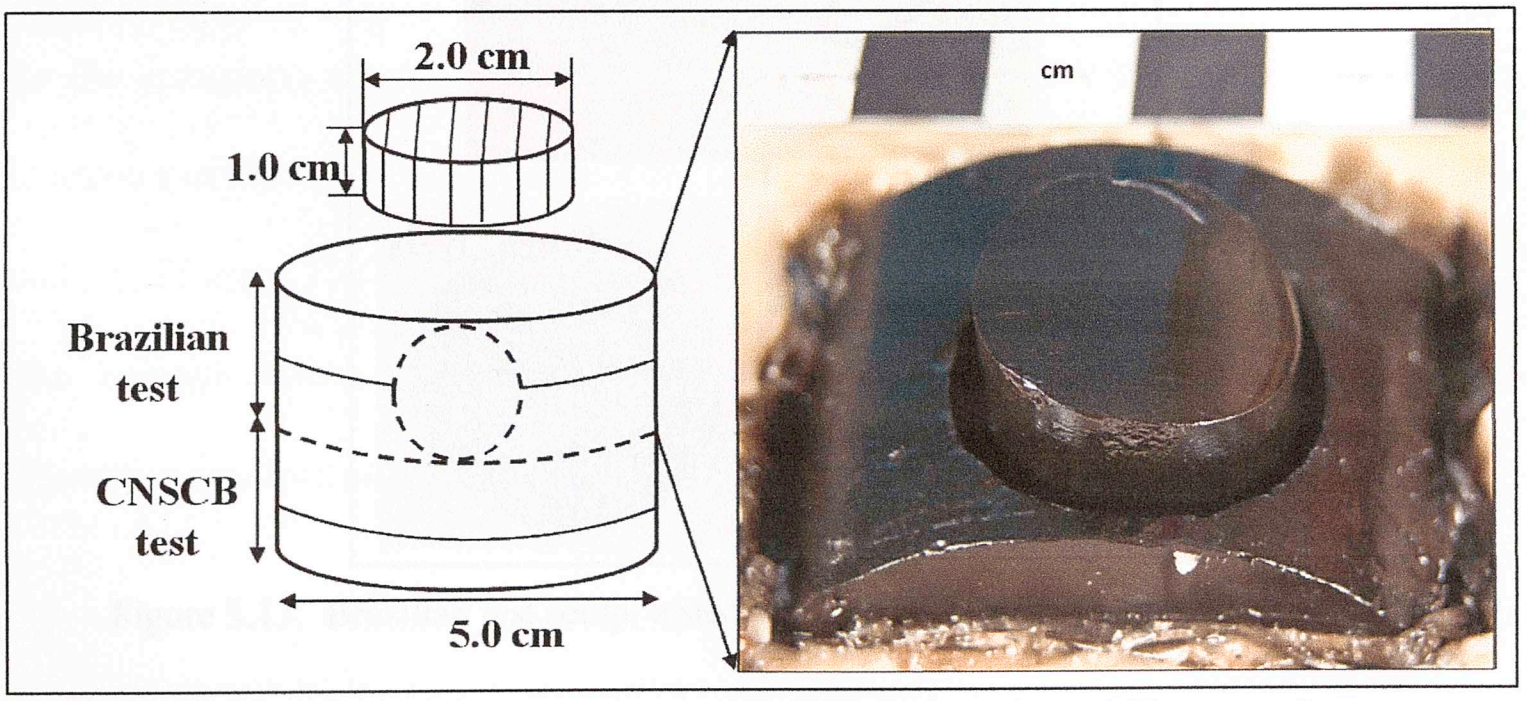

Figure 3.12. Schematic of sample preparation for Brazilian and CNSCB tests, plug cut parallel to the bedding planes.

An Axial-Torsion MTS 319 loading frame was used to compress the samples diametrically. A piece of cardboard was placed between the sample and the machine. For each selected depth, a sample was compressed with the loading line parallel to the bedding planes ($\theta = 90°$), while the other sample was compressed with the loading line perpendicular to the bedding planes ($\theta = 0°$). The loading rate was set at 8.9 N/s (2 lb/s), so the total testing time for each sample was less than 1 minute following ASTM standards (Newman and Bennet, 1990).

Figure 3.13 presents the two sets of tested samples for a given depth; the angle at which the line load was applied is shown.

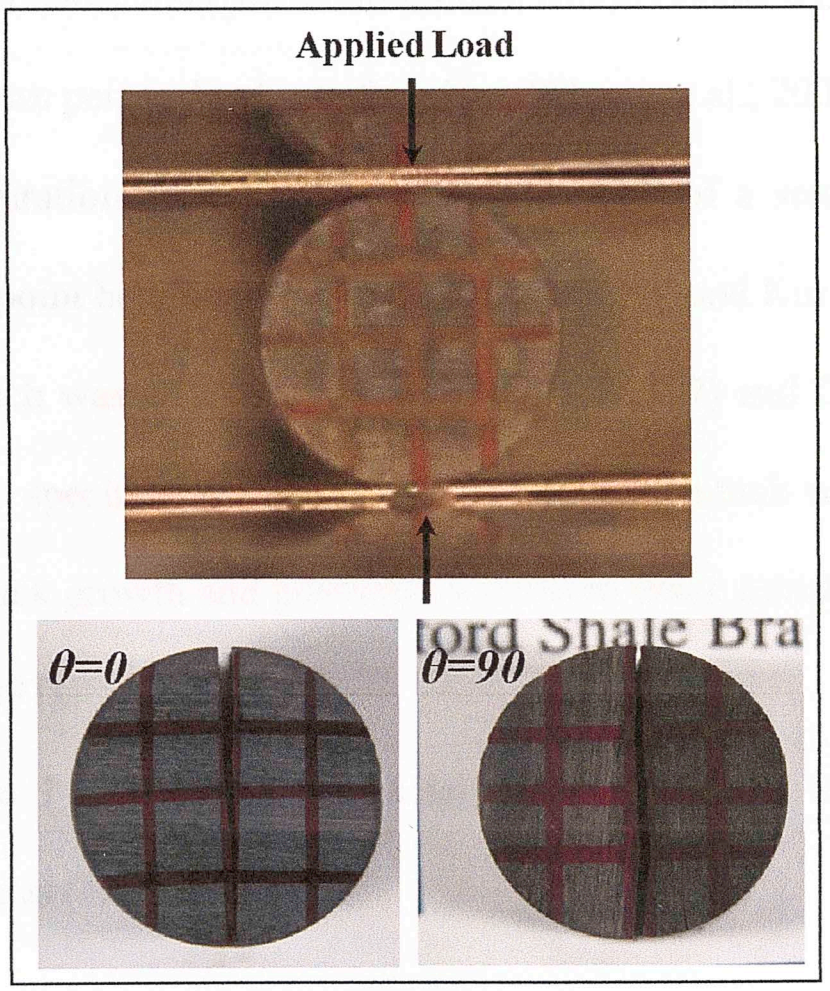

Figure 3.13. Brazilian test setup, tested samples at different loading orientations.

3.4.2 Fracture Toughness using semi-circular type specimens under three-point bending (CNSCB) and Acoustic Emissions.

The field of fracture mechanics has been developed for geomaterials with the purpose of studying the crack propagation and fracture of rocks under certain stress conditions. It has been applied to fields such as hydraulic fracturing, mechanical fragmentation, geophysics, fluid transport properties of fracturing rock masses, earthquake mechanics and many other practical applications (Lim et al., 1993). The fundamental property of fracture mechanics is the fracture toughness, which describes the resistance of the material to the propagation of a preexisting crack (Wang, 1998). The crack propagation is given under three different modes: Mode I is the tensile opening mode, where the crack grows perpendicular to the plane (Chang et al., 2002).

The sample configuration used for this study consisted of a semicircular specimen (SCB) under three-point bending, first proposed by Chong and Kuruppu (1984), with a chevron notch, which was then adapted by Kuruppu (1997) and Chang et al., (2001) for the semicircular specimen (Figure 3.14). The chevron notch was chosen as it can produce a stable crack growth and guarantee a uniform crack initiation at the tip of the notch (Kuruppu, 1997).

The average Mode I stress intensity factor along the crack front is given in a dimensionless form as (Kuruppu, 1997):

$$K_I = \frac{K_{av} P}{t\sqrt{R}} \tag{3.27}$$

Where t is the sample thickness, K_{av} the normalized stress intensity factor, and P is the maximum load applied. According to Kuruppu (1997) K_{av} shows a minimum value

at about a/R = 0.35 of 7.3, where a represents the crack length, and R represents the sample radius. The experimental maximum load and the K_{av} critical value are used to determine the fracture toughness.

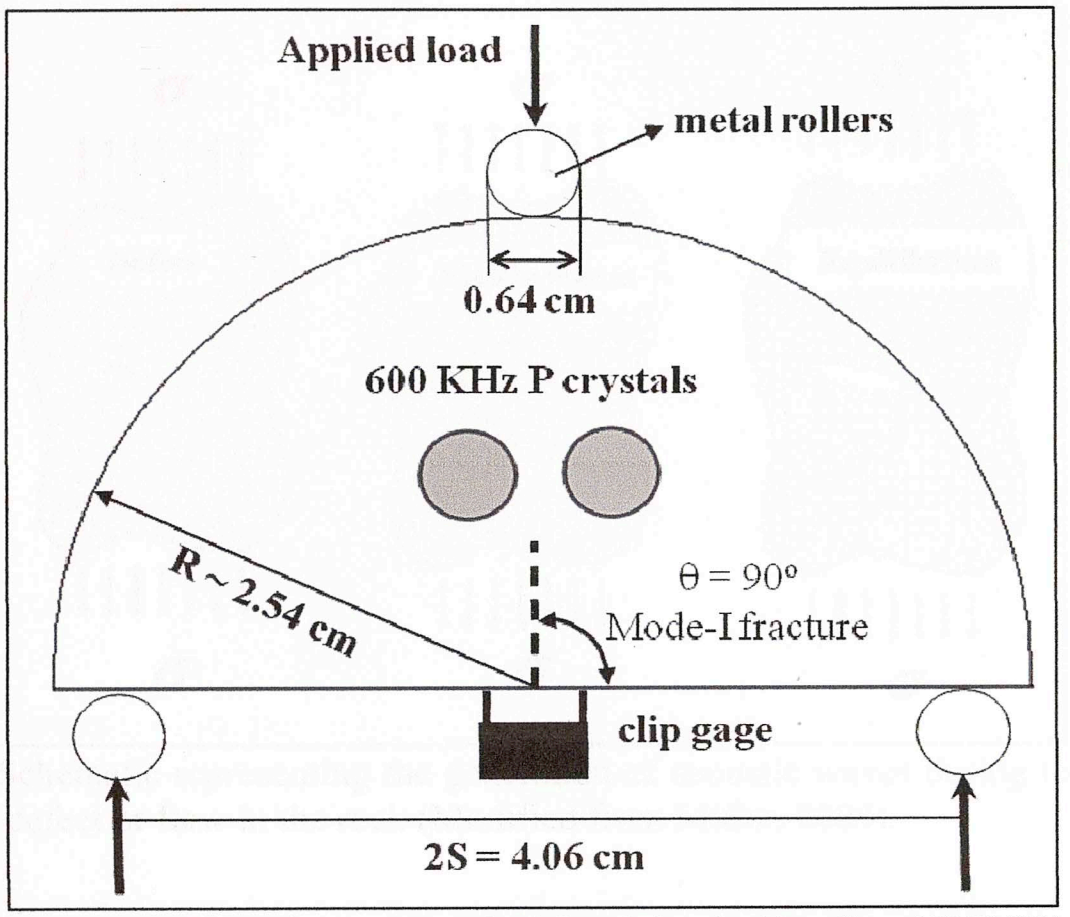

Figure 3.14. Schematic of the Chevron Notched Semicircular Bending (CNSCB) test setup.

Acoustic Emission (AE) monitoring has been proven to be a powerful tool in investigating crack propagation and failure in rock materials. Its applications have been studied by a number of authors (Mansour, 1994; Lysak, 1996; Dai and Labuz, 1997; Backer et al., 2005; Yuyama, 2005). An Acoustic Emission (AE) is defined as the phenomenon in which elastic waves are emitted from a sudden release of strain energy during the initiation and/or extension of inherent flaws present in the rock. Figure 3.15 presents a schematic illustrating such phenomena, starting with a flaw or defect in the rock mass, when a tensile stress (σ) is applied, the defect is stressed and opens and even propagates. There is a release of energy from localized sources due to an abrupt redistribution of the stress field around the opened crack (Backer et al.,

2005). This energy is released as an elastic wave that propagates through the media until equilibrium is reached, from which point an energy buildup starts again with the increasing stress (Figure 3.16).

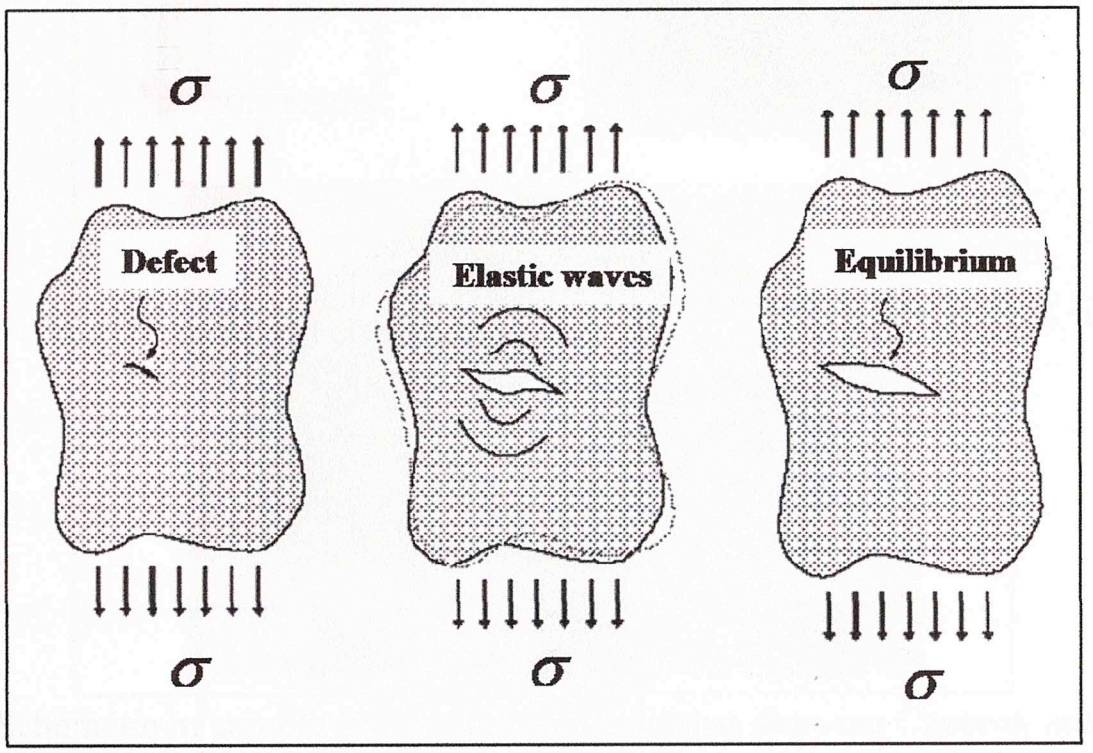

Figure 3.15. Schematic representing the generation of acoustic waves during tensile opening of an inherent defect or flaw in the rock (Modified from Miller, 2004).

This study was carried out generating only Mode I crack propagation; therefore the angle of the notch (ε) was set at 90 degrees (Lim et al. 1994). The characteristics of the samples and the setup are shown in Figure 3.16. The 5 cm (2 in) diameter core was cut in half, selecting the smoothest surface for this test in cases where the core was not totally cylindrical. The other half was used for samples for the Brazilian and/or IDSTD^{TM} tests in cases where needed. Following Chang et al. (2002), the loading span (*2S*) was fixed at 4.06cm (1.6 in), which resulted in a span to diameter ratio (*S/D*) of 0.8 (Figure 3.14). The notch was formed by two cuts using a Dia-Laser saw with a thickness of 0.03 cm (0.01 in), an outer diameter of 10.2 cm (4 in), and an inner diameter of 1.3 cm (0.51 in). The initial crack length (a_0) was designed to be approximately 0.6 cm (0.24 in) (Figure 3.19).

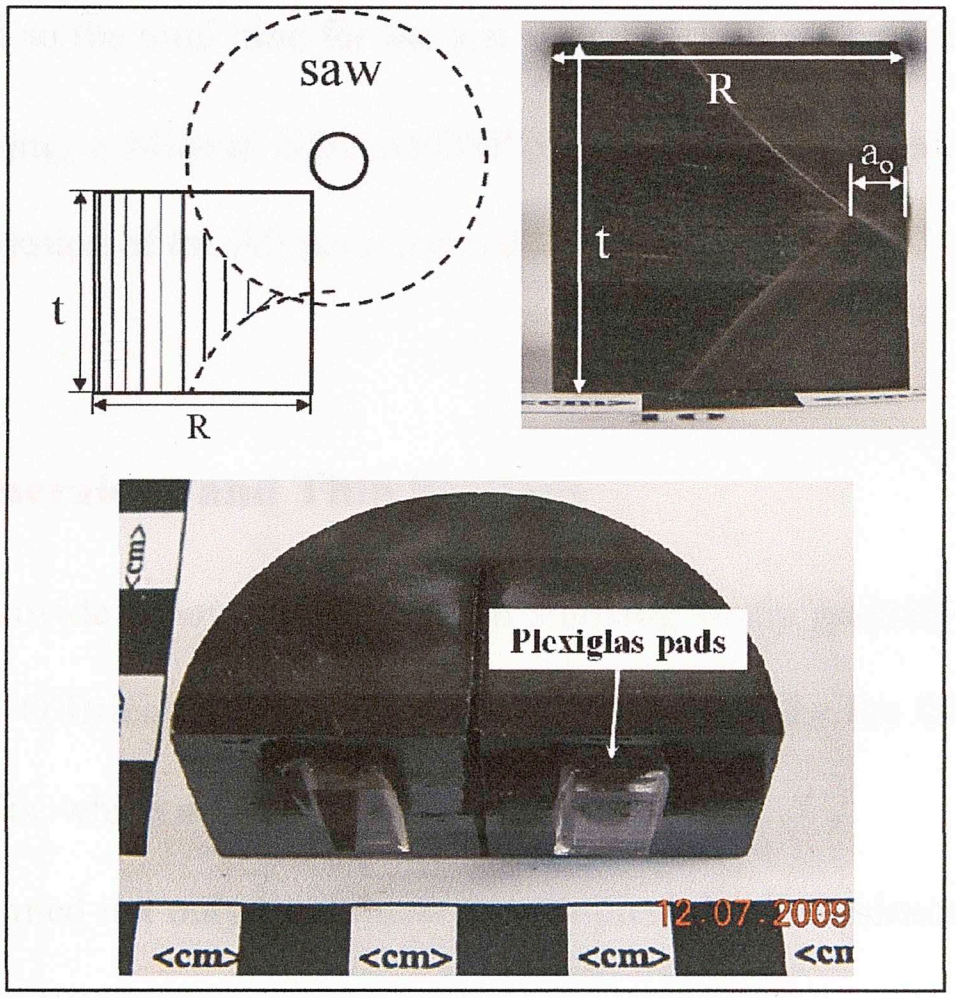

Figure 3.16. Schematic of sample preparation, cross section showing Chevron notch geometry, prepared sample with Plexiglas pads attached to the base.

During the test, the opening of the crack was recorded using an MTS clip gage mounted on Plexiglas pads fabricated specially for such application. The pads were glued on the base of the sample (Figure 3.16). Two pairs of 600 kHz compression piezoelectric crystals were clamped on each side of the notch and approximately in front of the notch tip where the fracture propagation is assumed to begin. Thin lead foils were placed between the crystal and the rock to serve as acoustic coupling and ground for the recording system. The crystals served as receivers to monitor the acoustic emissions from the fracturing process

Axial load was applied to the CNSCB samples by an Axial-Torsion MTS 319 loading frame. The tests were carried out under controlled displacement to provide a better control of the stable fracture growth. Displacement rate was at be 0.00005 cm/sec

(0.00002 in/sec) so the total time for the test is within 5 min (Chang et al. 2002). For the AE monitoring, a Mistras 2001 AEDSP-32/16 system was used, which allowed real time visualization of the AE parameters during the test.

3.5. XRD Mineralogy and Thin Sections

Thin sections provide a powerful tool when studying finely grained materials under the microscope. O'Brien and Slatt (1990) provide a guide for the fabric analyses of argillaceous rocks, which was followed in this thesis.

XRD was performed not only to evaluate the samples' detailed mineralogy but also to correlate with the ECS log and previous mineralogy results.

The samples for thin section preparation and XRD analysis were cut from one half of the tested CNSCB samples, as illustrated in Figure 3.17. A vertical section was selected for the thin section preparation. A vertical fragment of the entire remaining rock was cut for XRD analysis after the thin section was prepared. The samples for thin sections were shipped to National Petrographic Services, Inc for the preparation of the thin sections. From the remains of the preparation of the thin sections, the XRD samples were shipped to the USGS for analysis.

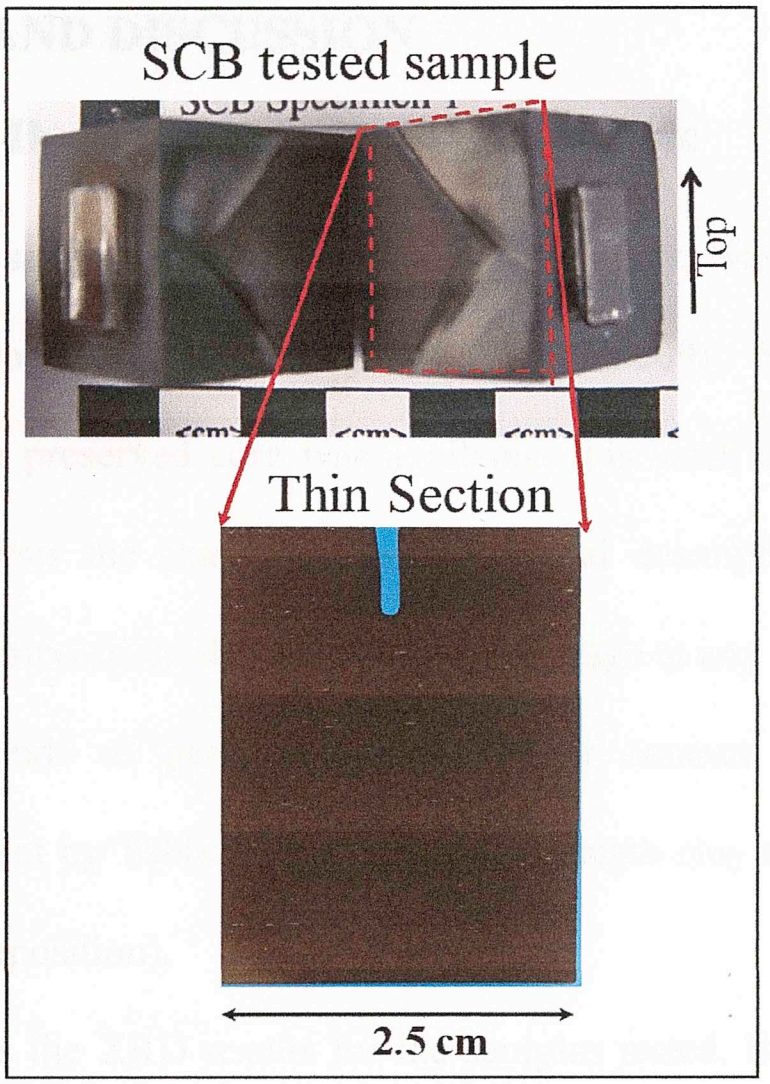

Figure 3.17. Tested SCB sample for thin section preparation, and prepared thin section.

4. RESULTS AND DISCUSSION

4.1 Geological Description, Microscopic Fabric

Woodford shale sample selection tested in this work was guided by the earlier geomechanics work characterization of Tran (2009). Since limited previous description of the preserved core was available, this work detailed through focused thin section analysis the shale detailed geological description. Given the variable nature of shale composition, the properties can change at any scale (Slatt et al., 2008), following the trends of percentage of the clay content and the other mineral composition evident by Table 4.1 (at any chosen depth clay content varied so did the other mineral composition).

Table 4.1 presents the XRD results for the samples tested. Estimated porosities from logs and XRD mineralogy of the selected samples are also given. The porosity log accounts for the total effective porosity obtained from the Wyche #1 well which was calibrated using mercury injection porosity measurements on the core by Tran (2009). From these, clay packing density was calculated following Equations 3.15 - 3.17.

Table 4.1. USGS XRD Mineralogy results.

Depth (m)	Qtz	Kspar	Plag	Total Carb	Pyr	SUM NON-CLAY	SUM CLAY	Amorphous	Por. (%)	CPD (η)
33.81	52	3	0	4	1	59	23	18	0.16	0.72
36.85	53	3	0	5	3	65	12	21	0.16	0.71
41.36	36	2	2	11	3	53	32	15	0.14	0.78
44.28	32	2	2	7	3	47	38	15	0.16	0.76
50.04	38	3	2	7	6	56	27	17	0.15	0.76
50.17	36	2	2	9	3	54	26	20	0.15	0.76
50.59	35	1	2	2	10	50	29	20	0.14	0.78

The results show the expected differences in mineralogy between the Upper and Middle/Lower member of the Woodford observed in the ECS log, Showing high quartz content and low clay content for the Upper Woodford

Thin section observations, as shown in Figures 4.1-4.5, have resulted in the following lithofacies classifications for the selected samples, following the methodology of O'Brien & Slatt (1990), and based on Buckner's (2011) lithofacies description: light gray laminated shale (33.81 m), calcareous laminated shale (36.86 m), gray laminated shale (41.36 m, 44.28 m and 50.18 m), and black laminated shale (50.59 m) are the dominant lithofacies.

The sample at 33.81 m (light gray laminated shale) corresponds to a siliceous/argillaceous mudstone (Figure 4.1). The microfabric presents massive to poorly developed laminations. Detrital silt size quartz grains are present both scattered in the matrix and as thin laminations. Microcrystalline silica (chert) is present in elongated, lenses of a few mm thick. These might correspond to replaced macerals of organic matter (possibly liptinite), or might also correspond to compacted radiolarian tests replaced with microcrystalline silica. Liptinite (yellow in transmitted light) is present but not abundant in the same lenses, possibly from compacted algal bodies (Buckner, 2011). Some scattered clay size pyrite crystals occurred. Horizontally laminated organics (dark) are present (Figure 4.1).

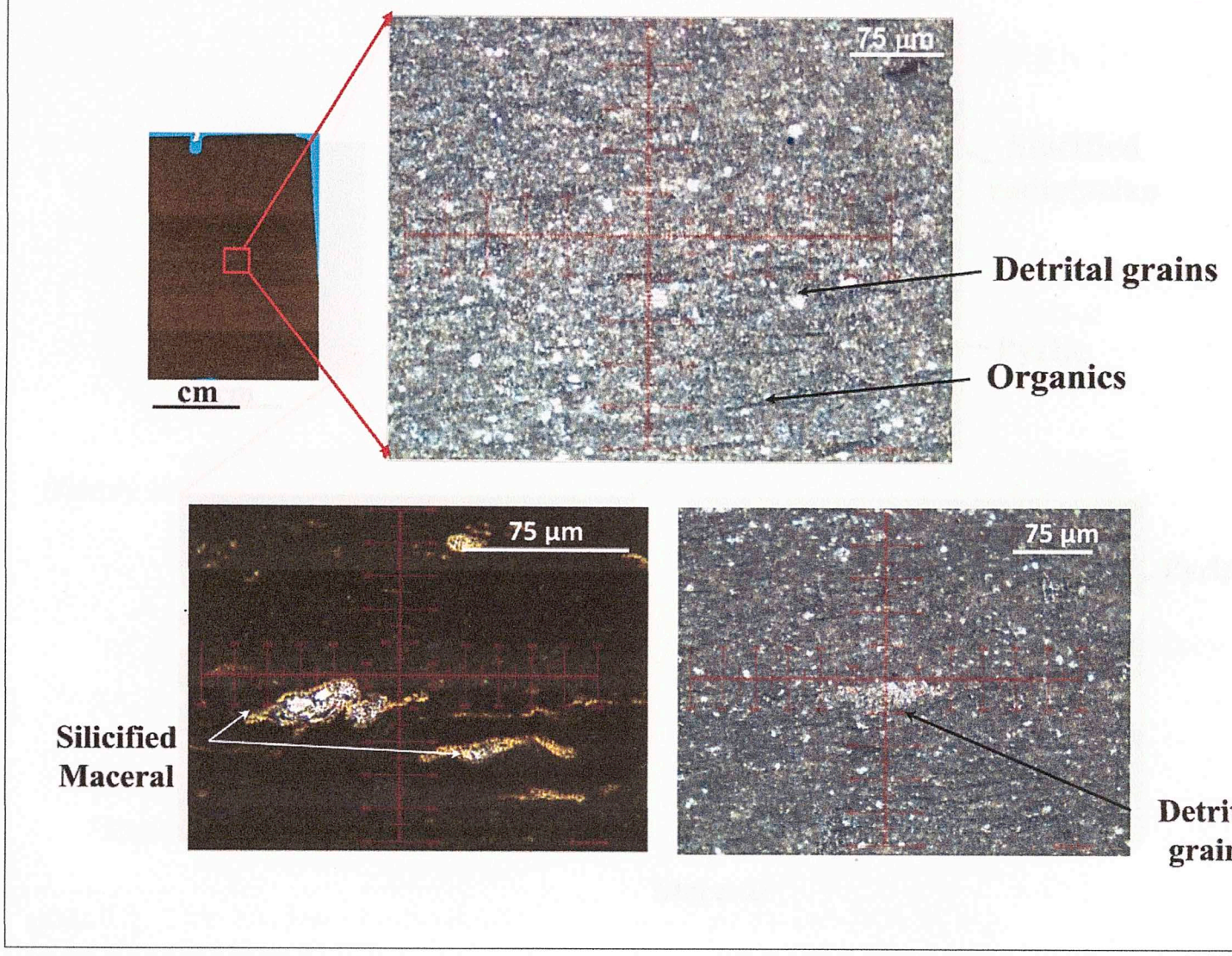

Figure 4.1. Thin section observations for light gray laminated shale (33.81 m).

The sample at 36.86 m (calcareous laminated shale) corresponds to a siliceous/argillaceous mudstone. The microfabric is thickly laminated, presenting alternating, siliceous-rich laminations (of less than 0.5 mm) and clay/organic rich laminations. The laminations are composed of silt sized silicified radiolarian microfossils (Figure 4.2). Calcite is present in the laminations (they react in contact with HCL), however the source of the calcite is still not clear (*Totten, personal communication*). Authigenic crystalline pyrite (light gold in reflected light) is present within the siliceous radiolarians. Yellow macerals (possibly liptinite) are present within the clay rich laminations, but not so abundant in the siliceous- rich laminations (Figure 4.2).

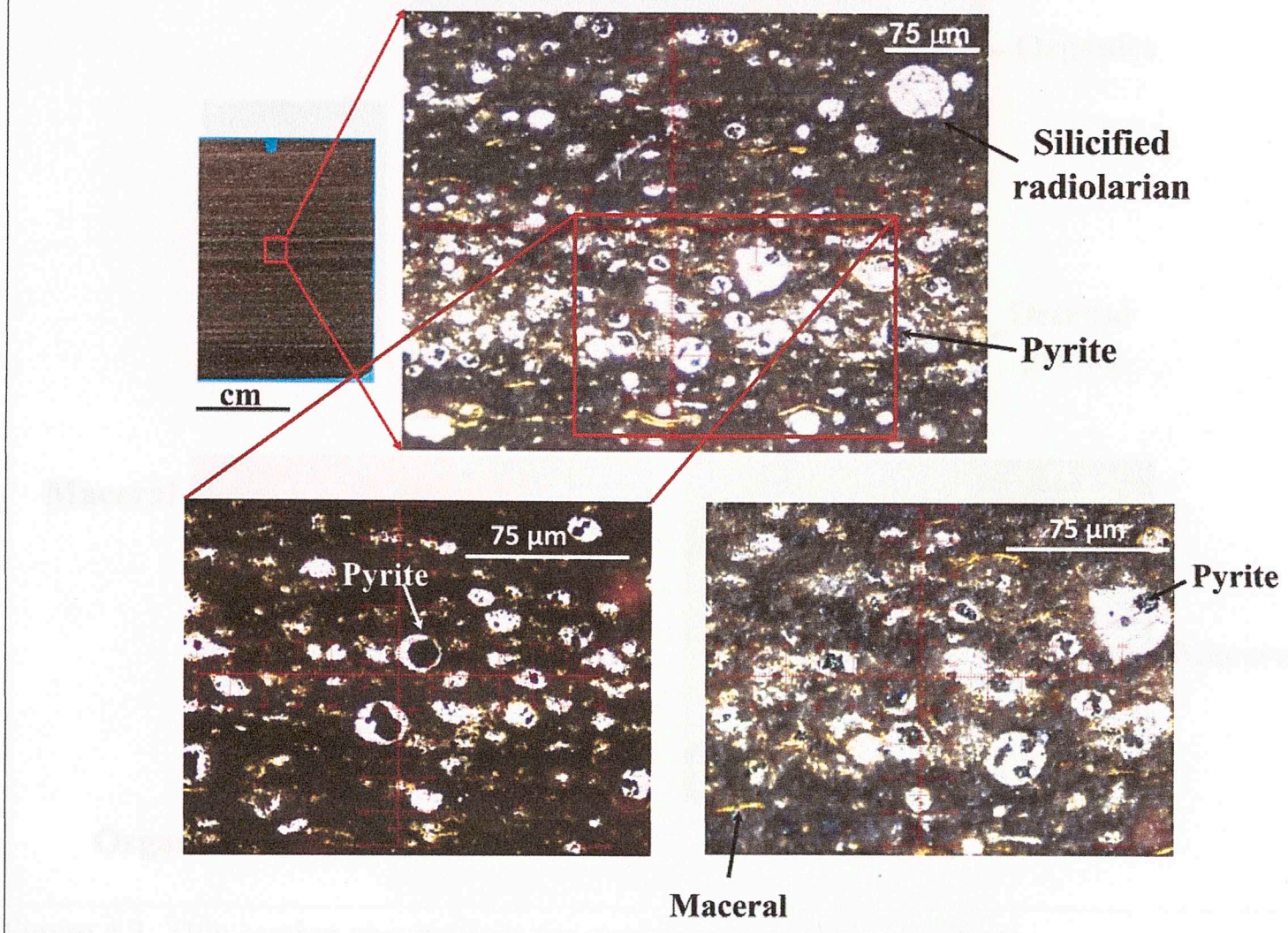

Figure 4.2. Thin section observations for calcareous laminated shale (36.86 m).

Samples at 41.36 m, 44.28 m and 50.18 m (gray laminated shale) are argillaceous/siliceous mudstone (Figures 4.3 - 4.5). The microfabric is finely laminated showing some small laminations of relatively lighter color, possibly due to a relative increase in the amount of the clay size detrital grains. Several thin laminations (at the micro-scale) are present, composed mainly of clay size detrital grains (Quartz and/or Plagioclase). Yellow macerals (liptinite) are common, but chert-replaced macerals are not common. Black organic deposits are present and pyrite is scattered in small proportions in the matrix (Figure 4.3 – 4.4).

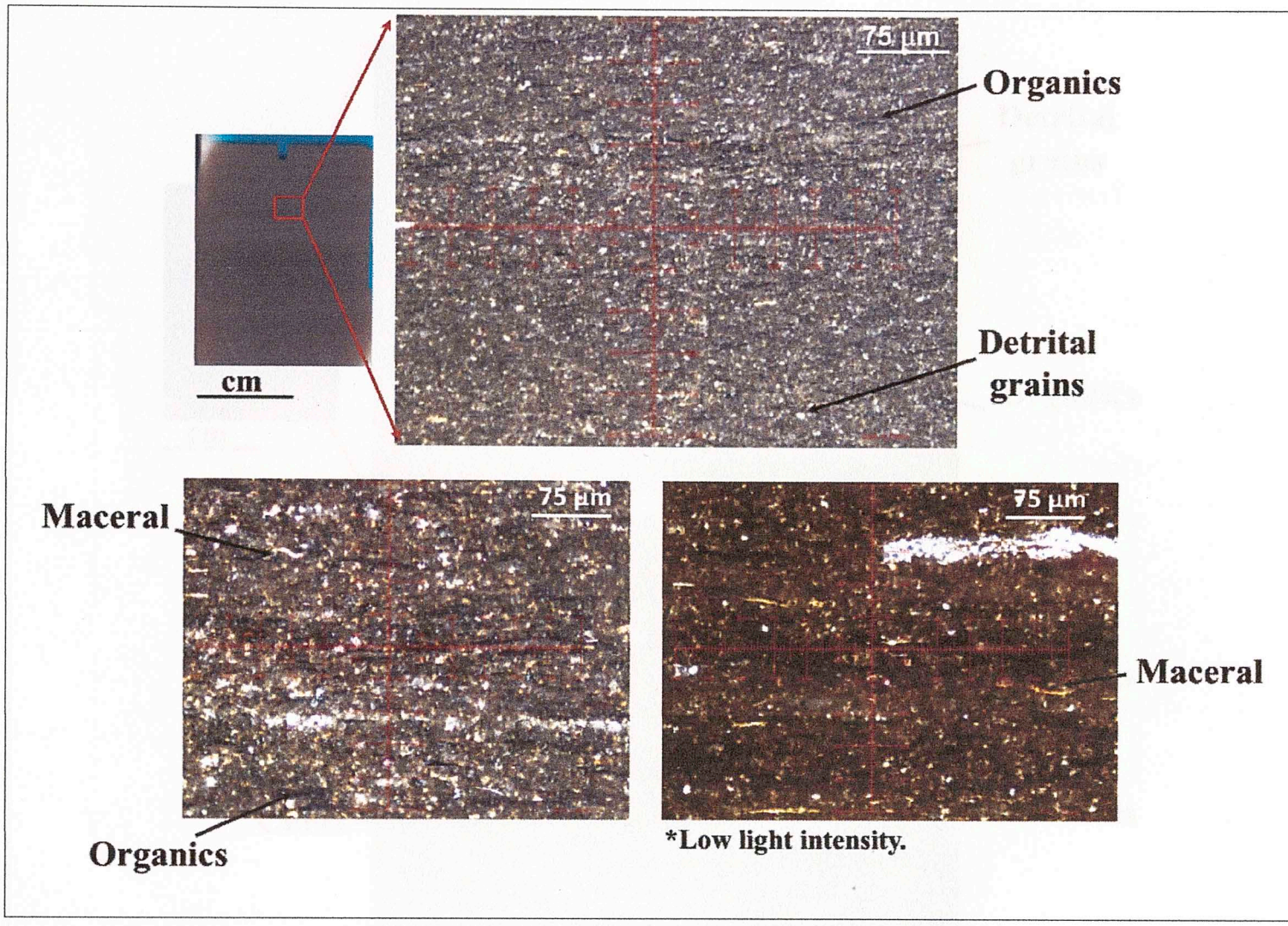

Figure 4.3. Thin section observations for gray laminated shale (41.36 m).

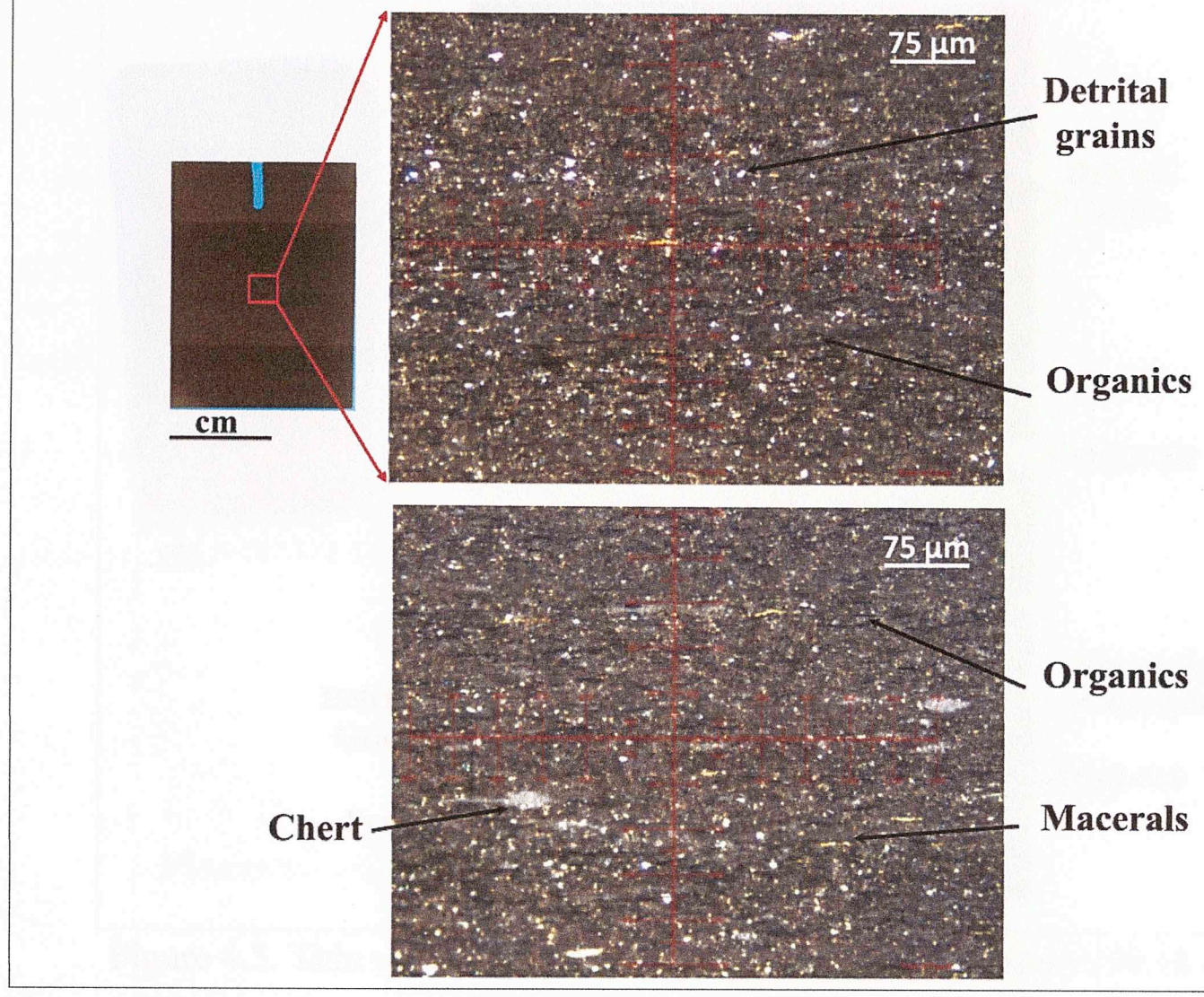

Figure 4.4. Thin section observations for Gray laminated shale (44.28 m).

A bigger thin section was prepared from the tested UCS sample. This thin section was microprobe-polished. Figure 4.5 presents a boundary between two laminations of distinctive amount of detrital grains as a dotted line. Several thin laminations (micro-scale) are present, showing good lateral continuity in the thin section. These are composed of clay size detrital grains (Quartz/Plagioclase). Yellow macerals (liptinite) are common (Figure 4.5).

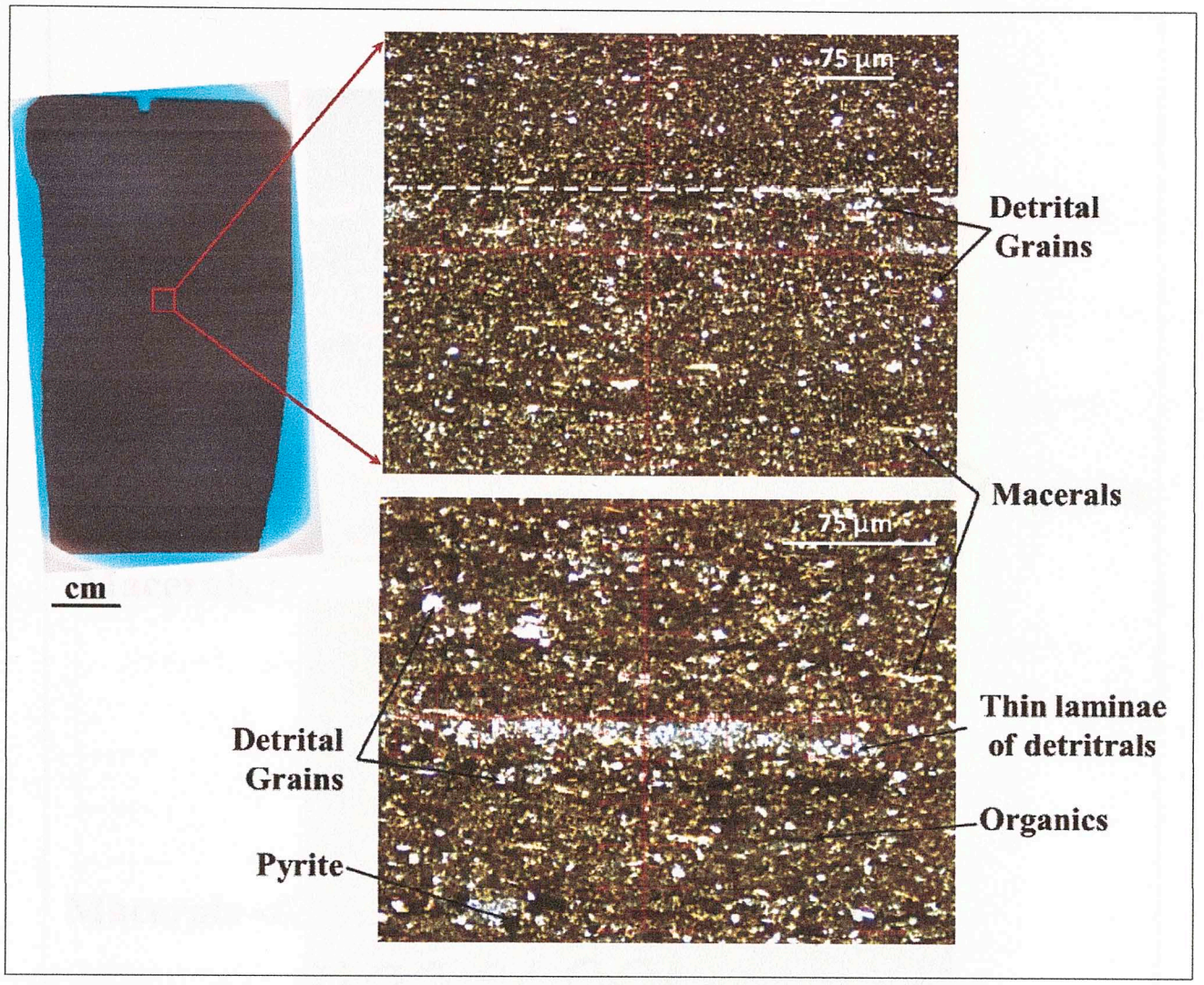

Figure 4.5. Thin section observations for Gray laminated shale (50.18 m).

The sample at 50.59 m (black laminated shale) corresponds to an argillaceous mudstone (Figure 4.6). Microfabric is slightly finely laminated; yellow macerals (liptinite) are abundant, presenting different sizes, shapes and colorations. Detrital clay size grains are present, but less abundant, resulting in a more clay-rich matrix. Organic black laminations are present. There is a relative upward decrease in the amount of macerals (Figure 4.6).

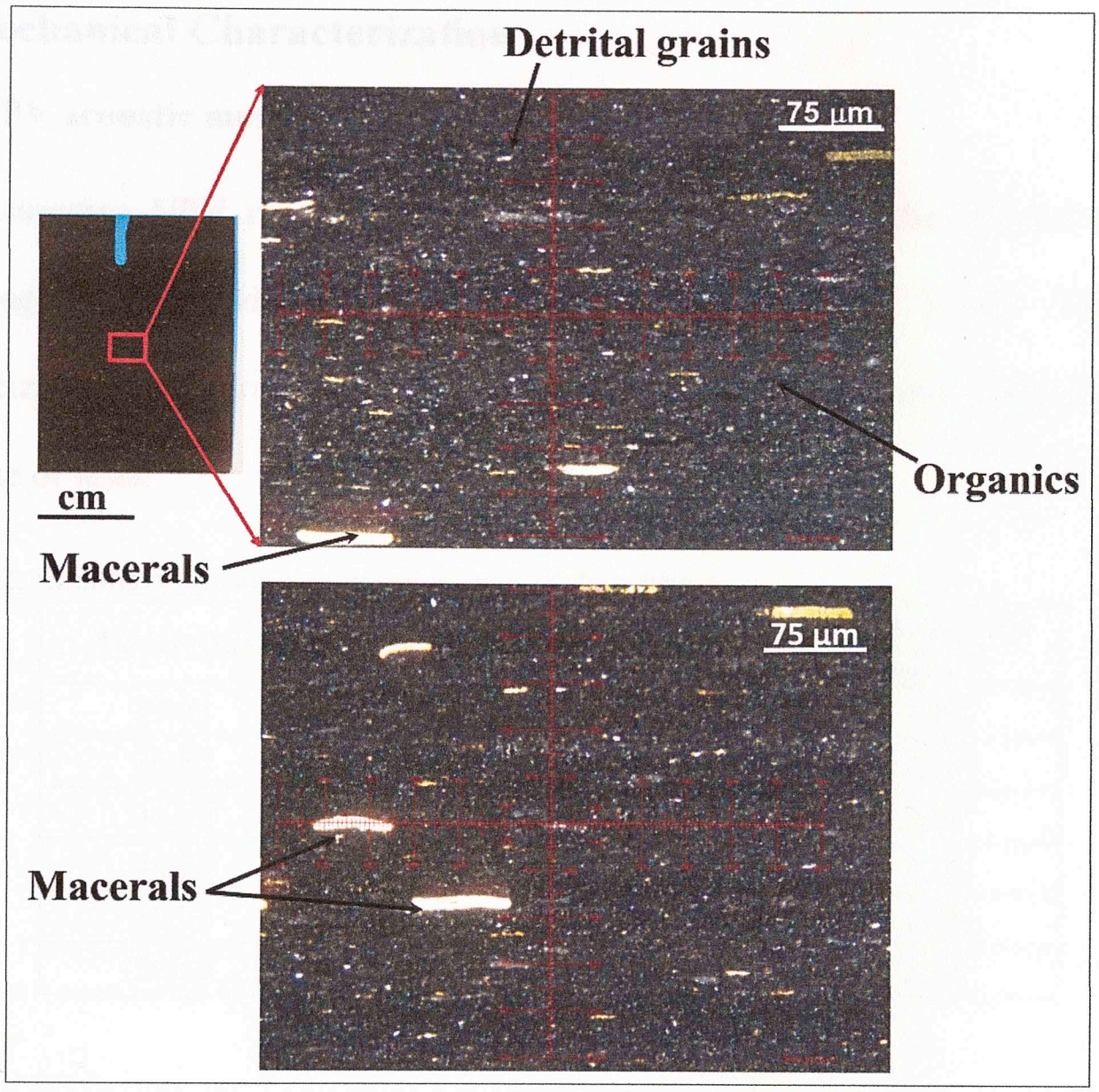

Figure 4.6. Thin section observations for Gray laminated shale (50.59 m).

The thin section of the calcareous laminated shale sample shows that the observable macroscopic laminations are the result of interlayers between continuous clay rich and siliceous laminations. On the other hand, thin sections of other samples reveal that the silt-size quartz grains, pyrite, kerogen, and the rest of the non-clay components are embedded in the continuous clay matrix (GG). The relative difference in abundance of such components at the micro-scale in the clay matrix results in the finely laminated fabric characteristic of the light gray laminated shale and gray/black laminated shale. These observations highlight the need for a specific evaluation of the thickly laminated sample when studying the effects of Woodford Shale morphology on its anisotropic mechanical properties, as presented in subsequent sections.

4.2 Mechanical Characterization

4.2.1 UPV acoustic measurements

Non-destructive UPV measurements were first conducted for the selected samples following the methodology previously described (Chapter 3.3.2). Table 4.2 summarizes the measured dimensions and bulk densities of the core samples used for this suite of tests.

Table 4.2. Summary of samples dimensions and densities

Depth (m)	Length (cm)	Diameter (cm)	Bulk density (g/cc)
33.81	4.47	5.02	2.09
36.85	4.27	5.01	2.13
41.36	6.34	4.98	2.27
44.28	2.39	5	2.26
50.27	2.72	4.98	2.25
50.59	2.74	5.04	2.18

Figure 4.7 presents the common waveforms acquired for this test, from which the arrival times were taken for the several waves employed, the red dotted lines represent the approximate arrival time for each waveform. Based on the sample dimensions, the velocities were then calculated for the aforementioned arrival times.

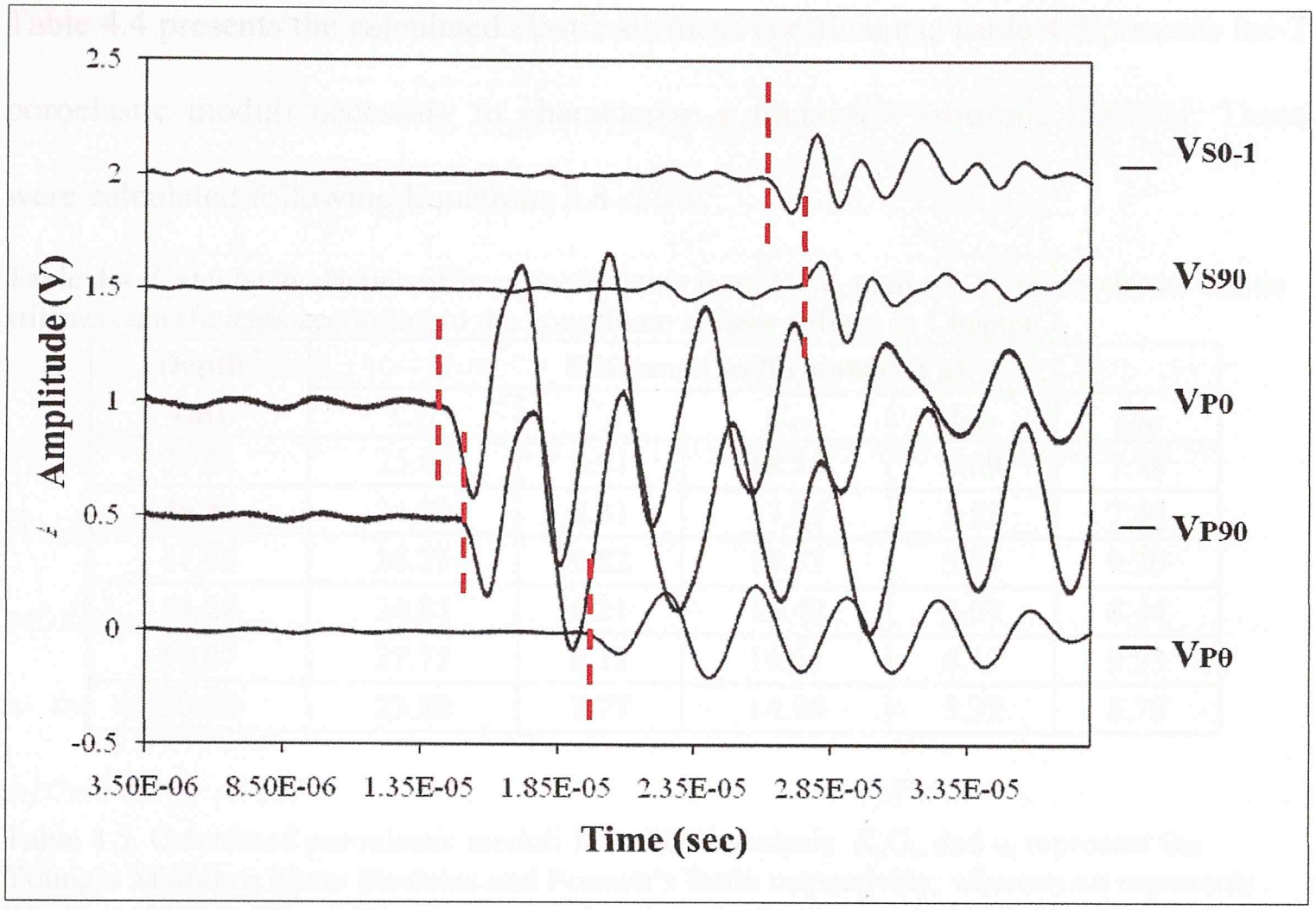

Figure 4.7. Standard waveforms acquired during UPV testing. Each waveform is related to the calculated velocity following the nomenclature introduced in Chapter 3.3.2.

Table 4.3 presents the calculated velocities for the selected samples. The angle (θ) used for the measurement and therefore for the calculation of $V_{P\theta}$ is shown in degrees. The elastic stiffness coefficients were calculated following Equations 3.2 - 3.7.

Table 4.3. Calculated velocities from UPV analysis. V_{P0}, V_{P90}, and $V_{P\theta}$ represent compression velocities at *0, 90* and an angle θ with respect to the vertical axis respectively. $V_{S0\text{-}1}$ *and* $V_{S0\text{-}2}$ represent perpendicularly polarized shear velocities in the vertical direction, whereas V_{S90} represents the shear velocity in the horizontal axis.

Depth	**Velocities (m/sec)**						
(m)	V_{P0}	V_{P90}	$V_{S0\text{-}1}$	$V_{S0\text{-}2}$	V_{S90}	$V_{P\theta}$	θ (°)
33.81	3460	2980	1929	1656	1650	3076	41
36.85	3363	2902	1870	1648	1610	3050	40
41.36	3530	2860	2024	1565	1562	2944	25
44.28	3313	2532	1932	1498	1492	3028	52
50.27	3512	2739	2013	1640	1690	2966	31
50.59	3301	2615	2007	1562	1571	2970	45

Table 4.4 presents the calculated elastic stiffness coefficients; Table 4.5 presents the 7 poroelastic moduli necessary to characterize a transverse isotropic material. These were calculated following Equations 3.8 -3.14.

Table 4.4. Calculated elastic stiffness coefficients from UPV analysis. C_{ij} represent the elastic stiffness coefficients according to the coordinate system defines in Chapter 3.

Depth (m)	**Stiffness Coefficients (GPa)**				
	C_{11}	C_{13}	C_{33}	C_{44}	C_{66}
33.81	25.02	6.91	18.56	5.69	7.78
36.85	24.09	8.31	17.94	5.52	7.45
41.36	28.29	9.82	18.57	5.54	9.30
44.28	24.81	8.21	14.49	5.03	8.44
50.27	27.75	8.12	16.61	6.13	9.23
50.59	23.80	7.77	14.90	5.32	8.78

Table 4.5. Calculated poroelastic moduli from UPV analysis. E_i,G_i, and υ_i represent the Young's Modulus, Shear Modulus and Poisson's Ratio respectively, whereas *αii* represents Biot's coefficient. The suffixes correspond to the coordinate system defined in Chapter 3.

Depth (m)	**Poroelastic Moduli (GPa)**						
	E1	*E3*	*v3*	*G1*	*G3*	*α11*	*α33*
33.81	20.33	15.79	0.20	7.78	5.69	0.67	0.74
36.85	18.83	13.79	0.25	7.45	5.52	0.67	0.73
41.36	22.22	13.49	0.26	9.30	5.54	0.62	0.70
44.28	19.62	10.37	0.25	8.44	5.03	0.67	0.75
50.27	21.80	12.03	0.25	9.23	6.13	0.63	0.72
50.59	19.51	10.87	0.26	8.78	5.32	0.70	0.76

The suffixes make reference to Figure 3.1.

The sample at 50.27 m (164.94 ft) was used for the analysis of the group vs. phase velocity measurement previously mentioned in Chapter 3. Table 4.6 presents the dimensions, density, the measured P wave velocities, and the calculated phase velocities of the two plugs taken at angles (θ) of 30° and 60° (Figure 3.8). Such measurements are consistent with the previously mentioned classic UPV approach, therefore, they represent phase velocities.

Table 4.6. Plug dimensions, densities and velocities from UPV analysis for sample at 50.27 m (164.94 ft).

Plug	L (cm)	D (cm)	Density (g/cc)	Measured Vel. (m/sec)	Calculated Vel. (m/sec)
30°	2.7	2	2.24	3016	2945
60°	2.2	2	2.24	3362	3336

Assuming that phase velocities are measured with the methodology here proposed, phase velocity surfaces were calculated based on the elastic stiffness coefficients (Table 4.4) following Equations 3.18 - 3.22. Figure 4.8 presents the calculated phase velocities and the measured phase velocities for the plugs at 30° and 60° with respect to the axis of symmetry. The results were then compared in order to validate the methodology employed. The results present errors of 2.4% and 0.8% for the plugs at 30° and 60° respectively. This confirms that by following the methodology here used, phase velocities are measured in the UPV analysis.

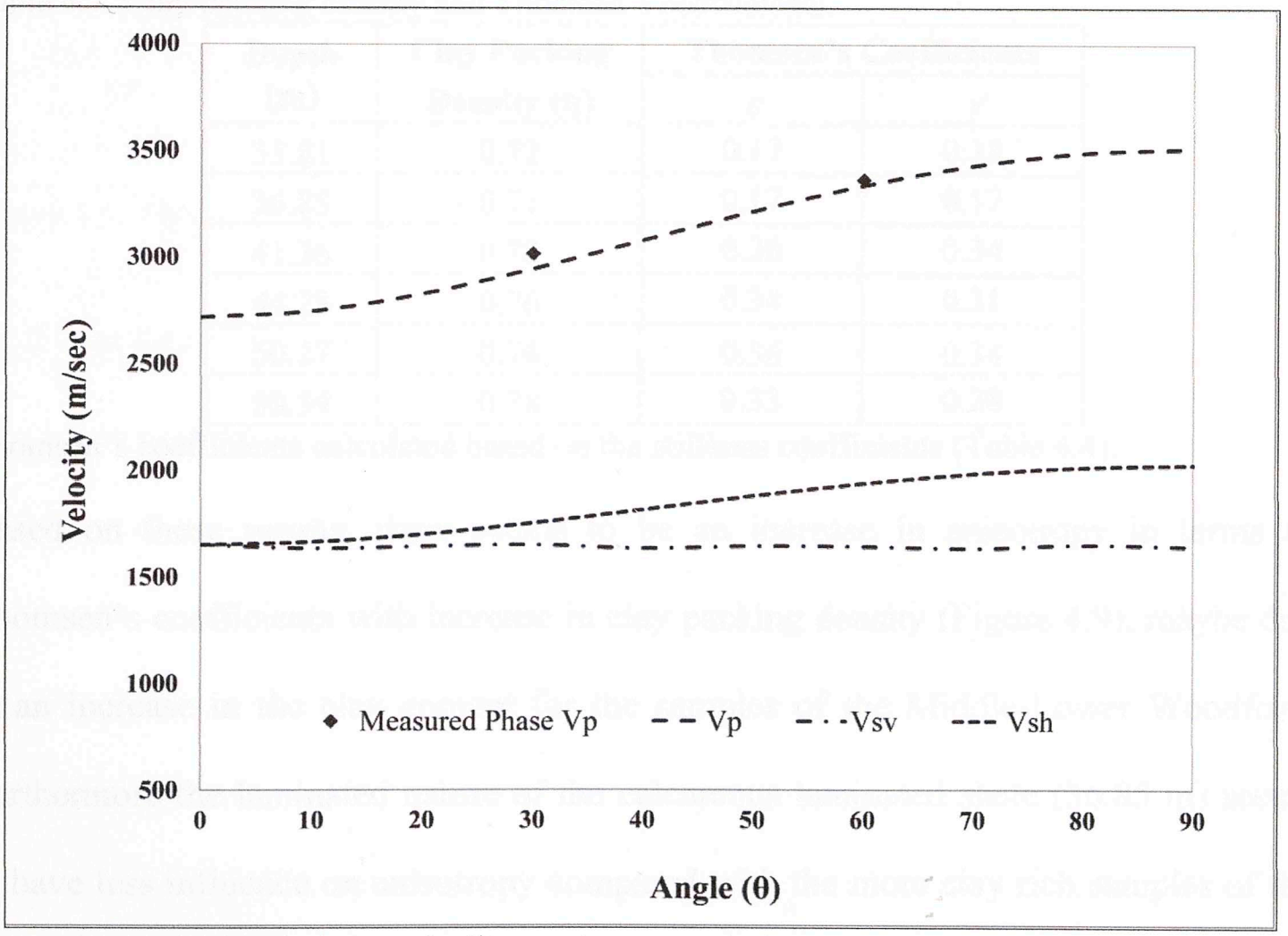

Figure 4.8. Calculated phase velocities and measured phase velocities for the sample at 50.27 m (164.94 ft).

Thomsen's coefficients (Thomsen, 1986) are commonly used in geophysics to characterize the degree of acoustic anisotropy, where ε and γ are related to the anisotropy of the P and S velocities respectively. These parameters can be calculated from the stiffness coefficients in the vertical and horizontal direction as (Thomsen, 1986):

$$\varepsilon = \frac{C_{11} - C_{33}}{2C_{33}} \tag{3.28}$$

$$\gamma = \frac{C_{66} - C_{44}}{2C_{44}} \tag{3.29}$$

Table 4.7 presents the calculated Thomsen's coefficients based on the UPV measurements along with the clay packing density (Table 4.1).

Table 4.7. Clay packing density and Thomsen's coefficients.

Depth (m)	**Clay Packing Density (η)**	**Thomsen's Coefficients**	
		ε	γ
33.81	0.72	0.17	0.18
36.85	0.71	0.17	0.17
41.36	0.78	0.26	0.34
44.28	0.76	0.34	0.31
50.27	0.76	0.36	0.34
50.59	0.78	0.33	0.28

Thomsen's coefficients calculated based on the stiffness coefficients (Table 4.4).

Based on these results, there seems to be an increase in anisotropy in terms of Thomsen's coefficients with increase in clay packing density (Figure 4.9), maybe due to an increase in the clay content for the samples of the Middle-Lower Woodford. Furthermore the laminated nature of the calcareous laminated shale (36.85 m) seems to have less influence on anisotropy compared with the more clay rich samples of the Middle and Lower Woodford. This suggests that the clay associated fabric at the

micro-scale might have direct influence in the acoustic anisotropy. This seems to be even higher than the influence of the thickly laminated fabric of intercalated lithologies at the millimeter scale present in the calcareous laminated shale.

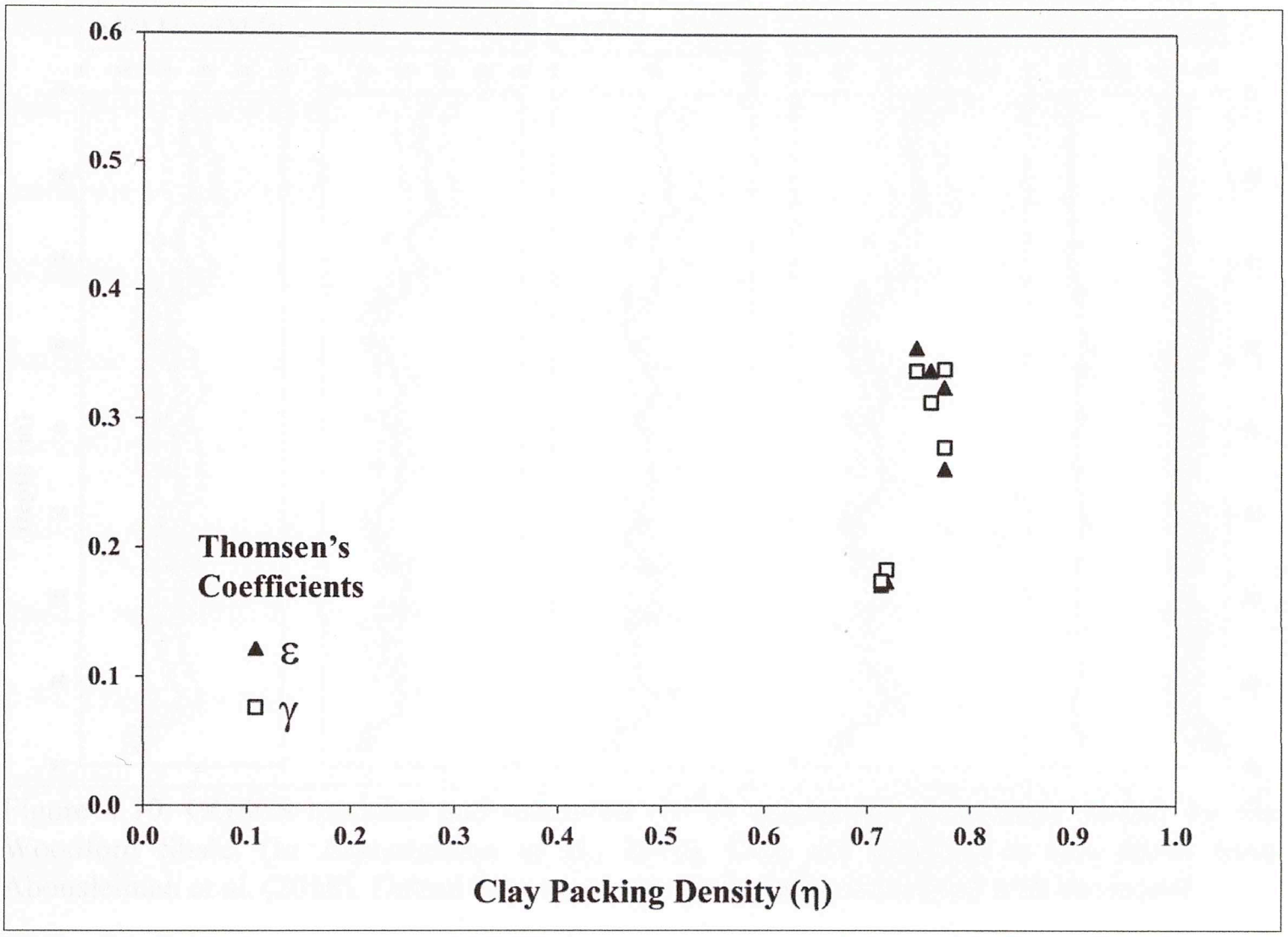

Figure 4.9. Thomsen's coefficients vs. Clay packing density

4.2.2 The GGSCS

The input parameters for the GGSCS upscaling model were the ECS mineralogy log, which presents good agreement with the XRD results (Abousleiman et al., 2007) and the previously mentioned calibrated porosity log. Figure 4.10 presents the modeled logs for the 7 poroelastic parameters necessary for the complete characterization of the transverse isotropic nature of the Woodford. Figure 4.10 also presents the values obtained from UPV measurements for the tested samples, showing the good

agreement between the UPV measurements and the modeled results (Abousleiman et al., 2010).

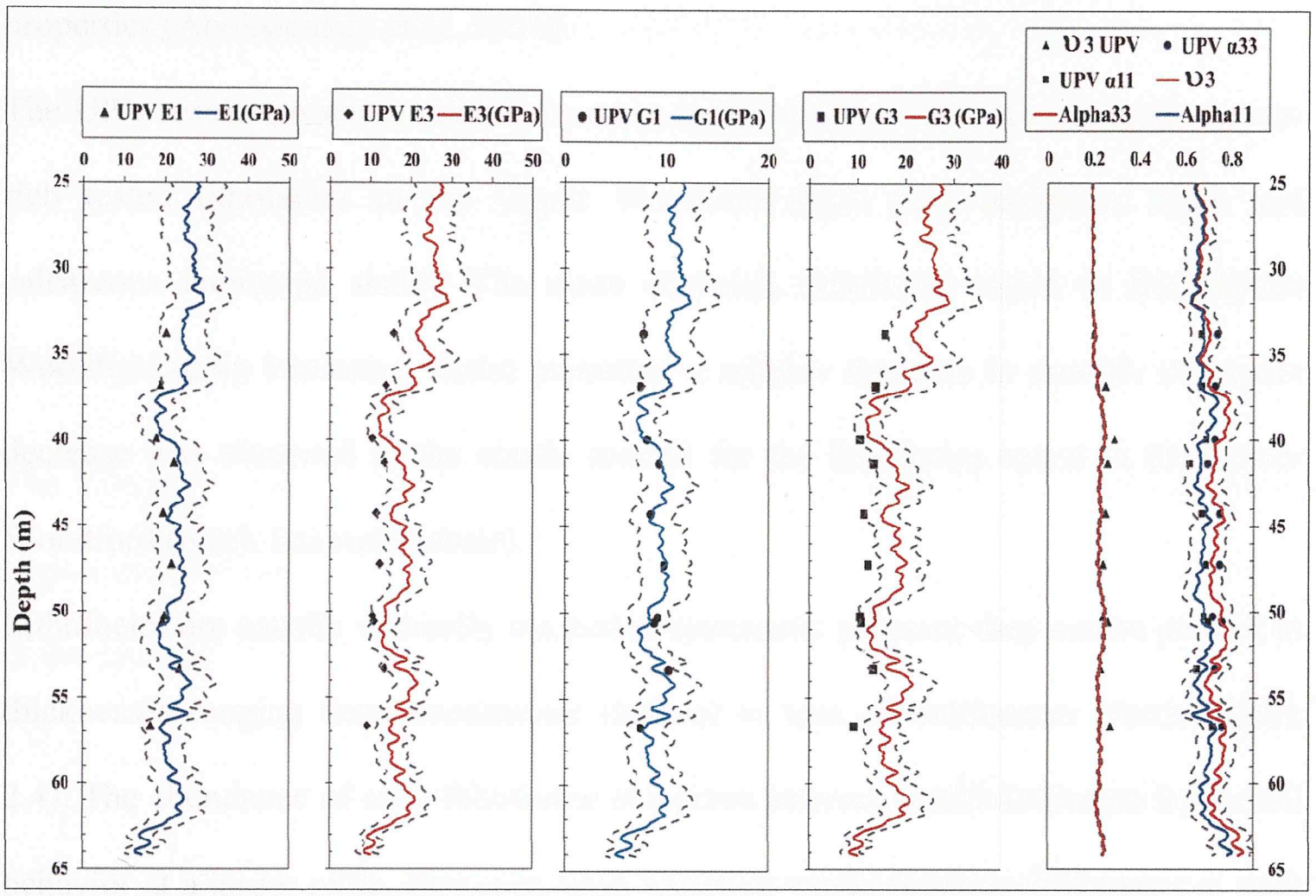

Figure 4.10. GGSCS modeled and measured (UPV) anisotropic poroelastic moduli for the Woodford Shale. (In Abousleiman et al., 2010). Data not included in this thesis from Abousleiman et al. (2010). Dotted lines represent the variance associated with the model.

Mineralogy has been suggested to control the mechanical response of shale formations. Therefore, having a direct influence on hydraulic fracturing response (Harris et al., 2011). The GGSCS provides a powerful tool for acquiring the anisotropic poroelastic moduli of the Woodford. These are not possible to acquire with well log data. Currently, the dipole sonic tool can measure the Shear Modulus (G_1) in the horizontal direction (Pistre et al., 2005). However, the calculation of Young's Modulus (E_1) in such a direction is based on simplified anisotropic models, developed based on observations in specific shale formations (Schoenberg et al., 1996), which are known to behave differently (Mattews et al., 2007; Slatt et al., 2008, Britt and

Schoeffler, 2009). Furthermore, the GGSCS results have been proven to present a better correlation with the laboratory results than the sonic-log derived mechanical properties (Abousleiman et al., 2010).

The UPV results present a relative increase in the elastic moduli for the more quartz-rich tested lithofacies in the Upper Woodford (light gray laminated shale and calcareous laminated shale). The more clay-rich lithofacies tested in the Middle Woodford (gray laminated shale) presented a relative decrease in moduli. A greater decrease was observed in the elastic moduli for the lithofacies tested in the Lower Woodford (black laminated shale).

Lithofacies are usually vertically stacked in systematic patterns; they can be present in thicknesses ranging from centimeters (inches) to tens of centimeters (feet) (Figure 2.4). The abundance of such lithofacies in a given interval would determine its overall behavior at a larger scale. However, such variation would produce differences at such scale, which might cause complexity for field applications such as drilling and hydraulic fracturing (Slatt and Abousleiman, 2011). Since the ECS log has a vertical resolution of 47.72 cm (1.5 ft) (Schlumberger, 2011), the modeled properties can be regarded as those at such scale. Hence, they can be used for field applications such as the ones proposed in this chapter.

4.2.3 Standard methodology vs. IDSTD™

Figure 4.11 presents the stress vs. strain plot for the uniaxial compressive test performed with the sample at 50.18 m (164.63 ft). The resulting UCS is 56.5 MPa (8200 psi). The quasi-static Young's Modulus and Poisson's Ratio calculated at 50% of the total stress are 5.49 GPa (797,500 psi) and 0.21 respectively. The Young's

Modulus represents the vertical stiffness or E_3 in the notation here used. Four small load-unload cycles were conducted at a faster rate in order to obtain the small strain mechanical properties (Figure 4.11); the results are summarized in Table 4.8.

Table 4.8. Young's Modulus for measurements at small strain, unconfined compressive test.

Axial Stress (MPa)	Cycling E (GPa)
6.07	7.80
12.48	9.92
19.10	9.55
27.10	9.82

The relatively small value at 6.07 MPa can be associated with the early nonlinear region in the stress- strain plot, which might be a result of the closure of micro-cracks in the sample.

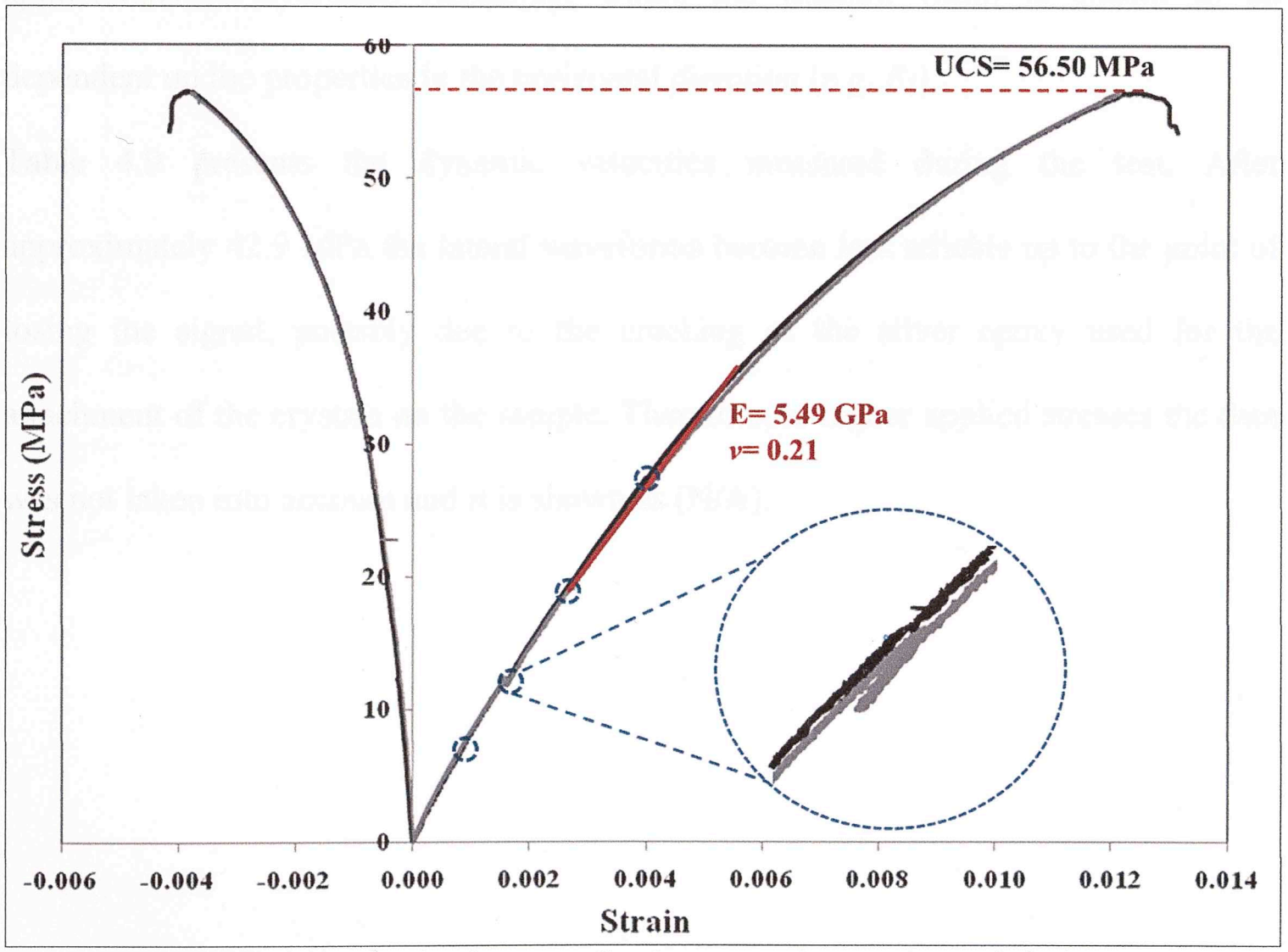

Figure 4.11. Stress vs. Strain plot for unconfined compressive test. Dotted circles represent the four small strain cycles.

The small strain Young's Modulus can be correlated to the quasi static E_3 by a factor of 1.7. Similar correlation between the equivalent dynamic E_3 and the small strain Young's Modulus results in a correlation factor of 1.8. As expected, the dynamic moduli are higher in magnitude than the quasi-static moduli, approaching the small strain moduli for the vertical direction. The resulting quasi-static to dynamic comparison in Young's Modulus results in a factor of 3.2. A correlation between the lateral quasi-static moduli and the dynamic moduli in the same direction was not possible due to the lack of quasi-static tests performed in lateral plugs.

Such factors are useful for correlation between the sonic log-derived modulus and the quasi static modulus when the last one is needed; such is the case of wellbore stability applications or hydraulic fracturing, where the fracture width is known to be dependent on the properties in the horizontal direction (e.g. E_1).

Table 4.9 presents the dynamic velocities measured during the test. After approximately 42.9 MPa the lateral waveforms become less reliable up to the point of losing the signal, possibly due to the cracking of the silver epoxy used for the attachment of the crystals on the sample. Therefore, at higher applied stresses the data was not taken into account and it is shown as (N/A).

Table 4.9. Measured velocities during uniaxial test

Velocities (m/sec)						
	Lateral				Axial	
Stress (MPa)	*P*	*P45*	*S1*	*S2*	*P*	*S2*
0.21	3398	3068	1699	2020	2964	1606
2.89	3375	3068	1699	2012	2964	1606
5.59	3375	3068	1702	2012	2972	1619
8.29	3375	3068	1705	2004	2988	1619
10.89	3375	3068	1705	2004	2988	1619
13.59	3375	3068	1711	2004	2988	1631
16.29	3375	3068	1711	1996	3014	1631
18.89	3375	3095	1711	1996	3022	1643
21.59	3375	3095	1716	1996	3039	1643
24.29	3375	3108	1716	1988	3057	1643
26.89	3375	3135	1688	1988	3057	1656
32.29	3353	3135	1688	1980	3065	1656
34.99	3353	3135	1688	1972	3065	1656
37.59	3353	3135	1633	1965	3065	1656
40.29	3353	3135	1633	1949	3065	1669
42.99	3353	3135	N/A	N/A	3083	1669
45.59	3331	3135	N/A	N/A	3101	1682
48.59	N/A	N/A	N/A	N/A	3101	1682
50.99	N/A	N/A	N/A	N/A	3101	1682
53.69	N/A	N/A	N/A	N/A	3101	1682

The suffixes make reference to Figure 3.8.

From such velocities the elastic stiffness coefficients were calculated. Table 4.10 presents the calculated C_{ij} and Thomsen's coefficients. Table 4.11 presents the poroelastic coefficients.

Table 4.10. Calculates Stiffness coefficients and Thomsen's coefficients.

UCS Stiffness Coefficients (GPa)							Thomsen's Coeff.	
Stress (MPa)	*C11*	*C33*	*C44*	*C66*	*C12*	*C13*	ε	γ
0.2	26.00	19.78	6.15	9.19	7.63	6.83	0.16	0.25
2.9	25.66	19.78	6.15	9.11	7.43	7.05	0.15	0.24
5.6	25.66	19.89	6.21	9.11	7.43	6.89	0.14	0.23
8.2	25.66	20.11	6.22	9.04	7.57	6.78	0.14	0.23
10.9	25.66	20.11	6.22	9.04	7.57	6.78	0.14	0.23
13.6	25.66	20.11	6.29	9.04	7.57	6.64	0.14	0.22
16.2	25.66	20.45	6.29	8.97	7.72	6.51	0.13	0.21
18.9	25.66	20.57	6.33	8.97	7.72	7.11	0.12	0.21
21.6	25.66	20.80	6.36	8.97	7.72	6.97	0.12	0.21
24.2	25.66	21.04	6.36	8.90	7.86	7.25	0.11	0.20
29.6	25.66	21.04	6.29	8.90	7.86	8.15	0.11	0.21
32.3	25.32	21.16	6.29	8.83	7.66	8.30	0.10	0.20
34.9	25.32	21.16	6.29	8.76	7.80	8.30	0.10	0.20
37.6	25.32	21.16	6.09	8.69	7.93	8.71	0.10	0.21
40.3	25.32	21.16	6.14	8.56	8.20	8.61	0.10	0.20
42.9	25.32	21.41	6.27	N/A	N/A	N/A	0.09	N/A

The results show an overall increase in the stiffness coefficients with increments of applied stress in the vertical direction. The relative decrease of C_{11}, and C_{66} might be attributed to the weakening of the horizontal bedding planes once shear stresses were generated. There is also a decrease in anisotropy with applied stress due to the stiffening of the material as it is compressed. Similar trends can be observed in the more widely used poroelastic moduli as shown in Table 4.11.

Table 4.11. UCS Poroelastic moduli

Poroelastic moduli (GPa)							
Stress (MPa)	*E1*	*E3*	*υ3*	*G1*	*G3*	*α1*	*α3*
0.2	22.47	17.00	0.20	9.19	6.15	0.63	0.69
2.9	22.10	16.77	0.21	9.11	6.15	0.63	0.69
5.6	22.18	17.02	0.21	9.11	6.21	0.63	0.69
8.2	22.17	17.34	0.20	9.04	6.22	0.63	0.69
10.9	22.17	17.34	0.20	9.04	6.22	0.63	0.69
13.6	22.23	17.46	0.20	9.04	6.29	0.63	0.69
16.2	22.24	17.92	0.20	8.97	6.29	0.63	0.69
18.9	22.01	17.54	0.21	8.97	6.33	0.63	0.68
21.6	22.08	17.89	0.21	8.97	6.36	0.63	0.68
24.2	21.92	17.90	0.21	8.90	6.36	0.62	0.67
29.6	21.52	17.08	0.24	8.90	6.29	0.61	0.65
32.3	21.18	16.99	0.25	8.83	6.29	0.62	0.65
34.9	21.13	17.00	0.25	8.76	6.29	0.62	0.65
37.6	20.86	16.60	0.26	8.69	6.09	0.61	0.64
40.3	20.80	16.74	0.26	8.56	6.14	0.61	0.64
42.9	N/A	N/A	N/A	N/A	6.27	N/A	N/A

Three samples corresponding to the following depths were selected to be tested with the IDSTD^{TM}: 33.81 m (110.48 ft), 36.85 m (120.93 ft), and 50.26 m (164.89 ft). For the last one an extra test was performed at 0.35 MPa (50 psi) confining pressure. This allowed the analysis of a wider range of confining pressures and the validation of a linear Mohr-Coulomb failure criteria for such range.

Figure 4.12 presents the typical deviatoric stress vs. strain analysis for the IDSTD^{TM}, in this case for the sample at 33.81 m (110.48 ft). The strength values were taken from the peak deviatoric stresses of both tests at 6.89 MPa (1000 psi) and 13.79 MPa (2000 psi) confining pressures. Table 4.12 summarizes the results for the IDSTD^{TM} tests. Such strength values were used for the calculation of Cohesion (*Co*) and friction angle (ϕ) using the previously mentioned Mohr-Coulomb criteria (Table 4.13)

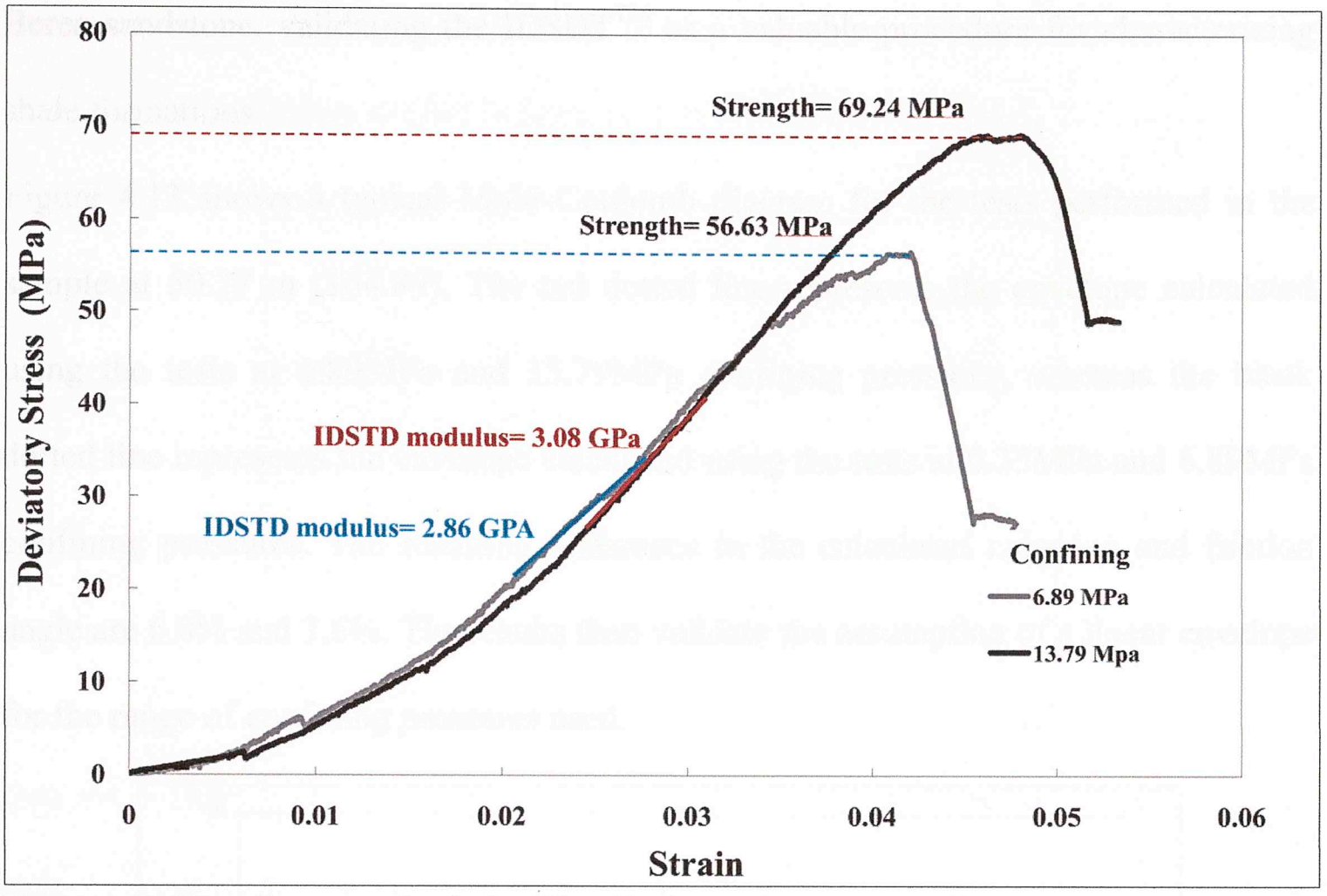

Figure 4.12. Dev. Stress vs. Strain for Woodford samples corresponding to 33.81 m at different applied confining pressures.

Table 4.12. IDSTD™ Results.

Depth (m)	IDSTD Modulus (GPa)			Dev. Strength (MPa)		
	0.35MPa	6.89MPa	13.79MPa	0.35MPa	6.89MPa	13.79MPa
33.81	N/A	2.86	3.08	N/A	56.63	69.24
36.85	N/A	3.19	3.22	N/A	90.66	92.73
50.27	1.97	2.27	2.78	64.46	73.77	80.46

The second raw makes reference to the different confining pressures used.

For the sample at 50.26 m at 0.35 MPa (50 psi), almost equivalent to an unconfined test, a difference is expected with the uniaxial compressive test due to differences in sample size and loading characteristics (Abousleiman, 2010). The resulting difference in maximum deviatoric stress and the UCS is 13%, showing good agreement within both techniques. The comparison between the IDSTD™ modulus and the quasi-static *E* of the uniaxial compressive test resulted in a correlation factor of 2.9. The results are close to those proposed by Abousleiman et al. (2010) for a similar comparison in

Berea sandstone, validating the IDSDT™ as a valuable procedure for characterizing shale formations.

Figure 4.13 shows a typical Mohr-Coulomb diagram for the tests performed in the sample at 50.27 m (164.89). The red dotted line represents the envelope calculated using the tests at 6.89MPa and 13.79MPa confining pressures, whereas the black dotted line represents the envelope calculated using the tests at 0.35MPa and 6.89MPa confining pressures. The resulting difference in the calculated cohesion and friction angle are 6.8% and 7.6%. The results then validate the assumption of a linear envelope for the range of confining pressures used.

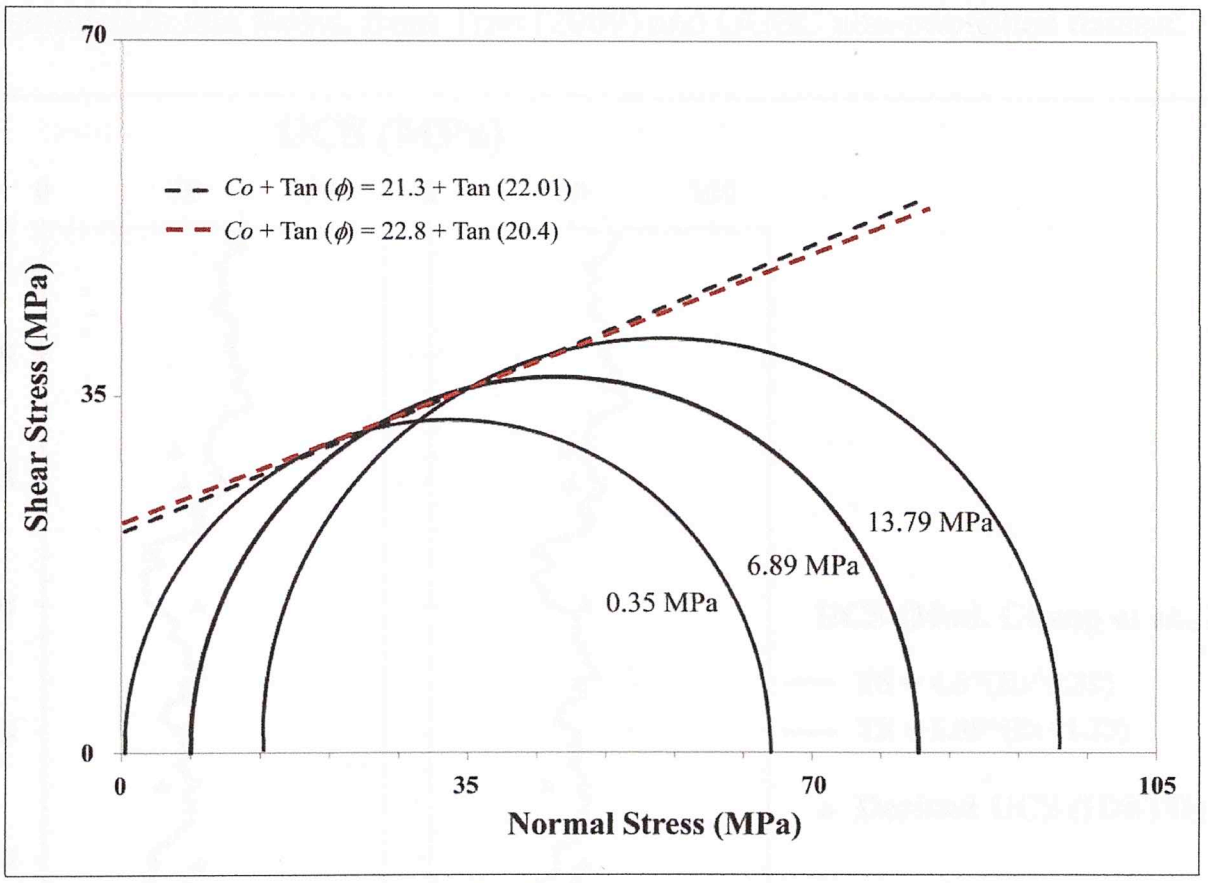

Figure 4.13. Mohr-Coulomb failure criteria calculated with the tests performed in sample at 50.27 m.

The UCS in the vertical direction was calculated (Table 4.13) based on the calculated *Co* and ϕ, and using a linear failure criteria. Following Chang et al. 2004 (in Mavko et al., 2010), correlations between vertical UCS and dynamic anisotropic Young's Modulus were proposed for the Woodford Shale. Figure 4.14 presents the UCS

derived from IDSTD™ results and the corresponding correlations proposed in terms of E_1 and E_3, parameter available from the GGSCS upscaling model.

Table 4.13. Calculated *Co*, ϕ, and UCS.

Depth (m)	Cohesion (MPa)	Fric. Angle (Calculated)	UCS
33.81	13.81	29.0	46.89
35.10	12.10	38.0	49.62
36.85	38.09	7.5	86.87
39.93	22.89	9.9	54.46
47.10	12.98	26.0	41.54
50.26	22.04	20.0	62.95
51.13	20.80	12.0	51.37
53.49	9.94	30.5	34.78
56.41	25.51	1.4	52.28

Data not included in this thesis, from Tran (2009) and GGSC non-published dataset.

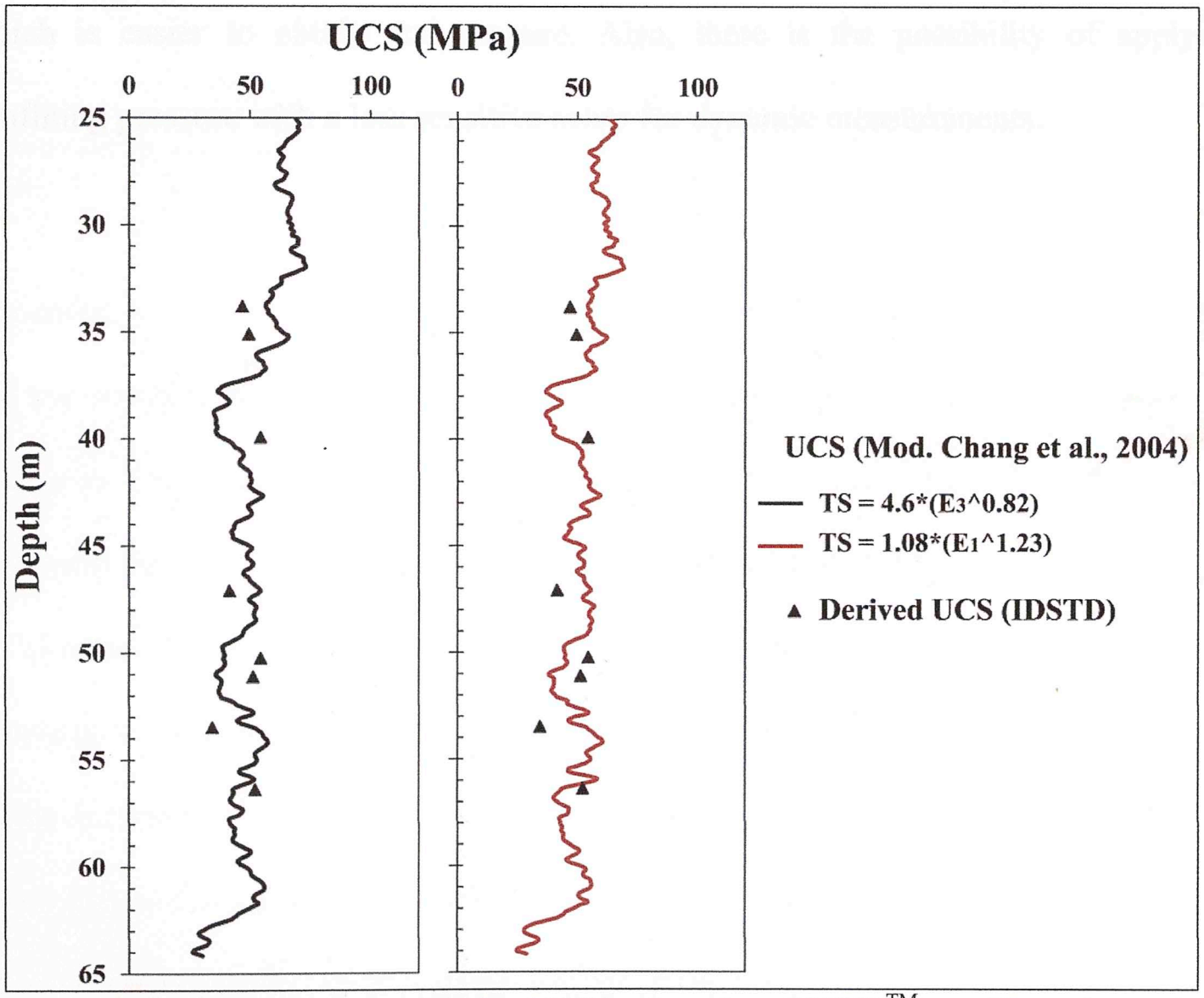

Figure 4.14. Vertical UCS log and derived UCS values from IDSTD™ test. The anisotropic Young's Modulus used in the correlations is specified.

As previously discussed, acoustic measurements were taken at different applied stresses. Figure 4.15 presents the calculated dynamic elastic moduli for the sample at 50.26 m at different applied stresses along with the results of the unconfined compressive test (Table 4.10). The results show good agreement with maximum differences of 15% for similar applied stresses in the range where a comparison was possible. The difference is highly influenced by the differences in sample sizes and loading characteristics. The previously mentioned damage induced in the crystals for the uniaxial test can contribute to the difference at higher applied stresses. The results then suggest that either technique can provide similar dynamic characterization capabilities. Furthermore, the IDSTD^{TM} has the advantage of using a smaller sample, which is easier to obtain and prepare. Also, there is the possibility of applying confining pressure with a less sensitive setup for dynamic measurements.

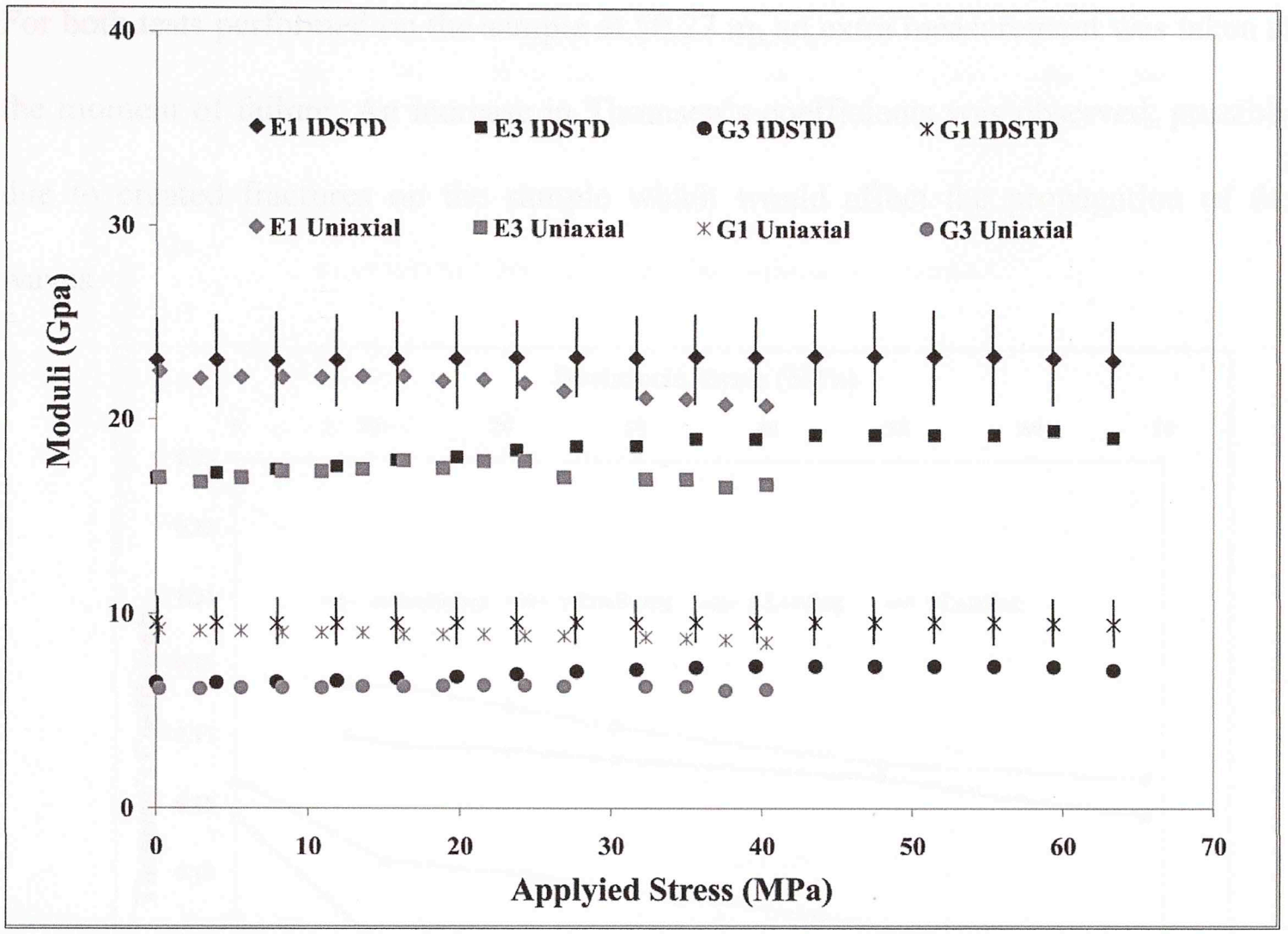

Figure 4.15. Comparison UCS and IDSTD (0.35 MPa conf.) for sample at 50.26 m. Bars correspond to standard deviation inherent to the dynamic modeling for the IDSTD™ (Tran, 2009).

Appendix A contains all the measured velocities, the calculated stiffness coefficients and the poroelastic moduli for all the tests performed. Figures 4.16 - 4.19 present the change in Thomsen's coefficients with applied stress for such tests. The results show an overall decrease in Thomsen's coefficients with confining pressure possibly due to the closure of microcracks present in the sample. During axial loading a decrease in Thomsen's coefficients was also observed. Such behavior is the result of the relatively higher increase in C_{33} and C_{44} due to the axial compaction relative to C_{11} and C_{66}. These last two have also been observed to decrease due to the generation of micro-cracks forming parallel to axis of symmetry of the sample (Tran, 2009; Abousleiman et al., 2010)

For both tests performed on the sample at 50.27 m, an extra measurement was taken at the moment of failure. An increase in Thomsen's coefficients was observed, possibly due to created fractures on the sample which would affect the propagation of the waves.

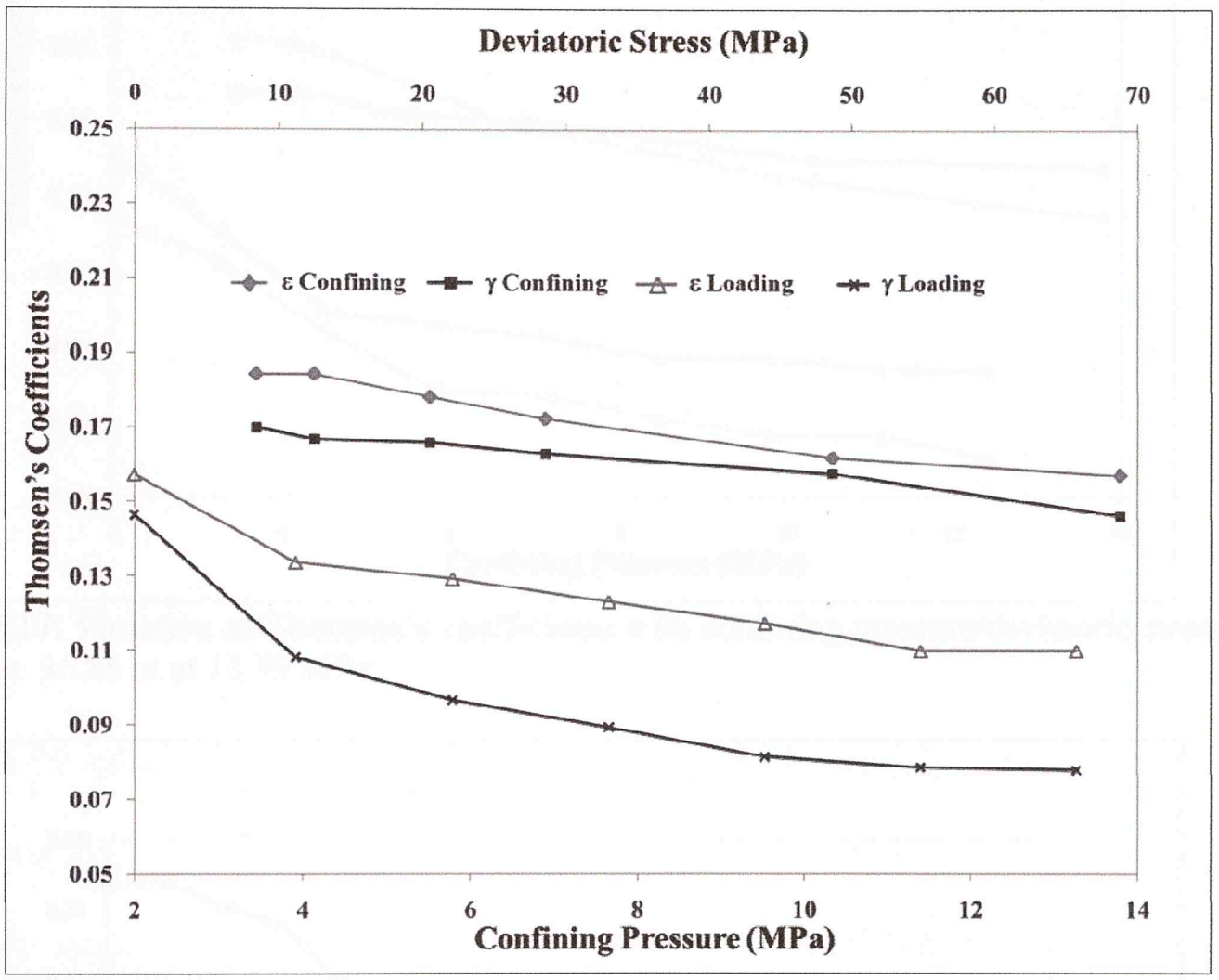

Figure 4.16. Variation of Thomsen's coefficients with confining pressure/deviatoric stress for sample at 33.81 m at 13.79 MPa.

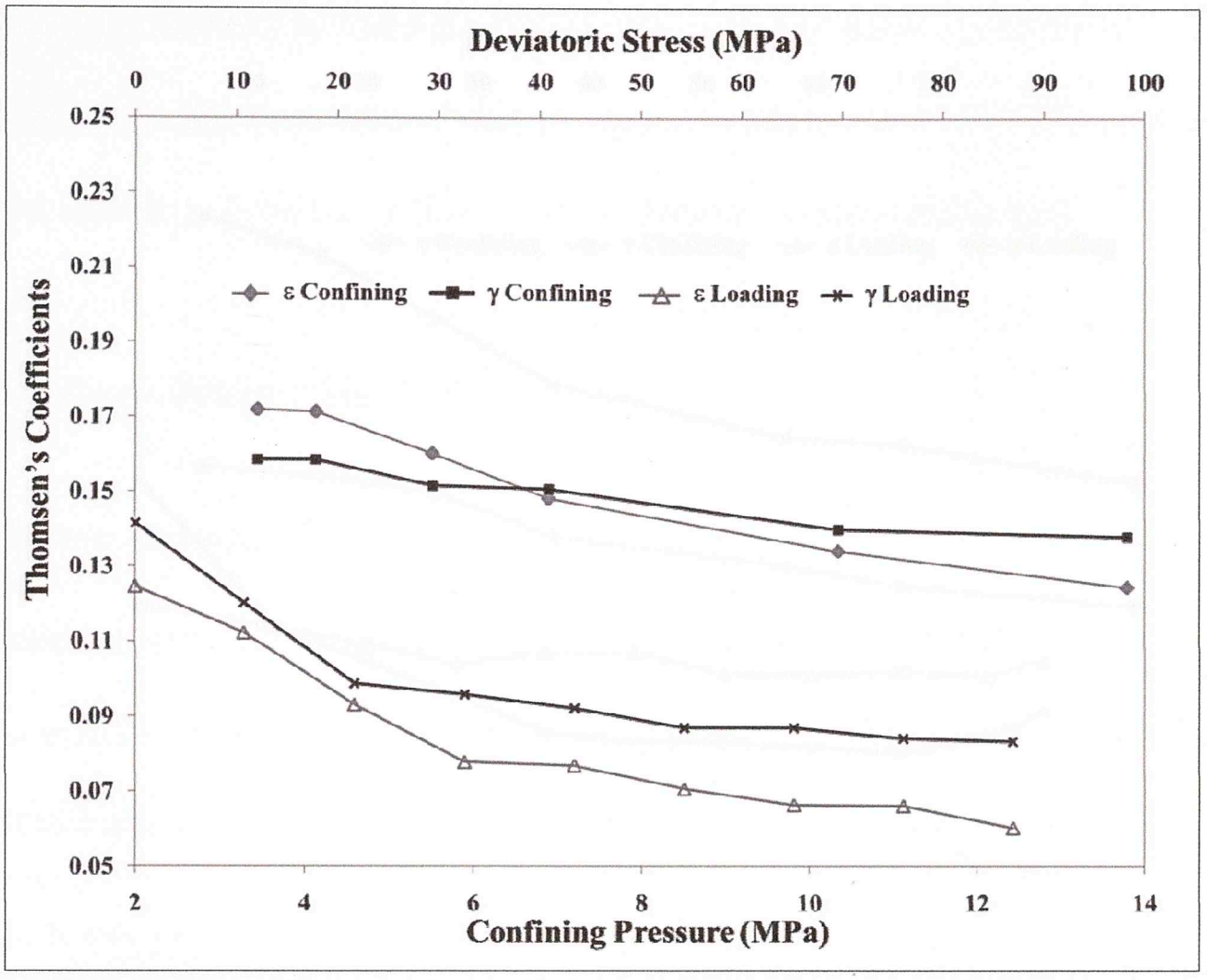

Figure 4.17. Variation of Thomsen's coefficients with confining pressure/deviatoric stress for sample at 36.85 m at 13.79 MPa.

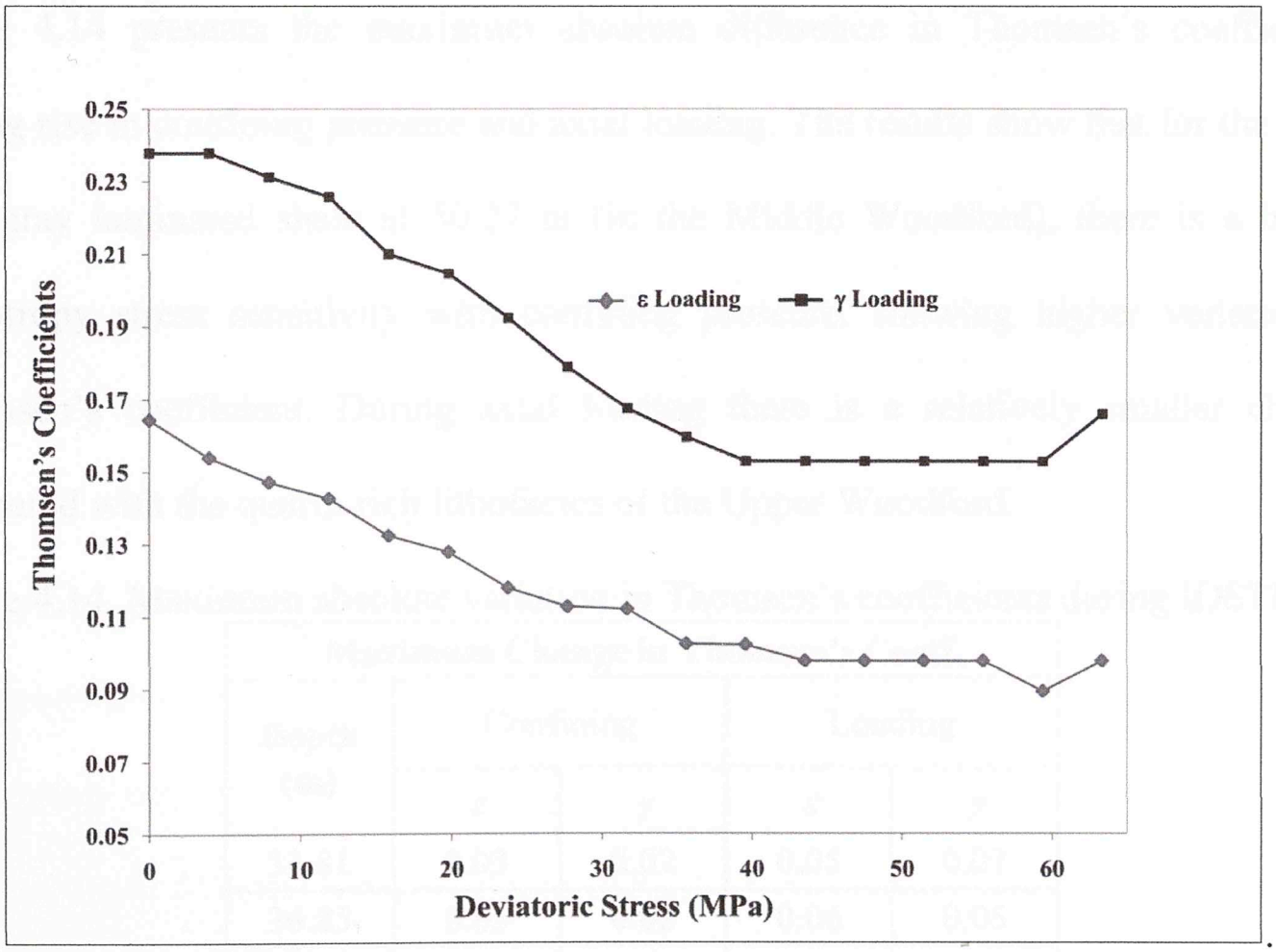

Figure 4.18. Variation of Thomsen's coefficients with confining pressure/deviatoric stress for sample at 50.27 m at 0.35 MPa.

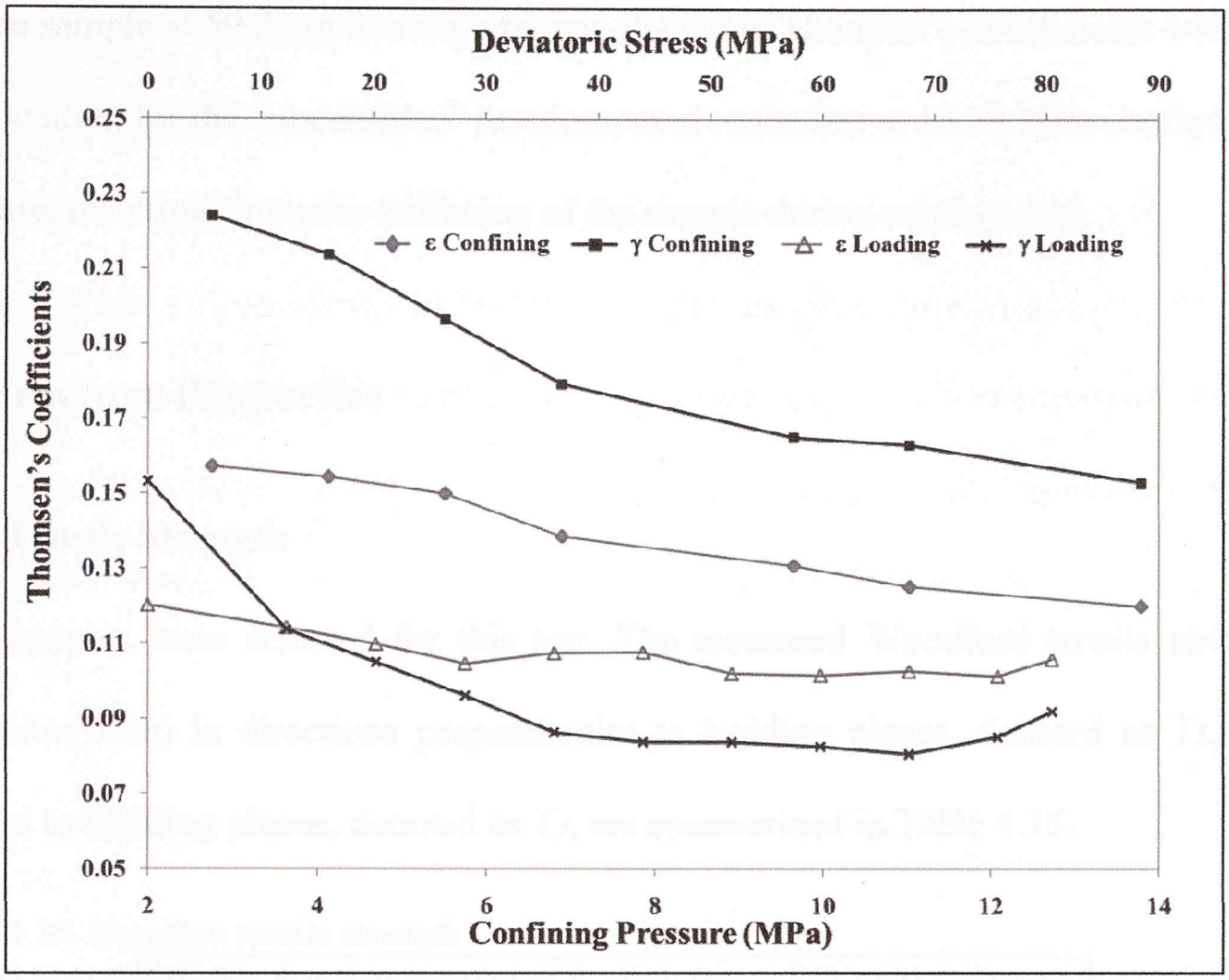

Figure 4.19. Variation of Thomsen's coefficients with confining pressure/deviatoric stress for sample at 50.27 m at 13.79 MPa.

Table 4.14 presents the maximum absolute difference in Thomsen's coefficients during rise in confining pressure and axial loading. The results show that for the clay-rich gray laminated shale at 50.27 m (in the Middle Woodford), there is a higher anisotropy stress sensitivity with confining pressure, showing higher variation in Thomsen's coefficient. During axial loading there is a relatively smaller change compared with the quartz-rich lithofacies of the Upper Woodford.

Table 4.14. Maximum absolute variation in Thomsen's coefficients during IDSTD™.

Maximum Change in Thomsen's Coeff.				
Depth (m)	Confining		Loading	
	ε	γ	ε	γ
33.81	0.03	0.02	0.05	0.07
36.85	0.05	0.02	0.06	0.05
50.27	0.04	0.08	0.02	0.04
50.27*	N/A	N/A	0.08	0.09

For the sample at 50.27 m there is a bigger change in Thomsen's coefficients with axial loading for the "unconfined" test compared to the test at 13.79 MPa confining pressure, resulting from the stiffening of the sample during confinement.

4.3 Fracture Properties

4.3.1 Tensile Strength

Five samples were selected for this test. The measured Woodford tensile strengths (Equation 3.26) in directions perpendicular to bedding planes, denoted as $T_{\perp}$, and parallel to bedding planes, denoted as $T_{//}$, are summarized in Table 4.15.

Table 4.15. Brazilian tensile strength

Depth (m)	Load Direction (rel. to bedding)	Max. Load (N)	Tensile Strength (MPa)
33.81	⊥	3747	12.84
	//	2351	6.16
36.85	⊥	3556	12.65
	//	1989	7.40
41.36	⊥	3347	11.43
	//	1956	5.02
44.28	⊥	3140	11.19
	//	1920	5.06
50.59	⊥	3276	11.69
	//	1609	4.35

The results show the anisotropic nature of Woodford tensile strength, suggesting that rock fabric (laminations and clay microfabric) has a direct influence on rock strength. Comparing the difference in mineralogy among the samples, the results suggest a secondary role of mineralogy in tensile strength (Sierra et al., 2010)

There seems to be a slight increase in tensile strength for the samples corresponding to the Upper Woodford. Similar to Thomsen's coefficients, the tensile strength anisotropy ratio ($T\perp/T_{//}$) exhibits an increasing trend with increased clay packing density (Table 4.1) as shown in Figure 4.20; the samples corresponding to the clay-rich Middle and Lower Woodford have the highest ratios. Such observation suggests that the horizontally-oriented clay microfabric contributes to the increase in tensile strength anisotropy in a more representative way than the laminations at the mm scale.

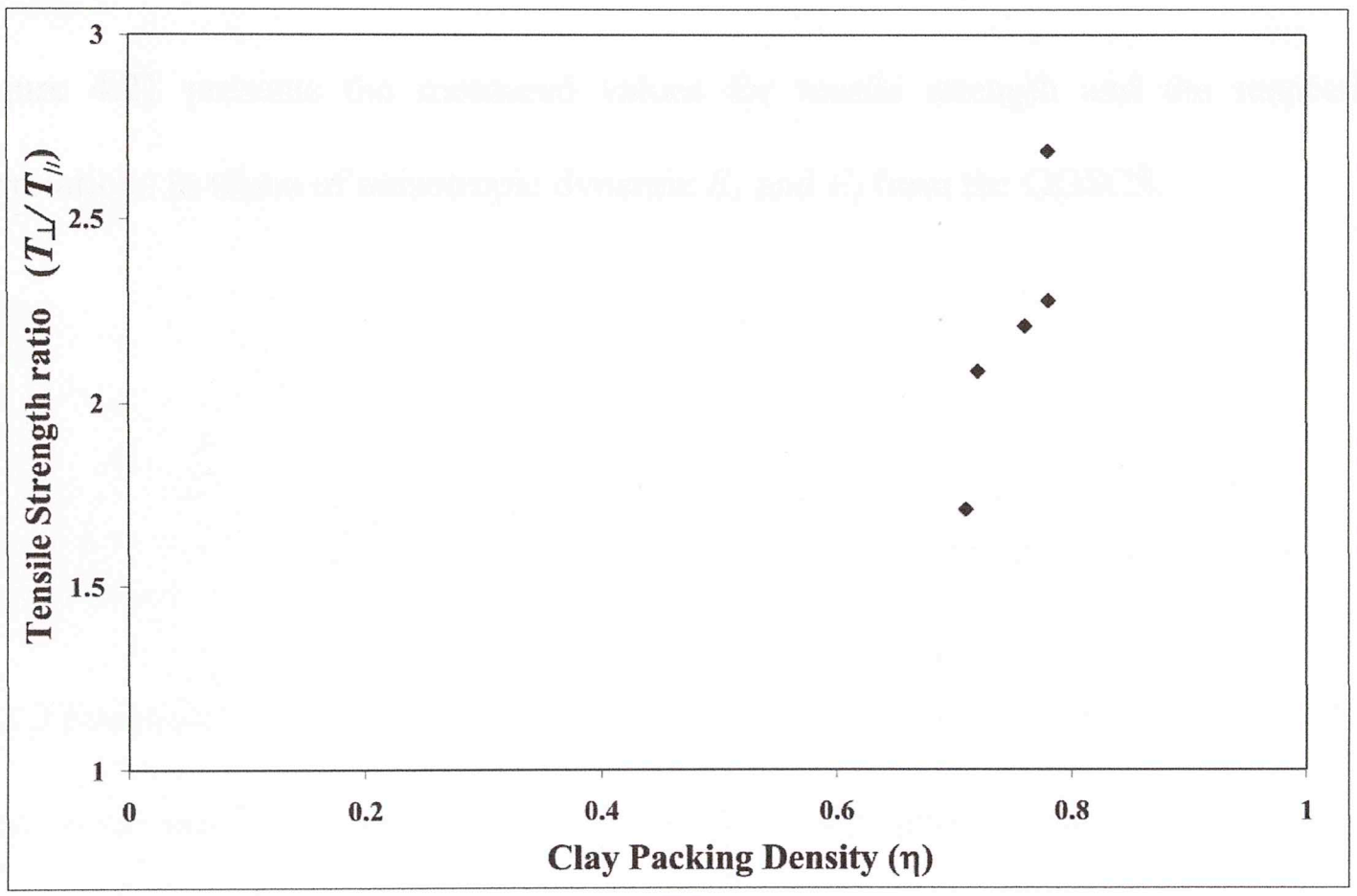

Figure 4.20. Tensile strength anisotropy vs. Clay packing density.

Following the previously mention UCS correlation and assuming that tensile strength is at least one order of magnitude less than the UCS, a correlation widely used in the industry (Economides and Martin, 2007), the tensile strength correlations show good correlation with the measured values. Hence, the vertical UCS can be correlated to the

vertical tensile strength (loaded parallel to the bedding planes, $T_{//}$) by a factor of 0.1 taking into account the limited number of laboratory measurements.

The lateral tensile strength (loaded perpendicular to the bedding planes, $T\perp$) could not be compared with a lateral UCS correlation due to the lack of such measurement in the laboratory, which has been observed to be different in laminated shales (Gallant et al., 2007). However, similar correlations were derived for $T\perp$ in terms of the upscaled dynamic E_1 and E_3.

Figure 4.21 presents the measured values for tensile strength and the respective correlations in terms of anisotropic dynamic E_1 and E_3 from the GGSCS.

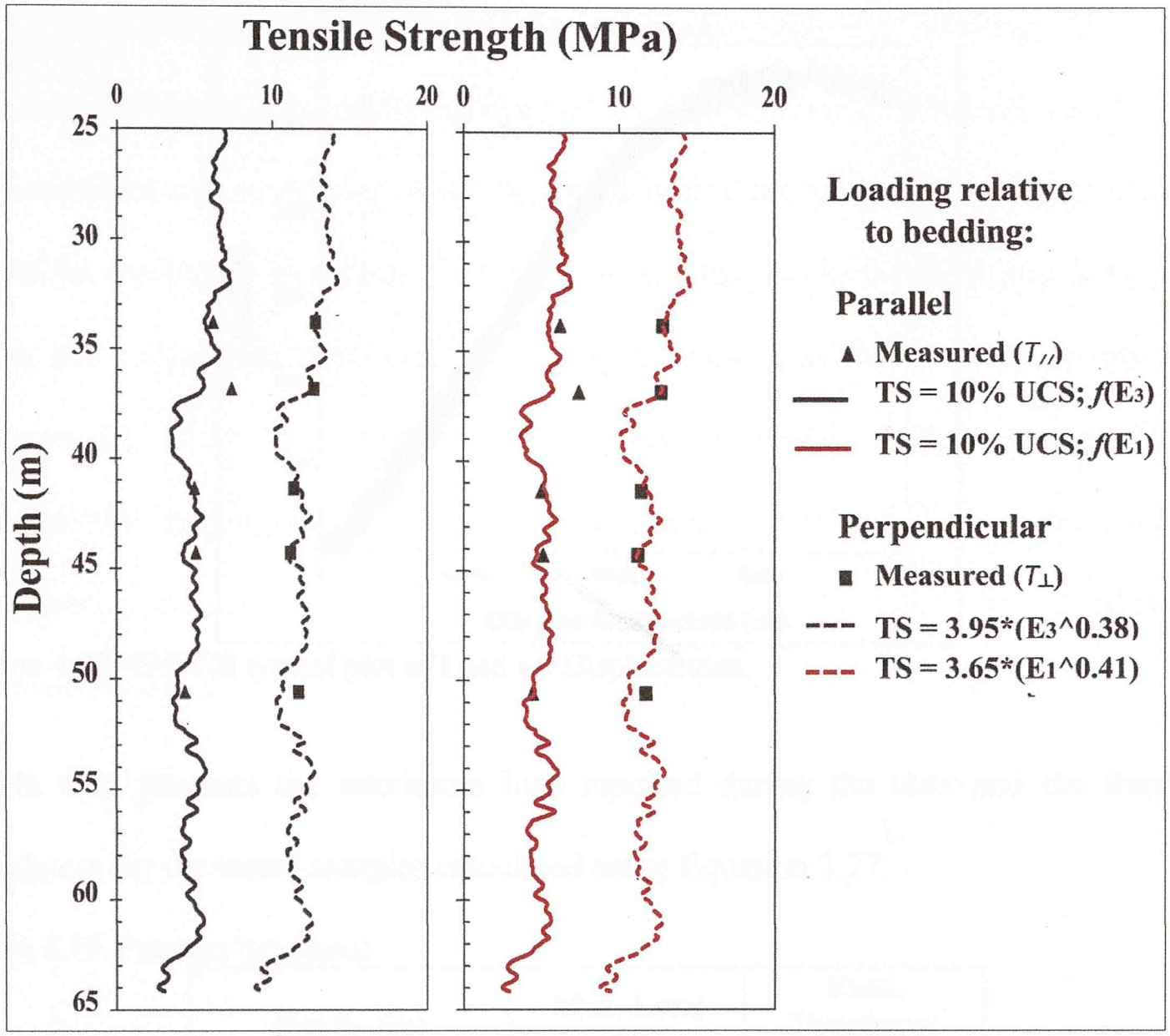

Figure 4.21. Tensile strength logs and measured values. The anisotropic Young's Modulus used in the correlations is specified.

4.3.2 Fracture Toughness and AE

The same samples tested for tensile strength were also selected for the fracture toughness evaluation. A typical plot of applied load versus clip gage displacement for CNSCB test is shown in Figures 4.22, from which the region of stable crack propagation can be observed as the plateau in the figure.

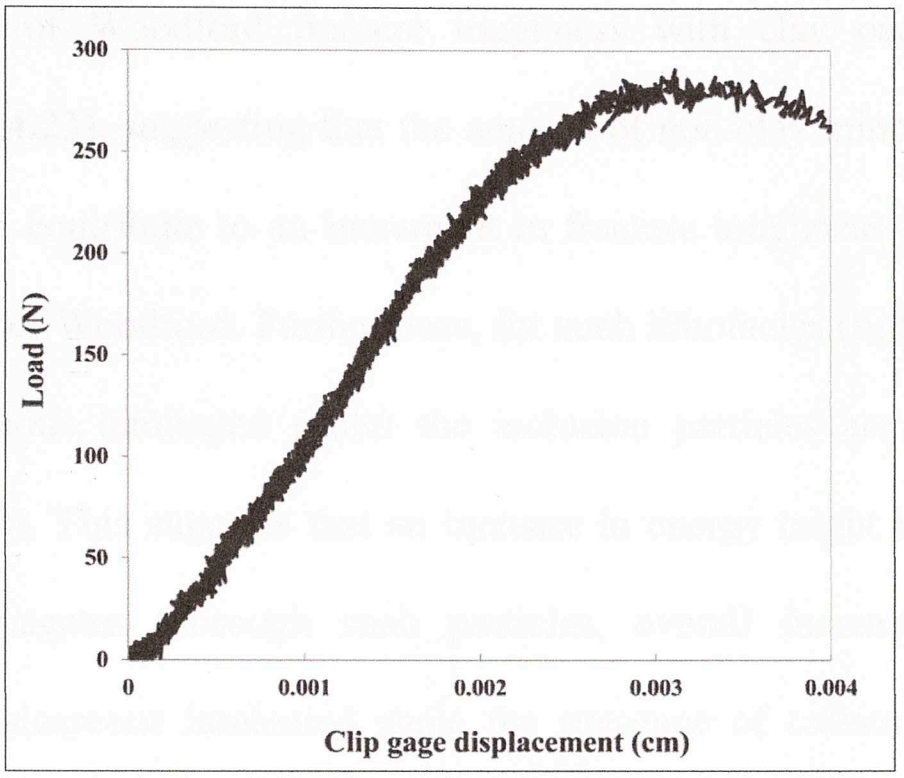

Figure 4.22. CNSCB typical plot of Load vs. Displacement.

Table 4.16 presents the maximum load reported during the tests and the fracture toughness for the tested samples calculated using Equation 3.27.

Table 4.16. Fracture toughness

Depth (m)	Max. Load (N)	Frac. Toughness (MPa√m)
33.81	489	1.17
36.85	133	1.15
41.36	83	0.65
44.28	89	0.74
50.59	89	0.74

Despite the small number of tests, the results might suggest insignificant variation of fracture toughness between samples in the Upper Woodford as well as between samples in the Middle and Lower Woodford, however more tests are required for a complete characterization of variations in fracture toughness as a smaller scale. When comparing the low-clay Upper Woodford to the more clay-rich Middle and Lower Woodford, fracture toughness shows an increase in magnitude, up to 57%. A

decreasing trend of Woodford fracture toughness with clay packing density is observed (Figure 4.23), suggesting that the amount of non-clay minerals, here treated as inclusions, can contribute to an increment in fracture toughness in the lithofacies tested for the Upper Woodford. Furthermore, for such lithofacies (light gray laminated shale and calcareous laminated shale) the inclusion particles are mainly silt size (Figures 4.1 – 4.2). This suggests that an increase in energy might be required when the fracture propagates thorough such particles, overall increasing the fracture toughness. For calcareous laminated shale the presence of calcite in the siliceous laminations can also contribute to the overall increase in fracture toughness.

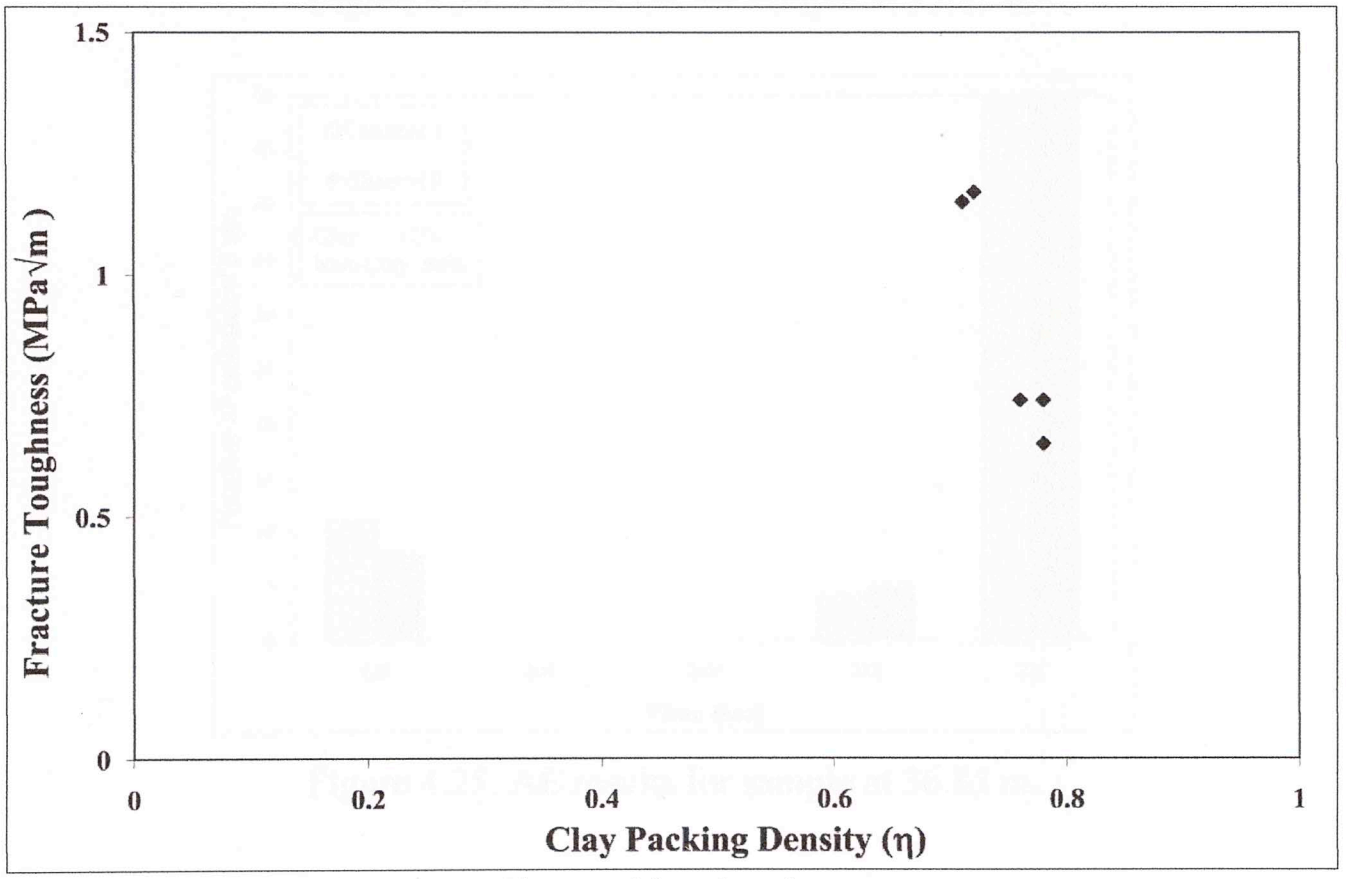

Figure 4.23. Fracture toughness vs. Clay packing density.

Lastly, the acoustic emissions (AE) recorded during CNSCB tests are shown in histograms in Figures 4.24 – 4.28. The moment of the uncontrollable fracture growth is indicated by the maximum number of emissions per unit of time in all diagrams. The light gray laminated shale (at 33.81 m) shows some early emissions only recorded

for one of the two acoustic crystals mounted on the sample surface. These emissions were possibly due to external noises.

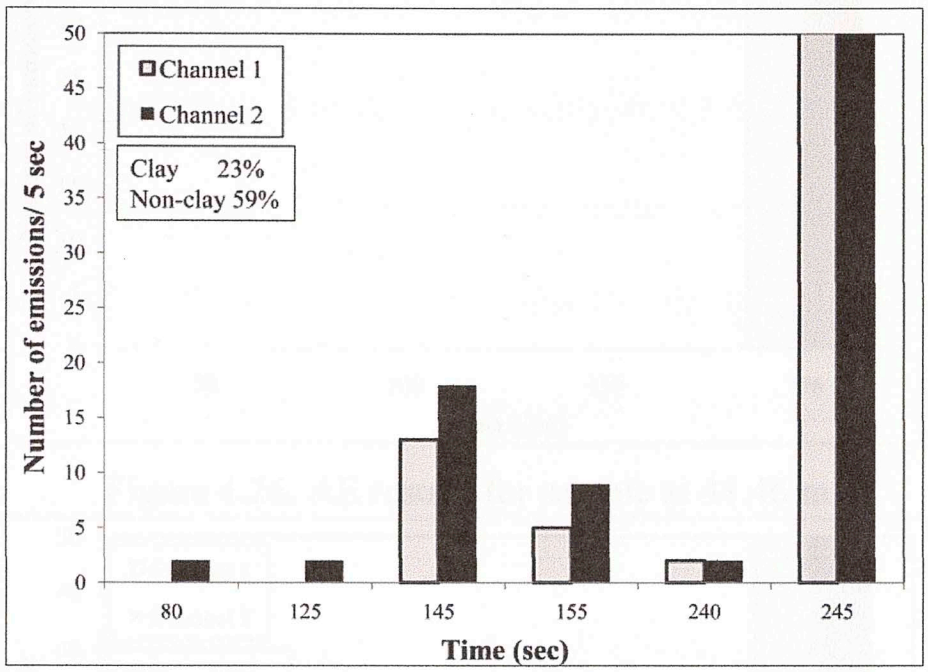

Figure 4.24. AE results for sample at 33.81 m

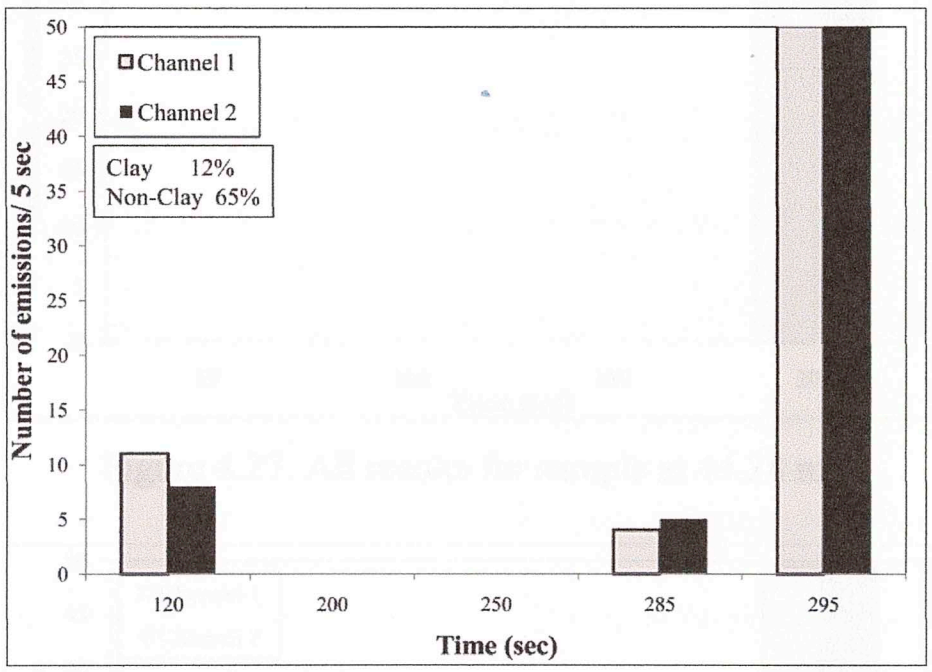

Figure 4.25. AE results for sample at 36.85 m.

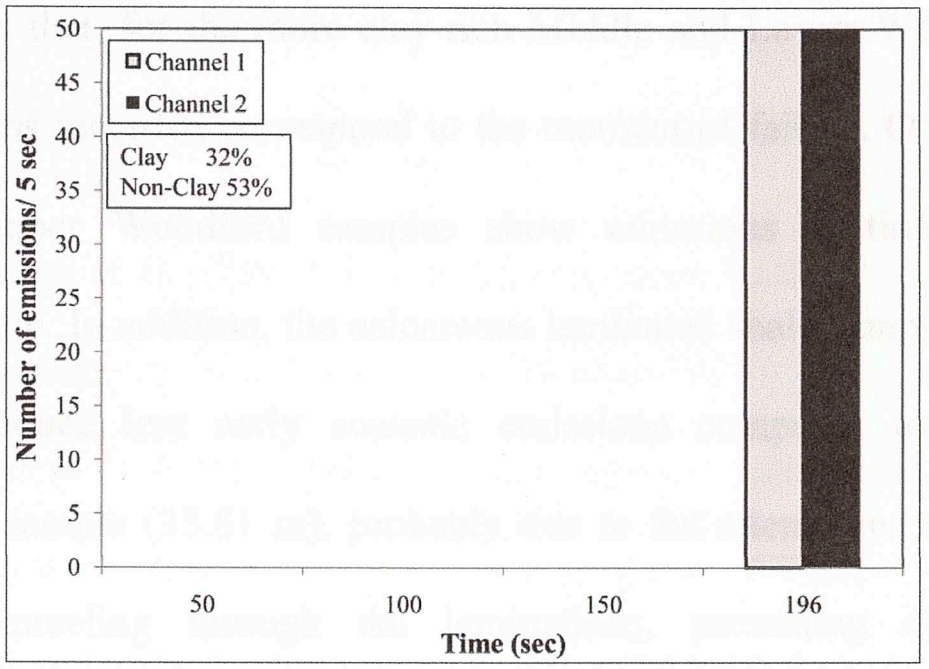

Figure 4.26. AE results for sample at 41.46 m

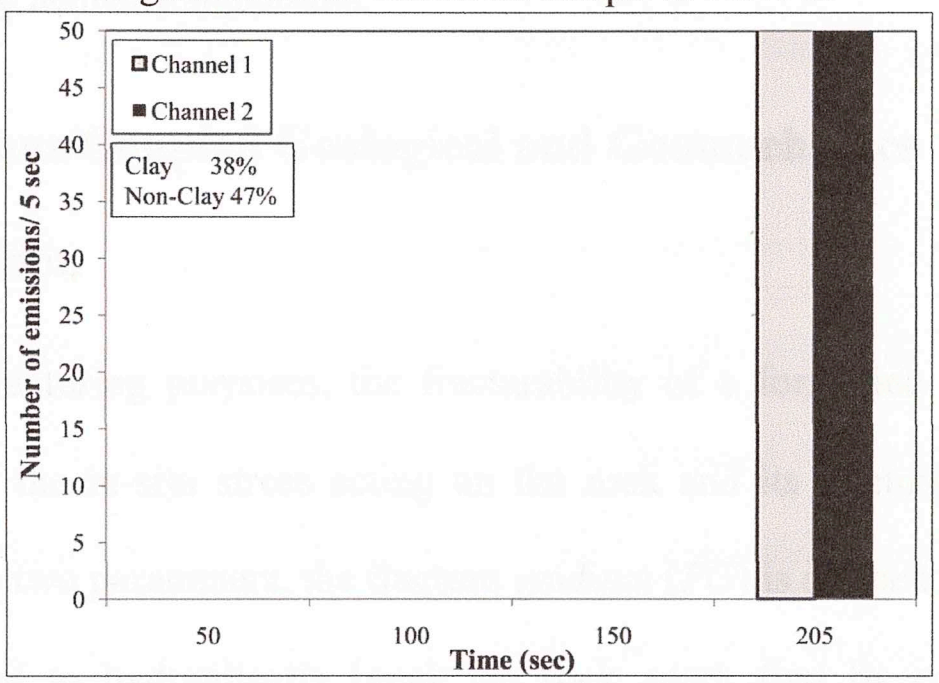

Figure 4.27. AE results for sample at 44.28 m.

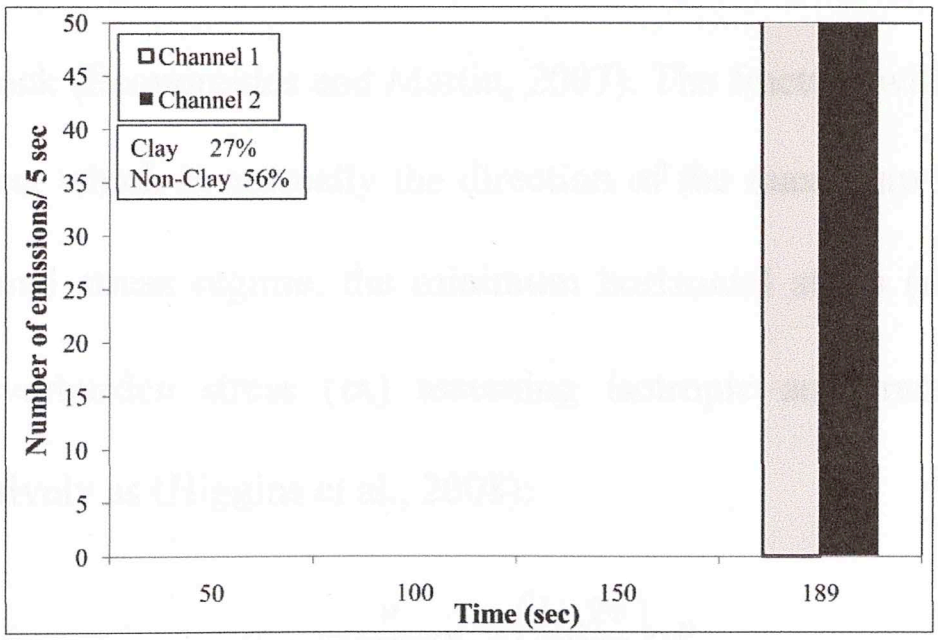

Figure 4.28. AE results for sample at 50.59 m.

The results show that, for the more clay-rich Middle and Lower Woodford samples, the only emissions recorded correspond to the moment of failure. On the other hand, the low-clay Upper Woodford samples show emissions at times prior to the catastrophic failure. In addition, the calcareous laminated shale sample (36.85 m) was observed to produce less early acoustic emissions compared to the light gray laminated shale sample (33.81 m), probably due to the attenuation of the generated elastic waves traveling through the laminations, presenting different mineral compositions and acoustic signatures.

4.4 Applications/Coupled Geological and Geomechanics Characterization

For hydraulic fracturing purposes, the fracturability of a formation is known to be dependent upon the in-situ stress acting on the rock and its fracture properties. By combining these two parameters, the fracture gradient (FG) is defined as the minimum pressure required to hydraulically break the rock apart, first by counteracting the horizontal stress acting on the formation, and then overcoming the inherent tensile strength of the rock (Economides and Martin, 2007). The fracture will follow the path of least resistance, which is normally the direction of the maximum horizontal stress (σ_H). For a normal stress regime, the minimum horizontal stress (σ_h) is defined in terms of the overburden stress (σ_v) assuming isotropic and transverse isotropic materials respectively as (Higgins et al., 2008):

$$\sigma_{\min} = \frac{\nu}{1-\nu}\sigma_V + \left(\frac{1-2\nu}{1-\nu}\right)\alpha P \tag{4.1}$$

$$\sigma_{\min} = \frac{E_1}{E_3}\frac{\nu_3}{1-\nu_1}(\sigma_V - \alpha_3 P) + \alpha_1 P \tag{4.2}$$

According to Waters et al., (2009): In the Arkoma basin for the Atoka, Coal, Hughes and Pittsburg counties, the Woodford ranges between 1830 – 2350 m (6000 -7700 ft) deep and 46 – 55 m (160-180 ft) thick. Assuming an overburden gradient of 0.023 MPa/m (1 psi/ft) and a normal pore pressure gradient of 0.01MPa/m (0.43 psi/ft) (Fjaer, 1992), the minimun horizontal stress was calculated for a simulated depth of 1830 m (6000 ft). Figure 4.29 shows the calculated σ_h, the fracture gradient (FG) and the previously defined couplets at the parasequence scale.

The results show that by recognizing the transverse isotropic nature of the Woodford, a better characterization of the horizontal stress (σ_h) can be achieved. Stress contrast is one of the main parameters analyzed for height confinement of the hydraulic fracture during stimulation (Economides and Martin, 2007). Therefore, a better definition of such contrasts is a valuable tool for the selection of the interval for stimulation designs.

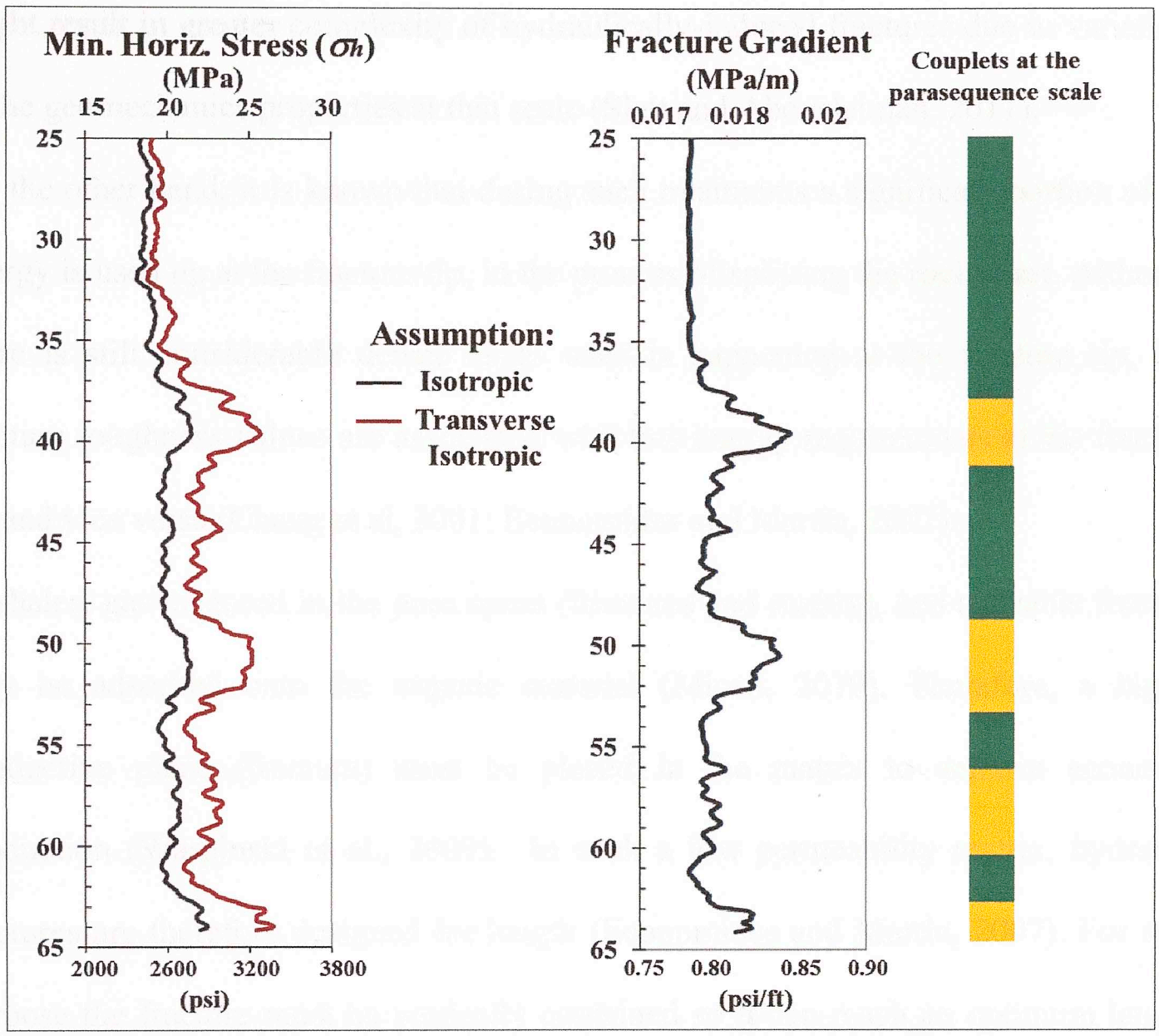

Figure 4.29. Min horizontal stress calculated using both, isotropic and anisotropic models. Fracture gradient and defined brittle/ductile couplets at the parasequence scale.

Figure 4.29 shows the correlation between the couplets at the parasequence scale and the fracture gradient. In terms of hydraulic fracturing, the couplets can be characterized as brittle and ductile, the first being the easiest to hydraulically fracture (low fracture gradient). These couplets can be resolved and mapped at a more regional scale (Slatt et al., 2008; Slatt and Abousleiman, 2011), providing a tool for horizontal wellbore placement, similar correlation of geomechanics and sequence stratigraphy has been recently investigated for the Woodford in the Permian basin by Harris et al. (2011). However, stratigraphic variability at a finer scale (lithofacies)

might result in greater complexity of hydraulically-induced fractures due to variations in the geomechanics properties at that scale (Slatt and Abousleiman, 2011).

On the other hand, it is known that during such treatments a significant portion of the energy is used up at the fracture tip, in the process of splitting the rock apart. Although there is still considerable debate as to what is happening at the fracture tip, low fracture toughness values are associated with low energy requirements at the fracture tip and vice versa (Chang et al, 2001; Economides and Martin, 2007).

In shales, gas is stored in the pore space (fractures and matrix), and a sizable fraction may be adsorbed onto the organic material (Miceli, 2010). Therefore, a highly conductive plane (fracture) must be placed in the matrix to achieve economic production (Warpinski et al., 2009). In such a low permeability matrix, hydraulic fractures are therefore designed for length (Economides and Martin, 2007). For such purpose the fracture must be vertically contained so it can reach an optimum length. Both contrasts in fracture gradient and fracture toughness can provide such height containment (Thiercelin et al., 1989; Economides and Martin, 2007). Despite the limited amount of tests, there appears to be a reduction in fracture toughness for the Middle/Lower Woodford (up to 57%), suggesting a fracture would be contained if performed in the Middle Woodford based on a difference in fracture toughness.

As previously mentioned, the Middle Woodford presents the highest organic richness, and therefore a brittle couple in the Middle Woodford might be an optimal target for well placement and completion (Figure 4.29).

All the previously mentioned laboratory analyses were performed on un-fractured samples. The presence of fractures has been proven to increase the effectiveness of

hydraulic fracturing treatments in shales (Gale et al., 2007; Economides and Martin, 2007; Warpsinsky, et al., 2009). In the area of study, two sets of fractures were identified. The fractures are confined mainly to the Upper Woodford (Slatt et al., 2010), suggesting that such member might be a tentative zone for hydraulic fracturing if fractures can be recognized and mapped. Under such conditions, the orientation and spacing of the fractures would determine the optimal well orientation in order to improve the treatment efficiency.

For the Middle Woodford the optimal well orientation might be aligned with σ_h, hence allowing a set of treatment stages with fractures perpendicular to the well axis. If similar fractures sets as the ones mentioned are present and can be mapped in the Upper Woodford, a horizontal well can be drilled crossing the fractures, hence allowing interconnection during treatment.

Multilateral wells were proposed for Woodford completion designs for the Arkoma basin by Newfield Exploration Co. In fact, in 2008 more than half of their wells were proposed to be drilled from multilateral pads (Dittrick, 2008). A multilateral well would allow to take advantage of both cases mentioned, having at least two laterals with different orientations as mentioned (Figure 4.30).

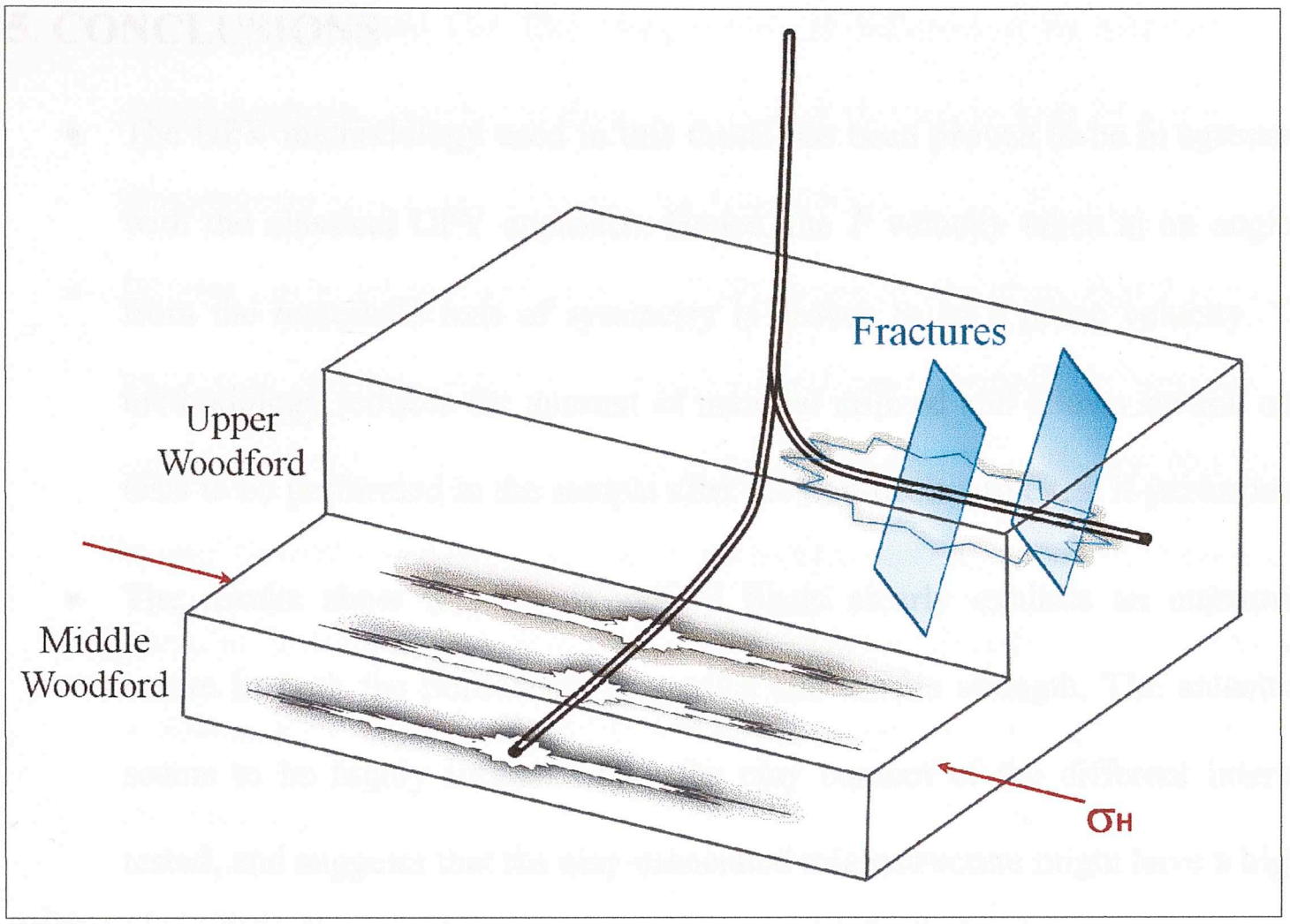

Figure 4.30. Schematic of a multilateral well drilled in the Woodford Shale.

5. CONCLUSIONS

- The UPV methodology used in this thesis has been proven to be in agreement with the classical UPV approach. Hence, the P velocity taken at an angle θ from the material's axis of symmetry is proven to be a phase velocity. This methodology reduces the amount of material utilized and allows several other tests to be performed in the sample after the non-destructive test is performed.

- The results show that the Woodford Shale clearly exhibits an anisotropic nature in both the poroelastic properties and tensile strength. The anisotropy seems to be highly influenced by the clay content of the different intervals tested, and suggests that the clay-associated microstructure might have a higher influence on anisotropy than possible laminations of different mineralogy at the mm scale. Further analyses reveal dependencies between the degrees of anisotropy with clay packing density. Despite the limited number of tests, an increasing trend of Woodford tensile strength with carbonate content can be observed, although such behavior seems to play a secondary role.

- The IDSTD^{TM} methodology presents good agreement with the classic unconfined compressive test methodology, affirming the IDSTD^{TM} as a powerful tool for the evaluation of shale formations, since difficulties in sample preparation for the classical methodologies are critical. An increase of the elastic stiffness coefficients during confinement was observed, which may be due to the closing of pre-existing cracks. A decrease of Thomsen's coefficients was observed during application of axial load, which is associated with a slight increase or even relative decrease of C_{11} and C_{66}, compared to the

increase of C_{33} and C_{44}. The phenomenon is believed to be associated with micro fractures forming in direction parallel to sample axis of symmetry, a phenomenon previously described by Tran (2009).

- Despite the small number of tests, CNSCB test results show that the fracture toughness of the low-clay, quartz-rich Upper Woodford samples are significantly higher (up to 50%) than those of the more clay-rich Middle and Lower Woodford samples, possibly due to the increase in size of the non-clay particles present in the lithofacies of the Upper Woodford. Also, acoustic emission prior to the uncontrollable fracture growth could only be recorded for the low-clay Upper Woodford.

- The GGSCS modeled anisotropic poroelastic moduli show good agreement with the measured values in the laboratory. Proposed correlations based on sonic log measurements were modified for unconfined compressive strength (UCS), and anisotropic tensile strength (σ_t) based on anisotropic Young's Modulus (E_1,E_3). E_1 is not available from standard well logs; the GGSCS results then provide a powerful tool for characterization of anisotropic properties of the Woodford Shale, showing good agreement between the measured values in the laboratory and the correlations proposed. Furthermore, by recognizing the transverse isotropic nature of shales, an improvement in their characterization and completion methodologies can be achieved.

- The interpreted parasequences in the sequence stratigraphy framework can be defined as brittle/ductile couplets, defining a brittle rock as one that is easily hydraulically fractured and vice versa for a ductile rock. Therefore, these

couplets define the tentative intervals for well placement and completion. Coupling these results with previous work in the same area, an optimal interval for completion was defined as a brittle/ductile couplet in the most organic-rich Middle Woodford. However, if fractures are present and can be mapped, the Upper Woodford presents an interesting target for completion. A multilateral well can take advantage of both intervals, drilling different trajectories in each member.

BIBLIOGRAPHY

Abousleiman, Y. N., Hoang, S. K., and Tran, M. H. (2010). Mechanical Characterization of Small Shale Samples Subjected to Fluid Exposure Using the Inclined Direct Shear Testing Device. *Int. Journ. of Rock Mechanics and Mining Sciences*, 47, 355-367.

Abousleiman, Y. N., Tran, M. H., and Hoang, S. K. (2008). Laboratory Characterization of Anisotropy and Fluid Effects on Shale Mechanical Properties Using Direct Shear Testing Device IDSTD. *42nd Rock Mechancis Symposium.* ARMA 08-256. San Francisco, CA: American Rock Mechanics Association.

Abousleiman, Y. N., Tran, M. H., Hoang, S. K., Christopher, B., Ortega, A., and Ulm, J. F. (2007). Geomechanics Field and Laboratory Characterization of Woodford Shale: the Next Gas Pay. *SPE Annual Technical Conference*. SPE 11120. Anaheim, CA: Society of Petroleum Engineers.

Abousleiman, Y. N., Tran, M. H., Hoang, S., Alberto, J., and Ulm, F. J. (2009). Geomechanics Field Characterization of the Two Profilic U.S Mid-West Gas Plays With Advanced Wire-Line Looging Tools . *SPE Annual Technical Conference*. SPE 124428. New Orleans, LA: Society of Petroleum Engineers.

Abousleiman, Y. N., Tran, M., Hoang, S., Ortega, A., and Ulm, F. (2010). Geomechnaics Field Characterization of Woodford Shale and Barnett Shalewith Advanced Looging Tools and Nano-indentation on Drilling Cuttings. *The Leading Edge*, 29, 730-736.

Abousleiman, Y., and Cui, L. (1998). Poroelastic soltions in transversely isotropic media for wellbore and cillinder. *Int. J. Solid Structures*, 35, 4905-4929.

Al-Tahini, A., and Abousleiman, Y. N. (2008). Acoustic Measurement and Calibration of In-situ Stresses Around a Wellbore. *SPE Annual Technical Conferece.* SPE 116132. Denver, Colorado: Society of Petroleum Enginners.

Amadei, B., Rogers, J. D., and Goodman, R. E. (1983). Elastic Constants ans Tensile Strength of the Anisotropic Rocks. *5th Congress Int. Society of Rock Mech.* Balkema, Roterdam: Int. society of Rock Mech. 189-196.

Arbenz, K. J. (2008). Structural Framework of the Ouachita Mountains. *Oklahoma Geological Survey*, circular 112A.

Aydin, A., and Basu, A. (2006). The Use of Brazilian Test as a Quantitative Measure of Rock Weathering. *Rock Mech. and Rock Eng.*, 39, 77-85.

Backer, T., Stanchits, S., and Dresen, G. (2005). Tensile Fracture Propagation and Acustic Emission Activity in Sandstone: The Effect of Loading Rate. *Int. Journ. Rock Mech. Min. Sci*, 42, 1094-1101.

Baihly, J. D., Malpani, R., Edwards, C., Han, S. Y., and Kok, J. C. (2010). Unlocking the Shale Mystery: How Lateral Measurements and Well Placement Impact Completion and Resultant Production. *SPE Tight Gas Completions Conference.* SPE 138427. San Antonio, TX: Society of Petroleum Engineers.

Banik, N. C. (1984). Velocity Anisotropy of Shales and Depth Convertion. *53rd International SEG Meeting.* Las Vegas, NV: Society of exploration Geophysicists.

Behera, L., and Tsvankin, I. (2009). Migration Velocity Analysis for Tilted Transversely Isotropic Media. *Geophysical Prospecting*, 57,13-26.

Behura, J., and Tsvankin, I. (2009). Reflection Coefficients in Attenuative Anisotropic Media. *Geophysics*, 74, WB193 - WB202.

Blakey, R. (2011). *Paleogeography and Geologic Evolution of North America.* http://jan.ucc.nau.edu. Accesed November 2010.

Britt, L. K., and Schoeffler, J. (2009). The Geomechanics of a Shlae Play: What Makes a Shale Prospective! *2009 SPE Eastern Regional Meeting.* SPE 125525. Charleston, WV: Society of Petroleum Engineers.

Buckner, T. N. (2011). *High Resolution Facies Changes, Lateral Continuity and Fracuring of the Woodford Whale from Behind Outcrop Drilling, Logging, and coring.* Master Thesis. Norman, OK: University of Oklahoma, In Progress.

Carriot, P., Costa, J., and Pinheiro, J. E. (1992). Cross-borehole Tomography in Anisotropic Media. *Geophysics*, 57, 1194-1198.

Chang, S., Lee, C., and Jeon, S. (2001). Measurement of Rock Fracture Toughness Under Modes I and II and Mixed Mode Condition by Using Disc Type Specimens. *Eng. Geology*, 66, 79-97.

Chong, K. P., and Smith, J. W. (1984). *Mechanics of Oil Shales.* Elsevier. New York, NY.

Chong, K. P., Kuruppu, M. D., Mahinda, D., and Kuszmaul, J. S. (1987). Fracture toughness Determination of Layered Materials. *Eng. Frac. Mech.*, 28, 43-54.

Claesson, J., and Bohloli, B. (2002). Brazilian Test: Stress field and Tensile Strength of Anisotroic Rocks Using an Analytical Solution. *Int. Journ. Rock Mech. Min Sci.*, 39, 991-1004.

Comer, J. B. (1991). Stratigraphic Analysis of the Upper Woodfor Formation, Permian Basin, West Texas and Southeastern New Mexico. *Bureau of Economic Geology, Report of Investigation 201.* Albuquerque, NM.

Comer, J. B. (2005). Facies Distribution and Hydrocarbon Production Potential of Woodford Shale in the Southern Midcontinent.*Oklahoma Geological Survey. Circular 110.* 229, 8.

Dai, S. T., and Labuz, J. F. (1997). Damage and Failure Analysis of Brittle Materials by Acoustic Emission. *Journ. Materialls in Civ. Eng.*, 200-205.

Dittrick, P. (2008). Longer Legs, Multilaterals Under Study in the Arkoma Woodford Shale Gas Pay. *Oil and Gas Journ.* 106, 13, 40-44.

Economides, M. J., and Martin, T. (2007). *Modern Fracturing, Enhancing Natural Gas Production.* Energy Tribune Publishing Inc. Houston, TX.

Ekbote, S., and Abousleiman, Y. N. (2006). Poroelastic solution for an Inclined Borehole Transverse Isotropic Formation. *Journ. of Eng. Mechanics*, 7, 754-763.

Fairhust, C. (1964). On the Validity of the Brazilian Test for Brittle Materials. *Int. Journ. Rock Mech and Mining Sci*, 1, 535-546.

Fjaer, R., Holt, R. M., Horsrud, P., Raaen, A. M., and Risnes, R. (1992). *Petroleum Related Rock Mchanicss.* Elsevier. New York, NY.

Gale, J. W., Reed, R. M., and Holder, J. (2007). Natural Fractures in the Barnett Shale and Their Importance for Hydraulic Fracture Treatments. *AAPG Bulletin*. 91,4, 603-622.

Gallant, C., Zhang, J., Wolfe, C. A., and Freeman, J. (2007) Wellbore Stability Considerations for Drilling Wells Through Finely Laminated Shale: A Case Study from Terra Nova. *SPE Annual Technical conference*. SPE 110742. Anaheim, CA. Society of Petroleum Engineers.

Harris, N. B., Miskimins, J. L., Minch, C. A. (2011). Mechanical Anisotropy in the Woodford Shale, Permian Basin: Origin, Magnitude, and Scale. *The Leading Edge,* 30 , 3, 284 - 291.

Higgins, S., Qestar, S. G., Donald, A., Bratton, T., and Tracy, G. (2008). Anisotropic Stress Models Improve completion Design in the Baxter Shale. *2008 Annual Technical Conference*. SPE 115736. Denver, CO. Society of Petroleum Engineers.

Hornby, B. E. (1994). *The Elastic Properties of Shale.* Cambridge, U.K: University of Cambrigde, PhD thesis.

Hornby, B. E. (1998). Experimental Laboratory Determination of the Dynamic Elastic properties of Wet, Drained Shlaes. *J. of Geophysical Research*, B12, 29945-29964.

Horsrud, P. (2001). Estimating Mechanical Properties of Shale from Empirical Correlations. *SPE Drilling and Completions*, SPE 50017, 68-73.

Johnston, J. E., and Christensen, N. I. (1994). Elastic Constants and Velocity Surfaces of Indurated Anisotropic Shlaes. *Survey in Geophysics*, 15, 481-494.

Johnston, J. E., and Christensen, N. I. (1995). Seismic anisotripy of Shale. *Journal of Geophysical Research*, 100, 4991-6003.

Kim, K. Y., Wrolstad, K. H., and Aminzadeh, F. (1993). Effect of Transverse Isotropy on P-Wave AVO for Gas Sands. *Geophysics*, 58, 883-888.

Kuruppu, M. D. (1997). Fracture Toughness Measurement Using Chevron Notched Semi-circular Specimen. *Int. Journ. Frac*, 86, L33-L38.

Lim, I. L., Johnston, I. W., Choi, S. K., and Boland, J. N. (1994). Fracture Testing of a Soft Rock with semicircular Specimen Under Three-point Bending. Part 1- Mode 1. *Int. Rock Mech. Min. Sci*, 3, 185-197.

Lim, I. L., Johnston, W. I., and Choi, S. K. (1993). Stress Intensity Factors for semicircular Specimen Under Three Point Bending. *Eng. Fracture Mech.*, 3, 363-382.

Lysak, M. V. (1996). Development of the Theory of Acoustic Emission by Propagating Cracks in Terms of Fraacture Mechancis. *Eng. Fract. Mech*, 3, 443-452.

Mansour, V. A. (1994). Acoustic Emission From Failing Rock Behavior. *Rock Mech. Rock Eng,*, 27, 173-182.

Mattews, L. H., Schein, G., and Malone, M. (2007). Stimulation of Gas Shale: They are the Same- Right? *2007 SPE Hydraulic Fracturing Technology Conference. SPE 106070.* Collegue Station, TX. Society of Petroleum Engineers.

Mavko, G., Mukerji, T., and Dvorkin, J. (2010). *The Rock Physics Handbook* . 2 Cambridge University Press. Cambridge, UK.

Miceli, A. A. (2010). *Geochemical Characterizartion of the Woodford Shale in Central and Southeastern Oklahoma.* Master Thesis. Norman, OK. University of Oklahoma.

Mitra, A., Warrington, D., and Sommer, A. (2010). Application of Lithofacies Models to Characterize Unconventional Shale Gas Reservoirs and Identify Optimal Completion Intervals. *SPE Western Regional Meeting.* Anaheim, CA: Society of Petroleum Engineers.

Newman, D. A., and Bennet, D. G. (1990). The Effect of Specimen Size and Stress Rate for the Brazilian Test- A Statistical Analysis. *Rock Mech. and Rock Eng.*, 23, 123-124.

Nguyen, V. X., Abousleiman, Y. N., and Hoang, S. K. (2008). Analyses of Wellbore Stability in Drilling Through Chemically Active Fractured Rock formations . *SPE Journal*. 2, 283-301. Richardson, TX: Society of Petroleum Engineers.

O'Brien, N. R., and Slatt, R. M. (1990). *Argillaceous Rock Atlas* . Springer-Verlag. New York, New York.

Ohnaka, M., and Kiyoo, M. (1982). Frecuency Characteristics of Acoustic Emission in Rocks Under Uniaxial Comresion and its Relation to the Fracturing Process to Failure. *Journ. Geophysics Res.*, 85, 3873-3884.

Okland, D., Hydro, N., and Cook, J. M. (1993). Bedding Related Borehole Inestability in High-Angle wells. *1993 SPE/ISRM Eurock*, Throndheim, Norway. SPE/ISRM 47285. Society of Petroleum Engineers.

Ortega, J. A., Ulm, F. J., and Abousleiman, Y. N. (2007). The Effect of the Nanogranular Nature on Shale on their Poroelastic Bahavior. *Acta Geotechnia*, 2, 155-182.

Pistre, V., Kinoshita, T., Endo, T., and Schilling, K. (2005). A Modular Sonic Tool for Measurements of 3D Formation Acoustic Properties. *SPWLA 46th Annual Logging Symposium.* New Orleans, LA. Society of Petrophysicist and Wellbore Anlasysts (SPWLA).

Portas, R. (2009). *Characterization and Origin of Fracture Patterns in the Woodford Shlae in Southeastern Oklahoma for Application to Exploration and development.* Master Thesis. Norman, OK: University of Oklahoma.

Rickman, R., Mullen, M., Petre, E., Grieser, B., and Kundert, D. (2008). A Practical Use of Shale Petrophysics for Stimulation Design Optimiztion: All Shale Plays Are Not Clones of the Barnett Shlae. *2008 SPE Annual Technical Conference and Exhibition.* SPE 115258. Denver, CO. Society of Petroleum Engineers.

Schoenberg, M., Muir, F., and Sayers, C. (1996). Introducing ANNIE a Simple Three Parameter Anisotropic Model for Shlaes. *Journ. of Seismic Exploration*, 5, 35-49.

Scott, E. T., and Abousleiman, Y. N. (2005). Acoustic Measurements of the Anisotropy of Dynamic Elastic and Poromechanis Moduli under Stress/Strain Pathways. *Journ. Eng. Mech.*, 131,937-946.

Sierra, R., Tran, M. H., Abousleiman, Y., and Slatt, R. M. (2010). Woodford Mechanical Properties and the Impact of Lithofacies. *44th US Rock Mechanics*

Symposium and 5th U.S.-Canada Rock Mechanics Symposium. ARMA 10-461. Salt Lake City, UT. American Rock Mechanics Association.

Slatt, R. M., and Abousleiman , Y. N. (2011). Merging Sequence Stratigraphy and Geomechanics for Unconventional Gas Shales. *The Leading Edge,* 30 , 3, 274 - 282.

Slatt, R. M., and Rodriguez, N. D. (2010). Comparative SequenceStratigraphy and Organic Geochemistry of Unconventional Gas Shlaes: Commonality or Coincidence? in Critical Assesment of Shale Resource Plays. *AAP/SEG/SPWLA Hedberg Conference*, Extended Abstracts.

Slatt, R. M., Prerna, S. R., Philp, P. R., Martfurt, K. J., and Abousleiman, Y. N. (2008). Workflow for Stratigraphic Characterization of Unconventional Gas Shale. *2008 SPE Shale-gas Production Conference*. SPE 119891. Forth Worth, TX. Society of Petroleum Engineers.

Slatt, R., Portas, Buckner, Abousleima, and O'Brien. (2010). Outcrop/behind Outcrop (Quarry) Multiscale Characterization of the Woodford Gas Shale, Oklahoma. In *AAPG Book on Unconventional Reservoirs.* American Associacion of Petroleum Geology.

Schlumberger/Services. (2011, February). (Schlumberger) Retrieved February 2011, from http://www.slb.com/services.aspx

Thiercelin, M., Jeffrey, R. G., and Naceur, K. B. (1989). Influence of Fracture Toughness on the Geometry of Hydraulic Fractures. *SPE Production Engineering, Nov*, 435-442.

Thomsen, L. (1986). Weak Elastic Anisotropy. *Geophysics*, 10, 1954-1966.

Tran, M. H. (2009). *Geomechanics Field and Laboratory Characterization of the Woodford Shale.* Master Thesis. Norman, OK. University of Oklahoma.

Tsvankin, I. (2005). *Seismic Signatures and Analysis of Reflection Data in Anisotropic Media.* Elsevier. New York, NY.

Tsvankin, I., Gaiser, J., and Grechka, V. (2009). Siesmic Anisotropy - Introduction. *Geophysics*, 5,WB1-WB2.

Ulm, F. J., and Abousleiman, Y. N. (2006). The Nanogranular Nature of Shale. *Acta Geotechnica*, 1, 77-88.

Vernik, l., and Nur, A. (1992). Ultrasoni Velocity and Anisotropy of Hydrocarbon Source Rocks. *Geophysics*, 57, 727-735.

Wang, Q. (1998). Stress intensity Factors of the ISRM Suggested CCNBD Specimen Used For Mode-1 Fracture Toughness. *Int. Journ. Rock Mech. Min Sci.*, 35, 997-982.

Warpsinsky, N. R., Magenhofer, M. C., Vincent, C. L., and Cipolla, C. L. (2009). Stimulated Unconventional Reservoirs: Maximizing Fracture Growth While Optimizing Fracture Conductivity. *Journal of Canadian PetroleumTechnology*, 48, 10, 39-51.

Waters, G., Dean, B., Downie, R., Kerrihard, K., Austbo, L., and McPherson, B. (2009). Simultaneous Hydraulic Fracturinf of Adjacent Horizontal Wells in the Woodford Shale. *2009 SPE Hydraulic Fracturing Technogy Conference*,SPE 119635. The Woodlands, TX. Socierty of Petroleum Engineers.

Wickstrom, C. W. (2008). Woodford Shale gas in Oklahoma. *AAPG Annual Convention and Exhibition.* San Antonio, TX. American Association of Petroleum Geologists ans Society for Sedimentary Geology.

Winterstein, D. F. (1986). Anisotropy Effect in P-wave and SH-wave stacking velocities contin information on Lithlogy. *Geophysics*, 3, 661-672.

Yuyama, S. (2005). Acoustic Emission for Fracture Studies Using Moment Tensor Analysis. *Journ. Strain Amalysis*, 40, 33-44.

Zoback, M. D. (2007). *Reservoir Geomechanics: Earth Stress and Rock Mechanics Applied to Exploration, Production and Wellbore Stability.* : Cambridge Press Cambridge, Massachussets.

APPENDIX A. Dynamic Measurements

Table A.1 – A.4 present the results for the sample at 33.81 m (Light gray laminated shale), from measured velocities to calculated poroelastic moduli.

Table A. 1. IDSTD measured velocities at different applied confining pressures and during axial loading for sample at 33.81 m.

IDSTD Velocities (m/sec)				
Confining Pressure				
Pressure (MPa)	*P*	*P45*	*angle*	*S*
3.45	2918	2913	21.2	1644
4.14	2918	2913	21.2	1647
5.52	2930	2924	21.3	1647
6.90	2942	2935	21.4	1651
10.34	2967	2946	21.4	1659
13.79	2979	2957	21.5	1674
Axial Loading				
Dev. Stress (MPa)	*P*	*P45*	*angle*	*S*
0.00	2979	2957	21.5	1674
11.17	3030	2957	21.5	1723
22.09	3043	2969	21.6	1744
33.00	3056	2981	21.7	1752
43.91	3069	2981	21.7	1765
54.83	3095	2992	21.8	1770
65.74	3082	2992	21.8	1770

Table A.2. IDSTD calculated dynamic stiffness coefficients at different applied confining pressures and during axial loading for sample at 33.81 m.

Dynamic Stiffness Coefficients (GPa)							**Thomsen's Coeff.**	
Confining Pressure								
Pressure (MPa)	*C11*	*C33*	*C44*	*C66*	*C12*	*C13*	ε	γ
3.45	24.99 ± 4.02	18.26	5.79	7.76 ± 1.80	9.47 ± 1.80	6.74 ± 1.01	0.18	0.17
4.14	24.99 ± 2.21	18.26	5.82	7.76 ± 0.99	9.47 ± 0.99	6.73 ± 0.99	0.18	0.17
5.52	24.97± 2.26	18.41	5.82	7.75 ± 1.01	9.47 ± 1.01	6.75 ± 1.01	0.18	0.17
6.90	24.96 ± 2.21	18.56	5.85	7.75 ± 0.99	9.46 ± 0.99	6.76 ± 0.99	0.17	0.16
10.34	24.98 ± 2.24	18.87	5.90	7.76 ± 1.00	9.46 ± 1.00	6.69 ± 1.00	0.16	0.16
13.79	25.01 ± 2.28	19.02	6.01	7.77 ± 1.02	9.47 ± 1.02	6.68 ± 1.02	0.16	0.15
Axial Loading								
Dev. Stress (MPa)	*C11*	*C33*	*C44*	*C66*	*C12*	*C13*	ε	γ
0.00	25.01 ± 2.26	19.02	6.01	7.77 ± 1.01	9.47 ± 1.01	6.68 ± 1.01	0.16	0.15
11.17	24.94 ± 2.19	19.67	6.36	7.74 ± 0.98	9.46 ± 0.98	6.16 ± 0.98	0.13	0.11
22.09	24.98 ± 2.24	19.84	6.52	7.78 ± 1.00	9.42 ± 1.01	6.16 ± 1.00	0.13	0.10
33.00	24.95 ± 2.30	20.02	6.58	7.76 ± 1.03	9.43 ± 1.03	6.16 ± 1.03	0.12	0.09
43.91	24.93 ± 2.30	20.19	6.68	7.77 ± 1.03	9.39 ± 1.01	6.09 ± 1.03	0.12	0.08
54.83	24.95 ± 2.26	20.54	6.72	7.77 ± 1.01	9.41 ± 1.01	5.96 ± 1.01	0.11	0.08
65.74	24.90 ± 2.26	20.36	6.72	7.76 ± 1.01	9.38 ± 1.02	5.84 ± 1.01	0.11	0.08

Table A.3. IDSTD calculated dynamic poroelastic moduli at different applied confining pressures and during axial loading for sample at 33.81 m.

IDSTD Elastic Moduli (GPa)						**Biot's Coeff.**	
Confining Pressure							
Pressure (MPa)	*E1*	*E3*	*G1*	*G3*	*v3*	*α1*	*α3*
3.45	20.34 ± 9.39	15.62	7.76 ± 0.99	5.79	0.20	0.62	0.71
4.14	20.34 ± 5.37	15.63	7.76 ± 1.01	5.82	0.20	0.62	0.71
5.52	20.32 ± 5.47	15.76	7.75 ± 0.99	5.82	0.20	0.62	0.70
6.90	20.32 ± 5.36	15.91	7.75 ± 1.00	5.85	0.20	0.62	0.70
10.34	20.39 ± 5.37	16.27	7.76 ± 1.02	5.90	0.19	0.62	0.70
13.79	20.43 ± 5.47	16.44	7.77 ± 1.01	6.01	0.19	0.62	0.70
Axial Loading							
Dev. Stress (MPa)	*E1*	*E3*	*G1*	*G3*	*v3*	*α1*	*α3*
0.00	20.43 ± 5.36	16.44	7.77 ± 1.01	6.01	0.19	0.62	0.70
11.17	20.55 ± 5.37	17.47	7.74 ± 0.98	6.36	0.18	0.62	0.70
22.09	20.62 ± 5.36	17.64	7.78 ± 1.01	6.52	0.18	0.62	0.70
33.00	20.59 ± 5.25	17.81	7.76 ± 1.03	6.58	0.18	0.62	0.70
43.91	20.62 ± 5.23	18.03	7.77 ± 1.01	6.68	0.18	0.63	0.70
54.83	20.68 ± 5.23	18.47	7.77 ± 1.01	6.72	0.17	0.63	0.70
65.74	20.67 ± 5.19	18.37	7.76 ± 1.02	6.72	0.17	0.63	0.70

Tables A.4 – A.6 present the results for the sample at 36.86 m (Calcareous laminated shale), from measured velocities to calculated poroelastic moduli.

Table A.4. IDSTD measured velocities at different applied confining pressures and during axial loading for sample at 36.86 m.

IDSTD Velocities (m/sec)				
Confining Pressure				
Pressure (MPa)	*P*	*P45*	*angle*	*S*
3.45	2900	2929	21.3	1628
4.14	2900	2929	21.3	1628
5.52	2924	2940	21.4	1635
6.90	2948	2940	21.4	1635
10.34	2972	2951	21.5	1647
13.79	2997	2962	21.6	1643
Axial Loading				
Dev. Stress (MPa)	*P*	*P45*	*angle*	*S*
0.00	2997	2962	21.6	1643
10.71	3035	3068	22.4	1677
21.59	3087	3093	22.6	1709
32.48	3128	3118	22.8	1714
43.37	3128	3130	22.9	1718
54.25	3142	3130	22.9	1722
65.14	3155	3143	23.0	1722
76.02	3155	3143	23.0	1726
86.91	3169	3143	23.0	1726

Table A.5. IDSTD calculated dynamic stiffness coefficients at different applied confining pressures and during axial loading for sample at 36.86 m.

Dynamic Stiffness Coefficients (GPa)							**Thomsen's Coeff.**	
Confining Pressure								
Pressure (MPa)	*C11*	*C33*	*C44*	*C66*	*C12*	*C13*	ε	γ
3.45	24.12 ± 2.26	17.95	5.66	7.45 ± 1.01	9.22 ± 1.01	7.84 ± 1.01	0.17	0.16
4.14	24.10 ± 2.26	17.95	5.66	7.45 ± 1.01	9.22 ± 1.01	7.78 ± 1.01	0.17	0.16
5.52	24.09 ± 2.26	18.25	5.71	7.44 ± 1.00	9.21 ± 1.01	7.71 ± 1.01	0.16	0.15
6.90	24.05 ± 2.26	18.55	5.71	7.43 ± 1.01	9.19 ± 1.01	7.55 ± 1.01	0.15	0.15
10.34	23.92 ± 2.28	18.86	5.79	7.39 ± 1.02	9.14 ± 1.02	7.42 ± 1.01	0.13	0.14
13.79	23.95 ± 2.24	19.17	5.76	7.39 ± 1.00	9.17 ± 1.00	7.37 ± 1.01	0.12	0.14
Axial Loading								
Dev. Stress (MPa)	*C11*	*C33*	*C44*	*C66*	*C12*	*C13*	ε	γ
0.00	23.95 ± 2.24	19.17	5.76	7.39 ± 1.00	9.17 ± 1.00	7.37 ± 1.00	0.12	0.14
10.71	24.08 ± 2.28	19.66	6.01	7.45 ± 1.02	9.18 ± 1.02	7.95 ± 1.02	0.11	0.12
21.59	24.14 ± 2.26	20.35	6.24	7.47 ± 1.01	9.20 ± 1.01	7.82 ± 1.01	0.09	0.10
32.48	24.14 ± 2.19	20.89	6.27	7.47 ± 0.98	9.20 ± 0.98	7.73 ± 0.98	0.08	0.10
43.37	24.14 ± 2.19	20.89	6.30	7.46 ± 0.98	9.18 ± 0.98	7.8 ± 0.98	0.08	0.09
54.25	24.05 ± 2.24	21.07	6.33	7.43 ± 1.00	9.19 ± 1.00	7.74 ± 1.00	0.07	0.09
65.14	24.08 ± 2.24	21.25	6.33	7.43 ± 1.00	9.22 ± 1.00	7.77 ± 1.00	0.07	0.09
76.02	24.07 ± 2.30	21.25	6.36	7.43 ± 1.03	9.21 ± 1.03	7.75 ± 1.03	0.07	0.08
86.91	24.03 ± 2.24	21.44	6.36	7.42 ± 1.00	9.19 ± 1.00	7.68 ± 1.00	0.06	0.08

Table A.6. IDSTD calculated dynamic poroelastic moduli at different applied confining pressures and during axial loading for sample at 36.86 m.

IDSTD Elastic Moduli (GPa)						**Biot's Coeff.**	
Confining Pressure							
Pressure (MPa)	*E1*	*E3*	*G1*	*G3*	*v3*	*α1*	*α3*
3.45	19.07 ± 4.72	14.26	7.45 ± 1.01	5.66	0.24	0.62	0.69
4.14	19.08 ± 4.72	14.32	7.45 ± 1.01	5.66	0.23	0.62	0.69
5.52	19.14 ± 4.72	14.69	7.44 ± 1.00	5.71	0.23	0.62	0.69
6.90	19.19 ± 4.72	15.12	7.43 ± 1.01	5.71	0.23	0.62	0.69
10.34	19.16 ± 4.72	15.53	7.39 ± 1.02	5.79	0.22	0.63	0.69
13.79	19.22 ± 4.72	15.89	7.39 ± 1.00	5.76	0.22	0.63	0.69
Axial Loading							
Dev. Stress (MPa)	*E1*	*E3*	*G1*	*G3*	*v3*	*α1*	*α3*
0.00	19.22 ± 4.72	15.89	7.39 ± 1.00	5.76	0.22	0.63	0.69
10.71	19.16 ± 4.72	15.86	7.45 ± 1.02	6.01	0.24	0.62	0.67
21.59	19.33 ± 4.72	16.70	7.47 ± 1.01	6.24	0.23	0.62	0.67
32.48	19.39 ± 4.72	17.30	7.47 ± 0.98	6.27	0.23	0.62	0.66
43.37	19.33 ± 4.72	17.23	7.46 ± 0.98	6.30	0.23	0.62	0.66
54.25	19.31 ± 4.72	17.46	7.43 ± 1.00	6.33	0.23	0.62	0.66
65.14	19.32 ± 4.72	17.63	7.43 ± 1.00	6.33	0.23	0.62	0.66
76.02	19.33 ± 4.72	17.65	7.43 ± 1.03	6.36	0.23	0.62	0.66
86.91	19.33 ± 4.72	17.89	7.42 ± 1.00	6.36	0.23	0.62	0.66

Table A.7- A.9 present the results for the sample at 50.27 m Gray/Black laminated shale), from measured velocities to calculated poroelastic moduli.

Table A.7. IDSTD measured velocities at different applied confining pressures and during axial loading for sample at 50.27 m.

Confining Pressure				
Pressure (MPa)	*P*	*P45*	*angle*	*S*
1.38	3028	3143	22.9	1733
2.76	3041	3194	23.3	1750
4.14	3068	3234	23.7	1767
5.52	3068	3261	23.9	1790
6.90	3095	3261	23.9	1812
8.27	3122	3275	24.0	1826
9.65	3122	3289	24.0	1836
11.03	3136	3289	24.0	1850
12.41	3150	3303	24.2	1850
13.79	3150	3316	24.3	1850
Axial Loading				
Dev. Stress (MPa)	*P*	*P45*	*angle*	*S*
12.27	3150	3316	24.3	1865
16.23	3150	3316	24.3	1870
20.19	3150	3316	24.3	1890
24.15	3164	3316	24.3	1900
28.11	3164	3316	24.3	1900
32.06	3164	3316	24.3	1900
36.02	3164	3331	24.4	1920
39.98	3164	3331	24.4	1920
43.94	3164	3331	24.4	1926
47.90	3164	3331	24.4	1926
51.86	3178	3331	24.4	1926
55.82	3178	3331	24.4	1926
59.77	3178	3345	24.5	1926
63.73	3178	3345	24.5	1926
67.69	3178	3359	24.6	1915
71.65	3178	3331	24.4	1900
75.61	3178	3331	24.4	1880
79.57	3136	3275	24.0	1831

Table A.8. IDSTD calculated dynamic stiffness coefficients at different applied confining pressures and during axial loading for sample at 50.27 m.

Dynamic Stiffness Coefficients (GPa)							**Thomsen's Coeff.**	
Confining Pressure								
Pressure (MPa)	*C11*	*C33*	*C44*	*C66*	*C12*	*C13*	ε	γ
2.76	27.13 ± 2.28	21.00	6.95	9.63 ± 0.98	7.87 ± 1.03	7.99 ± 1.03	0.15	0.19
4.14	27.27 ± 2.26	21.36	7.09	9.68 ± 0.98	7.91 ± 1.03	8.23 ± 1.03	0.14	0.18
5.52	27.29 ± 2.24	21.36	7.27	9.68 ± 1.02	7.93 ± 1.01	8.26 ± 1.02	0.14	0.17
6.90	27.29 ± 2.21	21.74	7.46	9.68 ± 1.00	7.93 ± 1.00	8.26 ± 1.00	0.13	0.15
9.65	27.39 ± 2.24	22.12	7.65	9.72 ± 0.99	7.95 ± 0.99	8.33 ± 0.99	0.12	0.14
11.03	27.43 ± 2.50	22.32	7.77	9.74 ± 1.00	7.95 ± 1.00	8.35 ± 1.00	0.11	0.13
13.79	27.44 ± 2.24	22.52	7.77	9.74 ± 1.12	7.96 ± 1.12	8.35 ± 1.12	0.11	0.13
Axial Loading								
Dev. Stress (MPa)	*C11*	*C33*	*C44*	*C66*	*C12*	*C13*	ε	γ
0.00	27.44 ± 2.24	22.52	7.81	9.74 ± 1.00	7.96 ± 1.00	8.35 ± 1.00	0.11	0.12
12.27	27.44 ± 2.21	22.52	7.89	9.74 ± 0.99	7.96 ± 0.99	8.39 ± 0.98	0.11	0.11
20.19	27.59 ± 2.24	22.52	8.11	9.81 ± 1.00	7.97 ± 1.00	8.70 ± 1.00	0.11	0.11
28.11	27.48 ± 2.19	22.72	8.19	9.77 ± 0.98	7.94 ± 0.98	8.49 ± 0.97	0.10	0.10
36.02	27.61 ± 2.21	22.72	8.37	9.82 ± 0.99	7.97 ± 0.99	8.60 ± 0.99	0.11	0.09
43.94	27.62 ± 2.24	22.72	8.42	9.83 ± 1.00	7.96 ± 1.00	8.60 ± 1.01	0.11	0.08
51.86	27.61 ± 2.26	22.92	8.42	9.83 ± 1.01	7.95 ± 1.01	8.56 ± 1.00	0.10	0.08
59.77	27.59 ± 2.48	22.92	8.42	9.81 ± 1.11	7.97 ± 1.11	8.60 ± 1.10	0.10	0.08
67.69	27.64 ± 2.21	22.92	8.46	9.83 ± 0.99	7.98 ± 0.99	8.64 ± 0.99	0.10	0.08
75.61	27.58 ± 2.26	22.92	8.37	9.80 ± 1.01	7.98 ± 1.01	8.64 ± 1.01	0.10	0.09
80.46	27.59 ± 2.19	22.52	8.19	9.77 ± 0.98	8.05 ± 1.01	8.15 ± 1.01	0.11	0.09

Table A.9. IDSTD calculated dynamic poroelastic moduli at different applied confining pressures and during axial loading for sample at 50.27 m.

IDSTD Elastic moduli (GPa)						**Biot's Coeff.**	
Confining Pressure							
Pressure (MPa)	*E1*	*E3*	*G1*	*G3*	*v3*	*α1*	*α3*
2.76	23.12 ± 4.01	17.35	9.63	6.95	0.23	0.60	0.66
4.14	23.17 ± 4.06	17.51	9.68	7.09	0.23	0.60	0.65
5.52	23.17 ± 4.02	17.49	9.68	7.27	0.23	0.60	0.65
6.90	23.2 ± 3.99	17.86	9.68	7.46	0.23	0.60	0.65
9.65	23.3 ± 4.00	18.20	9.72	7.65	0.24	0.60	0.64
11.03	23.35± 4.46	18.38	9.74	7.69	0.24	0.60	0.64
13.79	23.37 ± 3.99	18.58	9.74	7.81	0.24	0.59	0.64
Axial Loading							
Dev. Stress (MPa)	*E1*	*E3*	*G1*	*G3*	*v3*	*α1*	*α3*
0.00	23.37 ± 4.00	18.58	9.74 ± 1.00	7.81	0.24	0.59	0.64
12.27	23.35 ± 4.46	18.54	9.74 ± 0.99	7.89	0.24	0.59	0.64
20.19	23.35 ± 3.99	18.26	9.81 ± 1.00	8.11	0.24	0.59	0.63
28.11	23.37 ± 3.95	18.65	9.77 ± 0.98	8.19	0.24	0.59	0.63
36.02	23.44 ± 3.97	18.56	9.82 ± 0.99	8.37	0.24	0.59	0.63
43.94	23.46 ± 3.90	18.56	9.83 ± 1.00	8.42	0.24	0.59	0.63
51.86	23.49 ± 4.41	18.80	9.83 ± 1.01	8.42	0.24	0.59	0.63
59.77	23.44 ± 4.41	18.76	9.81 ± 1.11	8.42	0.24	0.59	0.63
67.69	23.47 ± 4.08	18.73	9.83 ± 0.99	8.46	0.24	0.59	0.63
75.61	23.41 ± 4.01	18.73	9.80 ± 1.01	8.37	0.24	0.59	0.63
80.46	23.58 ± 4.01	18.79	9.77 ± 0.98	8.19	0.23	0.59	0.64